

**CATALYSIS OF CARBON-CARBON COUPLING REACTIONS FOR THE
FORMATION OF LIQUID HYDROCARBON FUELS FROM BIOMASS
AND SHALE GAS RESOURCES**

by

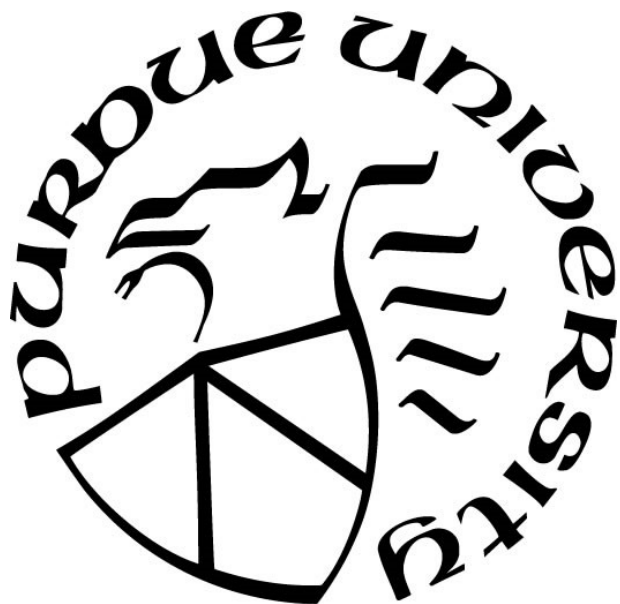
Richard Caulkins

A Dissertation

Submitted to the Faculty of Purdue University

In Partial Fulfillment of the Requirements for the degree of

Doctor of Philosophy



Davidson School of Chemical Engineering

West Lafayette, Indiana

December 2021

THE PURDUE UNIVERSITY GRADUATE SCHOOL
STATEMENT OF COMMITTEE APPROVAL

Dr. Fabio Ribeiro, Chair.

Davidson School of Chemical Engineering

Dr. Rajamani Gounder

Davidson School of Chemical Engineering

Dr. Jeffrey Miller

Davidson School of Chemical Engineering

Dr. Christina Li

Department of Chemistry

Approved by:

Dr. John A. Morgan

Soli Deo Gloria

ACKNOWLEDGMENTS

I am deeply grateful to many of the people who I have worked with since the start of my Ph.D., without whom none of the following work would have been possible. I have been fortunate to be a part of two incredible research centers at Purdue, with opportunities for extensive collaboration with experts in a wide variety of disciplines.

My first project as a graduate student dealt with upgrading biomass pyrolysis vapors, and I was lucky to have a group of senior students in the project as mentors during my first year in Prof. Ribeiro's research group. Drs. Harshavardhan Choudhari, John Degenstein, and Emre Gencer provided much of the initial direction on these projects, and they were instrumental in guiding my initial research and development as a graduate student. Ian Smith was a close collaborator following their departure. I would like to specially acknowledge Drs. Abhijit Talpade and Taufik Ridha. Frequent technical discussions on catalytic upgrading, fast pyrolysis mechanisms, and systems-level upgrading allowed for a much more complete picture of the H2Bioil process than would have been possible working individually. All of the work presented here concerning biomass pyrolysis is best understood as a collaborative effort between the three of us. I would also like to thank the professors who advised this project, Profs. Fabio Ribeiro, Rakesh Agrawal, and Nicholas Delgass. I would like to specially acknowledge Prof. Delgass, who as an emeritus professor was extremely generous with his time in advising on the biomass project. His technical insights were critical to its progression, and he is greatly missed. I would finally like to acknowledge our close collaboration with Prof. Hilkka Kenttamaa's research group, particularly with her students Drs. Priya Murria, Lan Xu, and McKay Easton. Their fundamental insights into the mechanisms of fast pyrolysis were critical to advancing our understanding of the phenomena we observed in our labs.

Following my work on the biomass project, I was put on a new project concerning Ni-catalyzed oligomerization of ethene derived from shale gas resources. I had the pleasure of working with an entirely new group of collaborators on this project, and I would like to thank Arunima Saxena, Dr. Ravi Joshi, Ranga Rohit Seemakurthi, and Elizabeth Bickel for their help in starting the new project and their continued support in technical discussions as the project

progressed. I would like to specially thank Prof. Rajamani Gounder for advising on the technical portions of this project; without his input, this work would not have been possible.

I would like to thank Yury Zvinevich, whose technical expertise is critical in constructing and maintaining the laboratory equipment used in catalysis research at Purdue.

Finally, I would like to thank my advisor, Prof. Fabio Ribeiro, who has demonstrated tremendous patience with me during my Ph.D.. His commitment to rigorous research in the field of catalysis is an example to all of the students in the Purdue Catalysis Center.

I would also like to acknowledge the sources of funding for my projects. The work presented here on biomass was supported by the Center for Direct Catalytic Conversion of Biomass to Biofuels (C3Bio), an Energy Frontier Research Center funded by the U.S. Department of Energy (DOE), Office of Science, Basic Energy Sciences (BES), under Award #DE-SC0000997. The work on ethene oligomerization was supported by the National Science Foundation under Cooperative Agreement No. EEC-1647722, an Engineering Research Center for the Innovative and Strategic Transformation of Alkane Resources. We also acknowledge the financial support from the donors of the American Chemical Society Petroleum Research Fund under Grant No. 54216-DNI5 for the synthesis and characterization of the Ni-zeolite samples used in this study. We acknowledge the helpful technical discussions with Prof. Enrique Iglesia (University of California-Berkeley) and financial support from the Neil Armstrong Distinguished Visiting Fellowship (Purdue University). We also acknowledge the helpful discussions with Dr. Ted Calverley (Purdue University)

TABLE OF CONTENTS

LIST OF TABLES	8
LIST OF FIGURES	9
ABSTRACT	12
1. ALDOL CONDENSATION OF BIOMASS FAST PYROLYSIS PRODUCTS	13
1.1 Introduction	13
1.1.1 Production of Liquid Fuels from Biomass via the H2Bioil Process.....	13
1.1.2 Fast Pyrolysis of Lignocellulosic Biomass.....	14
1.1.3 Hydrodeoxygenation.....	15
1.1.4 Aldol Condensation	15
1.2 Methods and Materials.....	20
1.2.1 Catalyst Preparation.....	20
1.2.2 Reactors	21
1.3 Results and Discussion	24
1.3.1 Aldol condensation of butanal	24
1.3.2 Sequential Aldol Condensation and Hydrodeoxygenation of Butanal	26
1.3.3 Sequential Aldol Condensation and Hydrodeoxygenation of Glycolaldehyde	28
1.3.4 Sequential Aldol Condensation and Hydrodeoxygenation HDO of Cellulose Pyrolysis Vapors	30
1.3.5 Sequential Aldol Condensation and Hydrodeoxygenation of Levoglucosenone and 5- HMF	32
1.3.6 Dehydration of Levoglucosan.....	39
1.4 Conclusions.....	44
2. ORIGINS OF CHAR FORMATION	46
2.1 Introduction.....	46
2.1.1 Effect of inorganic impurities.....	46
2.1.2 Influence of biomass components on char formation.....	46
2.2 Materials and Methods.....	47
2.2.1 Preparation of Inorganic-Doped Cellobiose	47
2.2.2 Preparation of Hemicellulose-free and Lignin-free Samples	47

2.2.3 Py-GC/MS Reactor	48
2.3 Results and Discussion	49
2.3.1 Effects of Inorganic Dopants on Cellobiose Pyrolysis	49
2.3.2 Contribution of Hemicellulose to Char Formation	53
2.4 Conclusions	54
3. EFFECTS OF ETHENE PRESSURE ON THE DEACTIVATION OF NI-ZEOLITES DURING ETHENE OLIGOMERIZATION AT SUB-AMBIENT TEMPERATURES	56
3.1 Introduction	56
3.2 Materials and Methods	57
3.3 Results and Discussion	59
3.4 Conclusions	66
APPENDIX A. QUANTIFICATION OF PYROLYSIS PRODUCTS USING FID AND EFFECTIVE CARBON NUMBER ESTIMATES	68
APPENDIX B. NREL LAP PROCEDURE	70
APPENDIX C. DETAILED PRODUCT DISTRIBUTION OF PYROLYSIS OF NA-DOPED CELLOBIOSE	71
APPENDIX D. N ₂ ADSORPTION ISOTHERMS FOR NI-MCM-41, NI-BETA, NI-FAU-6, AND NI-FAU-40	76
APPENDIX E. PORE SIZE DISTRIBUTIONS FOR NI-MCM-41, NI-BETA, NI-FAU-6, AND NI-FAU-40	80
APPENDIX F. EFFECTS OF BRØNSTED ACID SITES ON DEACTIVATION	84
APPENDIX G. STATISTICAL GOODNESS-OF-FIT ANALYSIS OF DEACTIVATION PARAMETER FITTING	87
APPENDIX H. MODELING OF DEACTIVATION TRANSIENTS IN DATA FROM AGIRREZABAL-TELLERIA AND IGLESIA	92
REFERENCES	94
PUBLICATIONS	103

LIST OF TABLES

Table 1. Carbon contents (% by weight) of unpyrolyzed cellulose and poplar samples and of char residue following pyrolysis of these samples.	23
Table 2: Carbon balances for aldol condensation over 2% Cu/TiO ₂ plus HDO over PtMo/MWCNTs of HMF and GA+HMF dissolved in methanol	38
Table 4. NREL LAP Analysis of Poplar and Maleic Acid Pretreated Poplar	48
Table 5. Carbon selectivity to char for cellobiose doped with 1% or 10% of various inorganic salts	53
Table 6. Char yields and carbon balances following fast pyrolysis and hydrodeoxygenation of poplar, cellulose, delignified poplar, and maleic acid pretreated poplar.	54
Table 7. Deactivation constants (k_d) and orders (n), and initial ethene dimerization rates (r_0) for Ni-MCM-41, Ni-Beta, Ni-FAU-6, and Ni-FAU-40 measured at different ethene reduced pressures (P/P_0). Statistical estimates of goodness-of-fit and uncertainties are reported in Table 12 (SI)... ..	63
Table 8. Deactivation constants (k_d) and orders (n), and initial ethene dimerization rates (r_0) for Ni-FAU-40 at different ethene reduced pressures (P/P_0) with and without H ₂ co-feed and pretreatment. Statistical estimates of goodness-of-fit and uncertainties are reported in Table 12 (SI).	66
Table 2: Effective carbon number contributions for relevant functional groups for the estimation of FID response factors based on molecular structure.....	68
Table 9: Complete product selectivities for pyrolysis of cellobiose and cellobiose doped with 1 wt% NaCl solution and with 10 wt% NaCl solution.....	71
Table 10. Summary of pore characterization for Ni-MCM-41, Ni-Beta, and Ni-FAU samples ..	83
Table 11. Fitted parameters to the Butt-Peterson deactivation model (Eq. (1) for Ni-Li-FAU-40.	85
Table 12. Deactivation model parameters for Ni-MCM-41, Ni-Beta, Ni-FAU-6, and Ni-FAU-40 at 258 K.....	88
Table 13. Deactivation model parameters for Ni-MCM-41, Ni-Beta, Ni-FAU-6, and Ni-FAU-40 at 258 K according to a first-order deactivation model.	89
Table 14. Deactivation model parameters for Ni-MCM-41, Ni-Beta, Ni-FAU-6, and Ni-FAU-40 at 258 K according to a second-order deactivation model.....	90
Table 15. Deactivation model parameters for Ni-MCM-41, Ni-Beta, Ni-FAU-6, and Ni-FAU-40 at 258 K without constraint on the deactivation order n and fit by minimizing least squares.....	91
Table 16. Deactivation model parameters for Ni-MCM-41.	93

LIST OF FIGURES

Figure 1: Aldol Condensation of Acetone	17
Figure 2: Mechanism of Aldol Condensation.....	18
Figure 3: Aldol condensation of glycolaldehyde can lead to the formation of branched or linear molecules as a result of keto-enol tautomerization following aldol condensation	20
Figure 4: Butanal aldol condensation over Cu/TiO ₂ in a fixed-bed continuous-flow reactor at 1 bar H ₂	25
Figure 5: Product selectivity following butanal aldol condensation in a pulsed-flow micro-reactor, carried out at 300°C and 30 psig H ₂ by vaporizing 1 µL butanal.	26
Figure 6: Aldol condensation plus HDO of butanal over Cu/TiO ₂ and PtMo/MWCNTs at 300°C and varying hydrogen partial pressures	27
Figure 7: Product carbon distribution resulting from glycolaldehyde aldol condensation over 2% Cu/TiO ₂ followed by HDO over 5% PtMo/MWCNTs under hydrogen pressures of 40 psi and 300 psi.	29
Figure 8: Reaction pathways observed for aldol condensation and hydrodeoxygenation of glycolaldehyde, including side reactions resulting in the formation of decarbonylated products	29
Figure 9: Product carbon distributions followed by HDO alone over 5% PtMo/MWCNTs and by aldol condensation over 2% Cu/TiO ₂ followed by HDO over 5% PtMo/MWCNTs of cellulose pyrolysis vapors at 45 psi H ₂	31
Figure 10: Comparison of product selectivity from sequential aldol condensation and hydrodeoxygenation of cellulose pyrolysis vapors and HDO alone of pyrolysis vapors, carried out at 300°C 350 psi total pressure, 3 bar H ₂ partial pressure.....	32
Figure 11: Aldol condensation over 2% Cu/TiO ₂ followed by HDO of levoglucosenone solution over 5% PtMo/MWCNTs at 45 psi and 300°C	33
Figure 12: Aldol condensation over 2% Cu/TiO ₂ followed by HDO of glycolaldehyde and levoglucosenone solution over 5% PtMo/MWCNTs at 45 psi and 300°C	33
Figure 13. Sequential hydrogenation and self-condensation of levoglucosenone.....	34
Figure 14. Aldol condensation of levoglucosenone and glycolaldehyde	34
Figure 15: Comparison of extrapolated glycolaldehyde (GA) and levoglucosenone (LGO) self-coupling data at 45 psi with GA + LGO data from the aldol condensation plus HDO system	35
Figure 16. Cross-condensation of glycolaldehyde with furfural	36
Figure 17: Aldol condensation over 2% Cu/TiO ₂ plus HDO over PtMo/MWCNTs of HMF and GA+HMF dissolved in methanol under 45 psi H ₂	37

Figure 18: Aldol condensation over 2% Cu/TiO ₂ plus HDO over PtMo/MWCNTs of HMF and GA+HMF dissolved in methanol under 300 psi H ₂	37
Figure 19: Aldol condensation plus HDO of HMF dissolved in methanol under 45 and 300 psi H ₂	38
Figure 20: Aldol condensation plus HDO of GA+HMF dissolved in methanol under 45 and 300 psi H ₂	39
Figure 21: Sequential dehydrations of levoglucosan and keto-enol tautomerization to form levoglucosenone.....	40
Figure 22: Isomerization of levoglucosenone in the presence of water to 5-HMF	40
Figure 23: GC spectrum for pyrolysis of surface-doped HUSY at 300°C. Levoglucosan elutes at the 30 minute mark, levoglucosenone elutes at 20.5 minutes, and 5-HMF elutes at 22.5 minutes.	42
Figure 24: Carbon distribution following pyrolysis of pore-doped HUSY at 300°C. The plotted selectivity is normalized to total recovered carbon; overall carbon balance is ~40%	43
Figure 25. Product selectivity to major products following fast pyrolysis of cellobiose doped with CaCl ₂ , MgCl ₂ , KCl, and NaCl in 1 wt% solutions. Pyrolysis conducted at 500°C in 30 mL/min He.	49
Figure 26. Product selectivity to products grouped by molecular structure following fast pyrolysis of cellobiose doped with CaCl ₂ , MgCl ₂ , KCl, and NaCl in 1 wt% solutions. Pyrolysis conducted at 500°C in 30 mL/min He.	50
Figure 27. Product selectivity to major products following fast pyrolysis of cellobiose doped with CaCl ₂ , MgCl ₂ , KCl, and NaCl in 10 wt% solutions. Pyrolysis conducted at 500°C in 30 mL/min He.	51
Figure 28. Effects of concentration of monovalent cation K ⁺ on product selectivities to major fast pyrolysis products of cellobiose. Pyrolysis conducted at 500°C in 30 mL/min He.....	52
Figure 29. Effects of concentration of divalent cation Ca ²⁺ on product selectivities to major fast pyrolysis products of cellobiose. Pyrolysis conducted at 500°C in 30 mL/min He.....	52
Figure 30. Product distribution following hydrodeoxygenation of fast pyrolysis vapors from cellulose, poplar, hemicellulose-lean residues, and delignified poplar. Pyrolysis was carried out at 500°C in 100 mL/min H ₂ at 300 psi, with hydrodeoxygenation taking place over 5% PtMo/MWCNTs at 300°C.....	54
Figure 31. Ethene oligomerization rates as a function of time-on-stream collected for (a) Ni-MCM-41 (Si/Al = 18, Ni/Al = 0.24) at 243 K, (b) Ni-Beta (Si/Al = 12.5, Ni/Al = 0.28) at 258 K, (c) Ni-FAU-6 (Si/Al = 6, Ni/Al = 0.07) at 258 K, and (d) Ni-FAU-40 (Si/Al = 40, Ni/Al = 0.20) at 258 K. A H ₂ co-feed was present in Ni-FAU experiments as 1% of total flow. Dotted lines represent fits to deactivation models according to a generalized deactivation model (Eq. (3.1)), with best-fit parameters summarized in Table 6.	61

Figure 32. Ethene oligomerization rates as a function of time-on-stream at 258 K for Ni-FAU-40 (Si/Al = 40, Ni/Al = 0.20) at conditions with and without 1% H ₂ co-feed. Dashed lines represent fits to deactivation models according to a generalized deactivation model (Eq. (3.1)), with parameters calculated in Table 7.....	65
Figure 33. N ₂ adsorption-desorption (77 K) isotherm for Ni-MCM-41.	76
Figure 34. N ₂ adsorption-desorption (77 K) isotherm for Ni-Beta.	77
Figure 35. N ₂ adsorption-desorption (77 K) isotherm for Ni-FAU-6.	78
Figure 36. N ₂ adsorption-desorption (77 K) isotherm for Ni-Li-FAU-40	79
Figure 37. Fraction of total surface area contained within a given pore diameter for 0.63 wt% Ni-MCM-41. The bulk of the surface area is contained in pores between 3-5 nm in diameter, with 85% of total surface area contained in pores <5 nm in diameter.	80
Figure 38. Fraction of total surface area contained within a given pore diameter for Ni-Beta. Most of the surface area is contained within pores <1.2 nm diameter, with 70% of total surface area in pores <1.3 nm in diameter.	81
Figure 39. Fraction of total surface area contained within a given pore diameter for Ni-FAU-6. Most surface area is contained within pores of <1.5 nm diameter, with 90% of total surface area in pores <1.9 nm diameter.	81
Figure 40. Fraction of total surface area contained within a given pore diameter for Ni-Li-FAU-40. Surface area is split between micropores and mesopores. Approximately 50% of total surface area lies in micropores with 1.4-1.7 nm diameter, while the remaining 50% of total surface area lies in mesopores with 3.5-10 nm diameter.	82
Figure 41. Ethene oligomerization rates as a function of time-on-stream for (a) Ni-FAU-40 (Si/Al = 40, Ni/Al = 0.20, 0.3 wt. % Ni) and (b) Ni-Li-FAU-40 (Si/Al = 40, Ni/Al = 0.26, 0.5 wt. % Ni), collected at 258 K. Fits to deactivation models are shown in dashed lines. H ₂ was co-fed at a concentration of 1% of the total feed.	85
Figure 42. Ethene oligomerization rates on H-MCM-41 at 258 K and 12-26 bar ethene (P ₀ = 28.4 bar for ethene at 258 K). 0.85 mol ethene g ⁻¹ h ⁻¹ flow at P/P ₀ = 0.42 and 1.9 mol ethene g ⁻¹ h ⁻¹ at P/P ₀ = 0.77 and P/P ₀ = 0.89.	86
Figure 43. Fit of ethene oligomerization data on Ni-MCM-41 at 243 K and 9 bar ethene from Agirrezabal-Telleria and Iglesia to the Butt-Peterson deactivation model (Eq. (3.1)). Data shown is extracted from Figure 5 of Agirrezabal-Telleria and Iglesia [78].	92

ABSTRACT

Biomass and shale gas have been proposed as alternate sources of hydrocarbon fuels, but traditional petroleum refining is not capable of directly converting either the highly oxygenated molecular structure of lignocellulosic biomass or the low molecular weight alkanes of shale gas into liquid fuels. Here, we investigate aspects of aldol condensation and oligomerization to perform C-C coupling of low molecular weight species in biomass pyrolysis vapors and shale gas.

Pyrolysis of woody biomass into C₁-C₉ molecules has demonstrated significant carbon losses away from fuel-range hydrocarbons to C₁-C₃ species following hydrodeoxygenation [1]. Aldol condensation has been proposed as a means of leveraging oxygen functional groups present in the pyrolysis product distribution prior to hydrodeoxygenation in order to couple low molecular weight species such as glycolaldehyde to transform the C₁-C₃ fraction into C₄₊ species. Here, we demonstrate that glycolaldehyde coupling has only a minor effect on aldol condensation of cellulose pyrolysis vapors, and that higher molecular weight species undergo significant reaction over the aldol condensation catalyst. We demonstrate a pathway by which levoglucosan can be converted into levoglucosenone, which then forms higher molecular weight species over the aldol condensation catalyst Cu/TiO₂.

Ni cation sites exchanged onto microporous materials catalyze ethene oligomerization to butenes and heavier oligomers but also undergo rapid deactivation. The use of mesoporous supports has been reported previously to alleviate deactivation in regimes of high ethene pressures and low temperatures that cause capillary condensation of ethene within mesoporous voids. Here, we reproduce these prior findings on mesoporous Ni-MCM-41 and report that, in sharp contrast, reaction conditions that nominally correspond to ethene capillary condensation in microporous Ni-Beta or Ni-FAU zeolites do not mitigate deactivation, likely because confinement within microporous voids restricts the formation of condensed phases of ethene that are effective at solvating and desorbing heavier intermediates that are precursors to deactivation. Deactivation rates are found to transition from a first-order to a second-order dependence on Ni site density in Ni-FAU zeolites with increasing ethene pressure, suggesting a transition in the dominant deactivation mechanism involving a single Ni site to one involving two Ni sites, reminiscent of the effects of increasing H₂ pressure on changing the kinetic order of deactivation in our prior work on Ni-Beta zeolites.

1. ALDOL CONDENSATION OF BIOMASS FAST PYROLYSIS PRODUCTS

1.1 Introduction

1.1.1 Production of Liquid Fuels from Biomass via the H2Bioil Process

Reducing dependence on fossil fuels through the development of alternative energy sources is desirable for reducing dependence on petroleum imports as well as for reducing carbon emissions. Although many strategies have been proposed for the production of electricity from renewable energy, the transportation sector remains reliant on petroleum-based fuels. The US is projected to consume 19.6 million barrels per day of crude oil compared to the production of 10.6 million barrels per day in 2020, with a net import of crude oil expected to be needed through 2040 [2]. Although natural gas, solar, wind, and nuclear power offer relatively clean sources of electricity, none of these are suitable for use as transportation fuels. Liquid fuels are currently safer and cheaper to store and use in vehicles than many proposed alternative fuel sources, such as hydrogen [3]. In addition, the infrastructure for distribution of liquid fuels is already in place, while a gas-based distribution system would require extensive development. Gasification could be used to transform natural gas or biomass into liquid fuels, however gasification followed by Fischer-Tropsch synthesis requires excessive amounts of hydrogen [4,5]. Given these limitations of renewable energy and the advantages of using liquid fuels, the H2Bioil process was proposed by Agrawal and Singh to use solar energy to produce hydrogen, which can then be used in much smaller quantities than in gasification and Fischer-Tropsch to perform reactions to transform biomass into liquid fuel [4]. As a solid, biomass has relatively low energy density due to the abundance of oxygen-containing functional groups in its component polymers cellulose, hemicellulose, and lignin. In H2Bioil, biomass is pyrolyzed and hydrodeoxygenated in order to produce fuels with optimal hydrogen use [4]. A PtMo bimetallic catalyst has already been developed to perform hydrodeoxygenation (HDO), and its selectivity to hydrogenated or dehydrogenated products may be controlled by varying the hydrogen partial pressure. 37.1% of carbon from pyrolysis and HDO of poplar goes to C₄₊ products[1], but 9.6% of carbon is lost as CO, 2.7% is lost as CO₂, 28.5% is lost as char, and 21.7% is lost as C₁-C₃ hydrocarbon products [1] (different feedstocks will give variations in these numbers). If C₄ through C₉ molecules are

considered as being suitable for gasoline, then a significant portion of biomass pyrolysis vapors are unsuitable for liquid fuels. An additional reaction step to take advantage of the presence of oxygen functional groups to lengthen carbon chain lengths would greatly increase the selectivity of the process to product molecules that are in the liquid fuel range.

1.1.2 Fast Pyrolysis of Lignocellulosic Biomass

Biomass itself is composed primarily of three polymers: cellulose, hemicellulose, and lignin. Fast-pyrolysis results in the decomposition of these polymers into smaller molecules; this product stream can be analyzed directly by GC or it can be condensed into a bio-oil. Although the specific makeup of biomass is dependent on the source plant, cellulose and hemicellulose together compose 30-70% by weight of intact biomass [6]. Pyrolysis of cellulose gives high yields towards levoglucosan and its isomers of 50 wt% - 60 wt%; formic acid, glycolaldehyde, furan-based molecules, CO, and CO₂ account for approximately 25 wt% [7]. More specifically, during fast hydropyrolysis of cellulose at 480°C and 17 bar H₂ partial pressure and 10 bar He partial pressure, selectivity towards glycolaldehyde in a collected liquid product has been reported as approximately 13% by weight [8]. During fast pyrolysis of cellulose at temperatures between 480°C and 500°C, selectivity towards glycolaldehyde has been reported as varying between 5% and 10% by weight [7-9]. Hemicellulose pyrolysis products are dominated by 50 wt% cumulative yield towards char, water, and CO and CO₂, but furan-based molecules, acetaldehyde, formic acid, acetic acid, and acetol account for the remainder of the product distribution [10]. Lignin pyrolysis gives 55 wt% yield to char, CO, and CO₂, with the remainder dominated by a variety of phenolic products, as would be expected from the linked aromatic units that compose lignin [11].

Pyrolysis results in the generation of a large number of carbonyl-containing compounds, and consequently aldol condensation has the potential to increase the average carbon number of product molecules. Glycolaldehyde, a C₂ species, is a particularly important component of the cellulose pyrolysis product distribution, makes up approximately 5-10% of the pyrolysis product distribution [8]; more fundamentally, glycolaldehyde is a primary product of cellulose fast pyrolysis resulting from unraveling of the reducing end of cellulose by retro-aldol condensation [12,13]. However, given the complexity of the pyrolysis product distribution, many different aldol condensation reactions are possible, both self-condensation reactions, such as glycolaldehyde-glycolaldehyde condensation to form C₄ species, as well as cross-condensation reactions, for

example between glycolaldehyde and a furfural- or levoglucosan-derived species such as levoglucosenone to form C₈ species.

1.1.3 Hydrodeoxygenation

Hydrodeoxygenation is a key step in the treatment of pyrolysis vapors for the production of liquid fuels. Liquid fuels, composed primarily of hydrocarbons, have much higher energy densities than oxygen-rich biomass; poplar has an energy density of approximately 19 MJ/kg [4,14] compared to an energy density of approximately 46 MJ/kg for gasoline. A PtMo bimetallic catalyst has been reported for the hydrodeoxygenation of oxygenates found in biomass pyrolysis vapors [1,15]. A 5 wt% Pt 2.5 wt% Mo/MWCNTs catalyst has been reported to show complete hydrodeoxygenation of vapors from the fast hydrolysis of cellulose at 300°C under 25 bar H₂ pressure [8]. Similarly, in studies of hydrodeoxygenation of dihydroeugenol, a model compound for lignin, at 23.5 bar H₂ pressure, a PtMo catalyst has been shown to give high yield (>97%) to propylcyclohexane, with 0.7% yield towards propylbenzene [15,16]. These experiments have also been performed at 1 bar H₂, with the result of complete HDO but increased selectivity towards aromatic products over hydrogenated products compared to the high H₂ pressure work [17]. In this work, a 5% PtMo/MWCNTs catalyst is used for all HDO studies, in which Pt and Mo are present in a 1:1 ratio.

1.1.4 Aldol Condensation

Biomass pyrolysis products are rich in oxygen functional groups, and many of the most abundant products contain carbonyl groups. For this reason, aldol condensation is an attractive pathway for upgrading pyrolysis vapors to higher molecular weight species prior to the removal of oxygen functional groups by hydrodeoxygenation.

Aldol condensation is a well-studied reaction with commercial applications. For example, Commercially, a key step in the production of 2-ethylhexanol is the aldol condensation of butyraldehyde, which is catalyzed homogeneously by a basic solution to 2-ethylhexenal [18]. Heterogeneous aldol condensation has also been studied extensively, and is typically done using a metal oxide such as MgO, ZrO₂, TiO₂, or with minerals such as hydroxyapatite (Ca₅ PO₄)₃(OH)) and hydrotalcite (Mg₆Al₂CO₃(OH)₁₆ · 4H₂O) [19–30]. Zeolite materials have also been studied for

aldol condensation, typically with ion-exchanged alkali and alkaline earth metals ion [24,31,32]. Various oxides including ZnO, MgO, MoO₃, B₂O₃, and P₂O₅ have been deposited on ZSM-5 and Y-faujasite to investigate their effects on aldol condensation [33]. It was discovered that among these promoter oxides, all resulted in an increase in the rate of aldol condensation with the exception of B₂O₃ and P₂O₅, which was attributed to the addition of further acidic sites to the zeolites by B₂O₃ and P₂O₅. The increase in rate observed with the other promoters was attributed to an increase in basic sites in the materials following their impregnation [33]. Strongly acidic sites in zeolites have been linked to the formation of coke during aldol condensation [31,33].

Recent work by Wang, Goulas, and Iglesia has shown that mixed Cu/SiO₂ and TiO₂ reduces catalyst deactivation, which was attributed to hydrogenation of alkenal products to more stable alkanals following aldol condensation [25]. A catalyst with similar hydrogenation element, Pd/ZrO₂, was studied by Gurbuz, Kunkes, and Dumesic. This catalyst was capable of performing aldol condensation and hydrogenation of C₅ ketones with total selectivity of approximately 60% to condensation products when operating at 66% conversion [30]. These studies demonstrate that aldol condensation can still take place in the presence of a weak hydrogenation function; in this work, we focus on the use of Cu/TiO₂.

Both acidic and basic sites play important roles in aldol condensation catalysis [25,26,33–36]. It has been found that alkali and alkaline earth metal ions added to MgO increased the number of basic sites on the catalyst according to the base strength of the oxide corresponding to a given promoter ion. Turnover rate was found to be proportional to the surface concentration of base sites [26]. Although adjacent acid-base Ti-O sites are thought to be necessary for this reaction [25], it has been found to proceed with titanol sites in Ti/SiO₂, in which multiple butanal molecules may adsorb at a single Ti site [37]. DFT and experimental evidence showed that tetrahedrally coordinated Ti sites in Ti/SiO₂ are more active than hexacoordinated Ti sites [37]. Rekoske and Barteau found that the anatase phase of titania was a highly selective catalyst for aldol condensation, but suffered from rapid deactivation due to the presence of large adsorbed molecules on the catalyst surface created during aldol condensation [20].

Butyraldehyde and acetaldehyde are frequently studied feeds for aldol condensation [19–21,33,37–40]. Aldol condensation of acetaldehyde leads to the formation of crotonaldehyde, while aldol condensation of butyraldehyde leads to the formation of 2-ethyl-hexenal. Ketones are also able to undergo aldol condensation, and acetone is commonly studied for this reaction. The

condensation products from acetone are mesityl oxide and isophorone (which is formed by cyclization of the double condensation product), shown in Figure 1 [26,41]. Aldol condensation results in the formation of reactive functional groups, and following aldol condensation an aldehyde group remains; many secondary reactions are possible following a single condensation reaction, including a second condensation. This is demonstrated by the formation of isophorone from acetone.

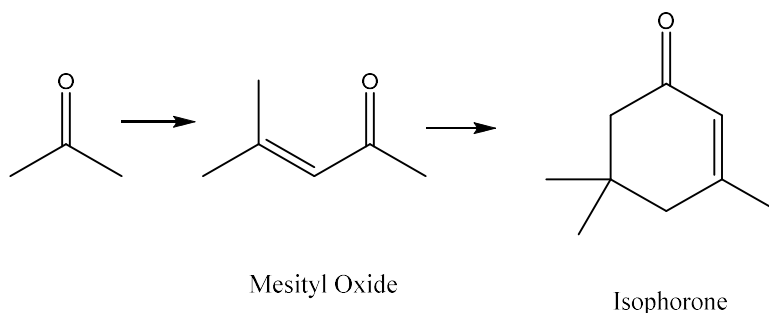


Figure 1: Aldol Condensation of Acetone

The mechanism of aldol condensation, common to both aldehydes and ketones, has been studied extensively [23,25,30,37,42]. The mechanism for the aldol condensation of a generic aldehyde or ketone with a carbon backbone two carbons or longer is shown in Figure 2, where R and R₁ are hydrogen atoms or alkyl groups. On titania, aldol condensation begins with the adsorption of a carbonyl-containing molecule at the oxygen atom to the catalyst. A hydrogen atom from the α-C is abstracted by surface oxygen acting as a base, forming an enolate [43]. Lewis acid sites serve to stabilize the transition state during enolate formation [25]. Additionally, DFT has shown that a methyl group at the α-C, as in propanal, leads to the formation of a more stable enolate as compared to if this R group is just a hydrogen atom, as in acetone [25]. Several studies have shown that enolate formation is the kinetically relevant step in this reaction [23,25], although it has also been suggested that product desorption could be kinetically relevant [21].

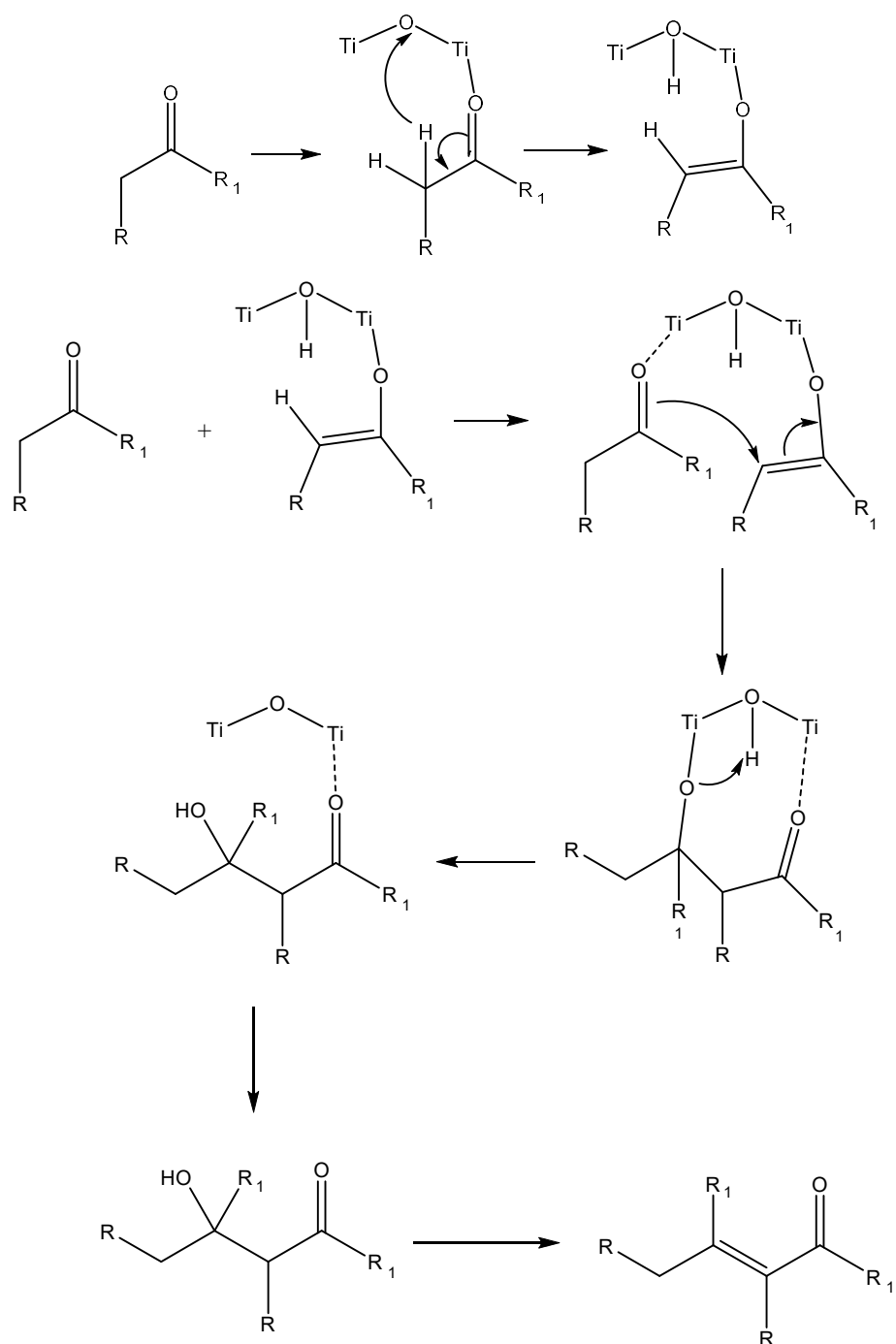


Figure 2: Mechanism of Aldol Condensation

Although aldol condensation is well-studied in literature, aldol condensation of pyrolysis vapors differs in that the molecules composing pyrolysis vapors are structurally different from most model compounds used in literature vapor-phase studies and in that process conditions are constrained by the need to perform additional downstream upgrading reactions following aldol

condensation. To address the second point, aldol condensation in literature is typically studied between 150°C-200°C. Although elevated temperatures will increase the rate of aldol condensation possibly leading to increased formation of poly-condensation products, elevated temperatures will also increase the rate of product desorption, possibly reducing coke formation relative to the lower temperatures. In addition to the differences in temperature, these studies also differ from literature in that this work is conducted in the presence of hydrogen pressures exceeding 1 bar to enable downstream hydrodeoxygenation.

Pyrolysis products contain much higher oxygen densities than are present in most studies in the aldol condensation literature, which typically focuses on one-oxygen aldehydes and ketones such as acetaldehyde, propionaldehyde, butyraldehyde, and acetone for vapor-phase condensation [20,25,26,41]. The additional oxygen functional groups present in pyrolysis vapor molecules may have a significant effect on aldol condensation rates, since the rate-limiting step for vapor-phase aldol condensation over TiO_2 is the formation of an enolate [25]. The presence of a hydroxyl group at the alpha position of the enolate will likely have an impact on its stability as the oxygen atom will attract electron density away from the carbon atom and improve the stability of the intermediate, possibly leading to higher overall rates of aldol condensation. In addition, the aldol condensation product will contain a C-C double bond adjacent to a carbonyl group that could undergo keto-enol tautomerization to form a species containing two carbonyl groups in equilibrium with the single carbonyl molecule. This doubly-carbonylated species can then undergo further aldol condensations to produce species with branched carbon chains, whereas condensation molecules derived from the singly carbonylated species are capable of forming only straight-chain products, assuming that the original reactant contains an aldehyde and not a ketone (as the ketone would naturally form branched species in all cases).

Vapor-phase upgrading of glycolaldehyde to larger molecules is rarely studied. Furan production from glycolaldehyde over HZSM-5 was studied by Kim et. al. using a microreactor system, and products were analyzed by GCMS. Although furan products were observed, total conversion was less than 2% [44]. Studies at such low conversions do not give sufficient information as to the performance of the catalyst under realistic conditions, particularly since a key challenge in aldol condensation is coke formation due to multiple condensations taking place on the surface of a catalyst. The goal here is to develop a catalyst that is capable of performing aldol condensation in series with the hydrodeoxygenation catalyst in the cyclone reactor with

improved selectivity towards fuel-range products with a biomass feed. Although aldol condensation is a well-studied reaction with applications in biomass, little work has been done to apply aldol condensation to pyrolysis products from intact biomass. It is therefore the goal of this work to understand how aldol condensation can be applied to cellulose pyrolysis vapors, and if the carbon lost to C₁-C₃ products can be recovered by the incorporation of an aldol condensation catalyst prior to hydrodeoxygenation.

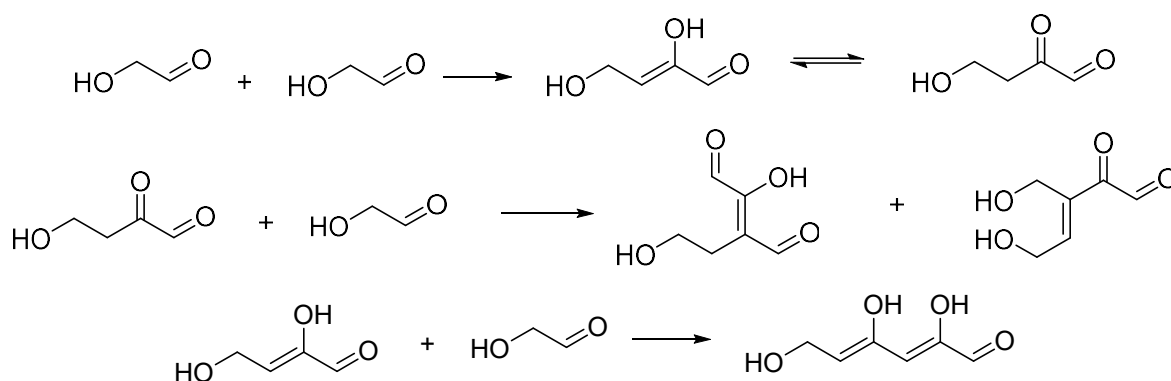


Figure 3: Aldol condensation of glycolaldehyde can lead to the formation of branched or linear molecules as a result of keto-enol tautomerization following aldol condensation

1.2 Methods and Materials

1.2.1 Catalyst Preparation

The Cu/TiO₂ catalyst was synthesized through electrostatic adsorption of copper onto titania. TiO₂ exists in several phases; the two phases of catalytic interest are anatase TiO₂ and rutile TiO₂, which differ in acid-base strength of and distance between pairs of Ti-O sites. Rutile TiO₂ deactivates much more quickly and has a much lower initial reaction rate than anatase TiO₂ during aldol condensation at the conditions of interest; P25 TiO₂ is a mixture of approximately 75% anatase and 25% rutile, and behaves similarly to the anatase phase in aldol condensation [25]. Degussa P-25 TiO₂ (Aeroxide) was first densified by adding excess Millipore water to form a paste. This paste was dried at 120°C overnight and ground and sieved to a particle size of less than 250 μm. Copper (II) nitrate hydrate (99.999%, Alfa Aesar) was dissolved in Millipore water. Ammonium hydroxide was added to this solution until a deep blue solution was formed. TiO₂ and the copper solution were combined in Millipore water and filtered. The solid was dried at room

temperature and at 120°C and then calcined at 300°C for two hours. The catalyst was then sieved to a particle size between 125 μm and 250 μm . Following synthesis, the copper content of the catalyst was determined to be 2 wt% using a PerkinElmer 300 AAnalyst atomic absorption spectrometer. The Cu/TiO₂ catalyst was reduced at 350°C for two hours prior to reaction in 30 mL/min He and 60 mL/min H₂.

The procedure used to synthesize PtMo/MWCNTs has been previously described [1]. It was synthesized through incipient wetness impregnation of multiwalled carbon nanotubes (MWCNTs) (Cheap Tubes, Inc.) of Pt(NH₃)₄(NO₃)₂ (99.995%, Sigma Aldrich) and (NH₄)₆-Mo₇O₂₄·4H₂O (99.98%, Sigma Aldrich). Platinum and molybdenum were in a 1:1 ratio to form the 5% PtMo catalyst. The catalyst is dried overnight and calcined for 2 hours at 450°C. The PtMo/MWCNTs catalyst is reduced at 450°C for two hours prior to reaction. As with the Cu/TiO₂ catalyst, the PtMo catalyst was sieved to a particle size between 125 μm and 250 μm .

1.2.2 Reactors

A pulse micro-reactor was used to study reactions of solid feeds as well as for preliminary studies of liquid model compounds. A CDS 5200 Pyroprobe was used to pyrolyze samples with the resulting vapors passed through a reactor. This unit contains a back pressure regulator capable of operating at temperatures of 300°C which was used to maintain pressures in the reactor between 2 bar and 20.4 bar. The unit was modified from the stock CDS 5200 pyroprobe such that following the reactor, product vapors were passed through the back pressure regulator and directly into a transfer line connected to the GC inlet, allowing for on-line analysis of reaction products without condensation of products. Liquid or solid samples are loaded inside of a 0.25" quartz tube (CDS Analytical) and heated to the desired temperature at a rate of 1.00°C per millisecond. Nitrogen (99.995%, Inweld Corporation) was used to flush air from the quartz tube prior to pyrolysis in a hydrogen (99.999%, Praxair) or hydrogen plus helium (99.995%, Indiana Oxygen) environment. Pyrolysis of solid samples, such as cellulose, was carried out at 500°C using sample masses of approximately 0.3 to 0.5 mg of sample, spread over the interior walls of the quartz tube to minimize sample thickness on the tube walls. For liquid feeds, a single 1 μL droplet was deposited inside of the quartz tube using a 1 μL syringe. Volatile liquid model compounds such as butanal were pyrolyzed at 100°C. Glycolaldehyde was loaded into the pyroprobe as a 19% solution in water by weight and pyrolyzed at 300°C. Low reactant volumes and masses were used in order to minimize

temperature gradients inside the solid or liquid feed, so that the entire sample is assumed to be at the same temperature under pyrolysis conditions.

Pyrolysis vapors were swept into a fixed-bed reactor by a gas stream consisting of pure hydrogen or a mixture of helium and hydrogen. The catalyst was loaded into a stainless steel 1/4" to 1/8" VCR male reducing union (Swagelok, SS-4-VCR-6-DM-2) which serves as the reactor for pyrolysis vapor upgrading. For HDO experiments, this reactor contains approximately 30 mg of 5% PtMo/MWCNTs with a layer of quartz wool above and below the catalyst. Aldol condensation experiments were carried out using 60 mg of 2% Cu/TiO₂ in place of the 5% PtMo/MWCNTs. For dual-bed experiments using both the HDO and aldol condensation catalysts, the HDO catalyst 30 mg of 5% PtMo/MWCNTs was loaded into the bottom of the reactor, with 60 mg of 2% Cu/TiO₂ loaded on top. The two catalyst beds were separated by quartz wool and a stainless steel frit positioned between quartz wool layers of the two catalyst beds in order to prevent catalyst bed mixing. Reactions were carried out at pressures between 30 psig and 350 psig.

Following the reactor, product vapors were passed through a transfer line into an Agilent 7890A GC and 5975C MSD. Products were identified from the MSD using the NIST database. For experiments in which an HDO catalyst was applied, only hydrocarbon products were expected. Therefore, a J&W GS-GasPro column of length 6.2 m was used to separate products. For experiments in which a large amount of methane and ethane were produced, a CO₂ cryogenic valve assembly was used to introduce CO₂ (Liquid Withdraw, Indiana Oxygen) to the GC oven for the purpose of cooling it to temperatures below 35°C and improve separation of these light products. For experiments conducted without HDO catalyst, oxygenates were expected. For these experiments, an Agilent J&W DB-1701 column of length 60 m was used to separate products. A three-way splitter was used to divert a portion of the product stream to the MSD, with the remainder analyzed by an FID. Hydrogen (99.999%, Praxair) was used as the carrier gas.

Carbon balance in the pyroprobe experiments was calculated by determining the product carbon flow rates based on FID peak areas and by measuring the mass of the carbonaceous char residue left following pyrolysis. Prior to pyrolysis, the mass of a solid loaded into the quartz tube is determined by massing the tube first without and then with sample loaded inside using a Mettler-Toledo XS205DU balance. Char masses were obtained by massing the quartz tube following pyrolysis. The carbon contents of intact cellulose and biomass and of the char produced from

pyrolysis of intact biomass were determined by elemental analysis performed by Galbraith Laboratories (Knoxville, TN), and are shown in Table 1.

Table 1. Carbon contents (% by weight) of unpyrolyzed cellulose and poplar samples and of char residue following pyrolysis of these samples.

	Unpyrolyzed	Char
Cellulose	45	81
Poplar	50	76

A continuous flow fixed-bed reactor was used to study the catalyst at conversions less than 100%. A Chrom Tech Series III pump was used to feed butyraldehyde (99.0%, Sigma Aldrich) into the reactor at rates between 0.006 mL/min and 0.063 mL/min. The reactor inlet was heated to 180°C to ensure vaporization prior to contact with the catalyst bed. A gas stream consisting of ultra-high purity hydrogen (99.999%, Praxair), ultra-high purity helium (99.995%, Indiana Oxygen), and argon (99.995%, Indiana Oxygen) was fed into the reactor. Pressure inside the unit is maintained at 350 psi using a back pressure regulator.

The catalyst bed was kept at a temperature of 300.0°C \pm 1.0°C during the reaction. Aldol condensation catalyst was loaded into the unit by packing a layer of mixed catalyst and quartz powder in between a top and bottom layer of quartz wool. Quartz powder was obtained by grinding quartz chips (Quartz Plus, Inc.) to particle sizes between 125 μ m and 250 μ m. Products were split to a condenser and to an Agilent 6890 GC.

Flow to the GC was automatically injected by a valve system in 30-minute intervals from a 3 mL sample loop and a 1 mL sample loop. Flow from the 3 mL sample loop was passed through a Supelco SPB-1 30 m long column to separate oxygenated products prior to entering an Agilent 3-way splitter which was used to split flow between an FID and an Agilent 5973N MSD. Products were identified from the MSD using the NIST database. Flow from the 1 mL sample loop was first passed through a Supelco 12718-U pre-column to remove heavy components from the product stream, then passed through a Supelco Carboxen 1000 packed column, which was used to separate light gases prior to detection by TCD. Helium (99.995%, Indiana Oxygen) was used as a carrier gas. Product quantification was carried out using the FID, for which molar response factors of species were determined using a group contribution method (Appendix A)

Reactions were allowed to continue for approximately eight hours until conversions remained steady within 1% over the course of multiple consecutive GC injections. Butanal flow was turned off and the catalyst was allowed to sit in 50 mL/min H₂ and 75 mL/min He at atmospheric pressure overnight prior to resumption of experiments the following day. Following stabilization of the catalyst over several days until a stable conversion was achieved, conversion was varied by varying the space velocity within the reactor while keeping the partial pressure of each component the same. This data was used to generate the selectivity versus conversion plots shown later.

1.3 Results and Discussion

1.3.1 Aldol condensation of butanal

Aldol condensation of butanal at 300°C and 1 bar H₂ was conducted in the fixed-bed continuous-flow reactor, with results shown in Figure 4. 2-ethyl-hexenal was the major observed product at the conversion studied, with a hydrogenated form, 2-ethyl-hexanal, and a C₁₂ oxygenated product also observed. Although a specific molecular structure could not be identified for the C₁₂ product using EIMS and the NIST database, ions observed in the fragmentation pattern are consistent with a parent molecule with formula C₁₂H₂₀O, the molecular formula of the C₁₂ aldol condensation product of 2-ethyl-hexenal with butanal. Although there are major differences between the pyroprobe and the fixed-bed continuous-flow reactor, these differences can be rationalized by the differences in reactor designs between the two systems. The high ratios of catalyst to reactant mass in the pyroprobe result in complete conversion of reactant molecules, and it is possible that only a single turnover occurs at each active site. Further, the presence of a hydrogen co-feed favors selectivity to hydrodeoxygenation and hydrogenation products which are not observed in the continuous-flow reactor in any significant abundance. Aldol condensation in the pyroprobe is therefore expected to underestimate selectivity to aldol condensation products as compared to a continuous-flow reactor. However, the low reactant volume requirements for the pyroprobe make it an effective tool for studying reactants with structural similarities to true pyrolysis products that are not commercially available in sufficient quantities for experiments in the continuous-flow reactor.

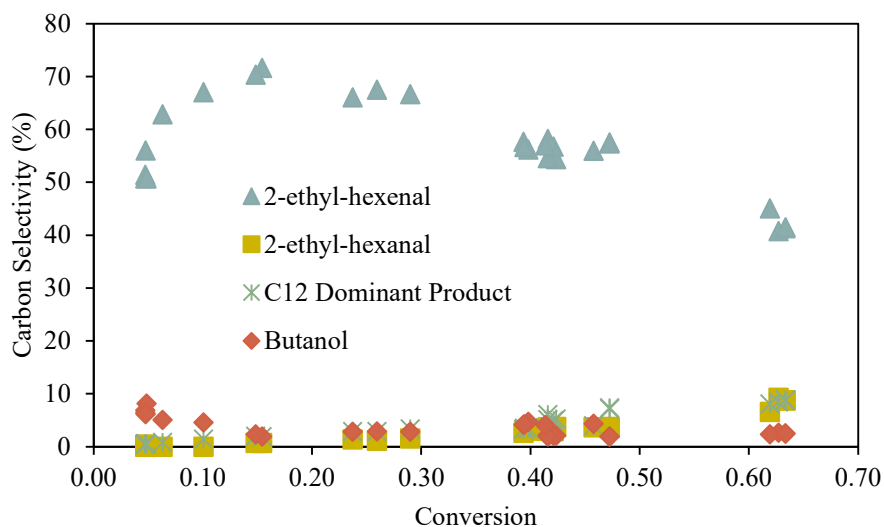


Figure 4: Butanal aldol condensation over Cu/TiO₂ in a fixed-bed continuous-flow reactor at 1 bar H₂

It is not practical to use a continuous flow reactor to study aldol condensation of model compounds for cellulose pyrolysis vapors due to the quantities of material required and the commercial availability of adequate model compounds. Aldol condensation of butanal was therefore also studied in the pulse-flow pyroprobe reactor. Results from aldol condensation alone of butanal at 300°C and 30 psig H₂ in the pulse-flow reactor are shown in Figure 5. Although H₂ is not needed for the aldol condensation reaction, all aldol condensation experiments were carried out in the presence of H₂ since the ultimate goal is to perform sequential aldol condensation and hydrodeoxygenation, and hydrodeoxygenation requires H₂.

In the pyroprobe, no oxygenated compounds were observed in the final product distribution. This is likely due to hydrodeoxygenation and hydrogenation of butanal and of aldol condensation products at the Cu sites in Cu/TiO₂. Since only a pulse of butanal is fed into the system, it is likely that the surface is saturated with hydrogen, resulting in high selectivity towards hydrodeoxygenated products.

Butanal lacks key functionalities present in target molecules in the pyrolysis product distribution, such as the presence of a hydroxyl group at the alpha carbon in glycolaldehyde. Aldol condensation proceeds through a carbocation mechanism, and the presence of this functional group may have an effect on the stability of aldol condensation intermediates; it is therefore critical to study more accurate model compounds for cellulose pyrolysis vapors, including glycolaldehyde.

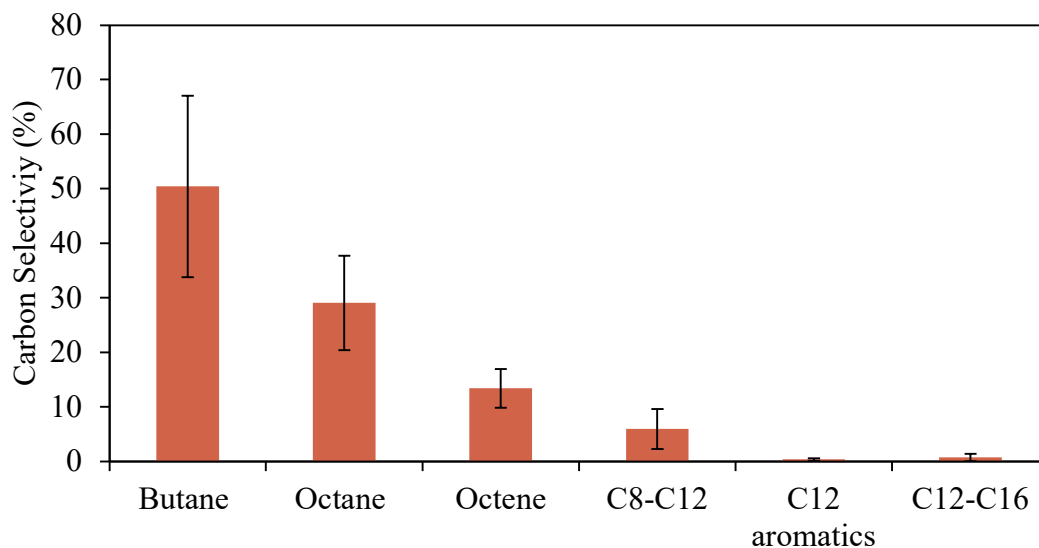


Figure 5: Product selectivity following butanal aldol condensation in a pulsed-flow micro-reactor, carried out at 300°C and 30 psig H₂ by vaporizing 1 μ L butanal.

1.3.2 Sequential Aldol Condensation and Hydrodeoxygenation of Butanal

Sequential aldol condensation and hydrodeoxygenation of butanal were performed over Cu/TiO₂ and PtMo/MWCNTs, respectively, at 300°C and H₂ pressures of 40 psig and 300 psig in the pyroprobe pulse-flow reactor, shown in Figure 6. In all experiments in the pyroprobe reactor involving the HDO catalyst, only alkane products were observed; product selectivities are reported for these experiments as selectivities to alkane products by carbon number. The incorporation of the hydrodeoxygenation catalyst increases the carbon selectivity to C₄ relative to aldol condensation alone at low hydrogen partial pressures, with most carbon detected as C₄ following HDO. Selectivity to C₈ was low (16% of carbon), with significant selectivity to C₅-C₇ products (24% of carbon). C₅-C₇ products are likely formed by decarbonylation and cracking of the C₈ aldol condensation product over PtMo/MWCNTs, a known side reaction [16]. The low collective selectivity to C₅₊ products, which are assumed to all derive from the aldol condensation product, can be attributed to hydrogenation of the carbonyl group in Cu/TiO₂ prior to aldol condensation. Higher selectivity to hydrogenation products in the pyroprobe reactor relative to the fixed-bed continuous flow reactor may be due to high surface coverages of hydrogen in the system, given the presence of a continuous flow of hydrogen through the catalyst bed before and during reactions and the low quantity of reactant in the feed.

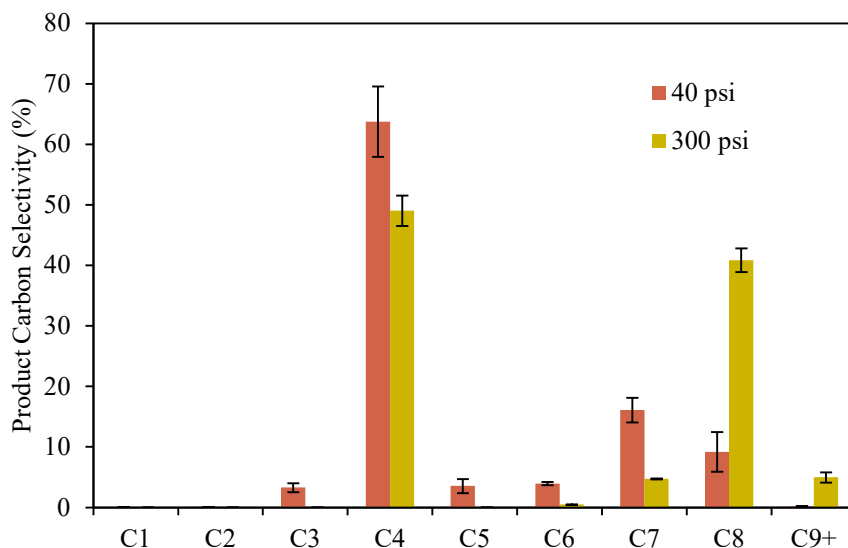


Figure 6: Aldol condensation plus HDO of butanal over Cu/TiO₂ and PtMo/MWCNTs at 300°C and varying hydrogen partial pressures

Increasing the hydrogen partial pressure to 350 psig results in higher selectivity to C₅₊ products, with much higher selectivity to C₈ aldol condensation products (41% of carbon) relative to decarbonylated C₅-C₇ products (5% of carbon). This finding is consistent with previous work with the PtMo catalyst, demonstrating decreased selectivity to decarbonylation and cracking products with increasing hydrogen partial pressure [16]. Increasing hydrogen partial pressure may also drive selectivity towards saturated aldol condensation products before they can form long-chain oligomers and highly unsaturated species that results in the loss of carbon as coke in these catalysts. The incorporation of the HDO catalyst resulted in only a slight decrease in selectivity to C₈ products at low hydrogen pressures. In the absence of an HDO catalyst, approximately 47% of carbon was detected in the form of C₅₊ products, while inclusion of an HDO catalyst reduced this to 40% selectivity to C₅₊ products. Operation at high hydrogen pressures resulted in total carbon selectivity to C₅₊ products of approximately 50%. The primary difference upon inclusion of the HDO catalyst was the difference in product selectivity. For aldol condensation alone, 43% carbon selectivity was observed to C₈ products (butene and butane), with 6% carbon selectivity to C₉₊ products. Inclusion of the HDO catalyst split the C₈ fraction into smaller hydrocarbons, with the 40% carbon selectivity to C₅₊ products split between C₅-C₇ products and C₈ products, assumed to be aldol condensation products or derived from aldol condensation products. Operation at 300 psi H₂ pressure resulted in a near-complete preservation of C₈ aldol condensation products, suggesting

that the previously observed C₅-C₇ species are the products of decarbonylation of the aldol condensation product observed in studies with just the aldol condensation catalyst in the continuous flow reactor.

1.3.3 Sequential Aldol Condensation and Hydrodeoxygenation of Glycolaldehyde

In order to extend the results from butyraldehyde condensation to systems more applicable to cellulose, glycolaldehyde aldol condensation was studied in the pyroprobe reactor. Solutions of 19 wt% glycolaldehyde in water were prepared and injected into a quartz tube, where they were vaporized using the pyroprobe's Pt coil at a rate of 1000°C/s up to a temperature of 300°C for 10 seconds. These vapors were passed over sequential downstream beds containing first Cu/TiO₂ and second PtMo/MWCNTs. The results of these experiments running at 40 psi H₂ and at 300 psi H₂ are shown in Figure 7. As can be seen from these results, 60% of detected carbon in the 40 psi runs was detected in the form of C₃+ aldol condensation products, with the remaining 40% of carbon detected in the form of C₂ products. It is assumed that C₂ products are formed as a result of hydrogenation of the carbonyl group over the Cu function and subsequent deoxygenation over the PtMo downstream catalyst. Such high selectivity to non-condensation products was also observed in the butyraldehyde aldol condensation system. As with that system, it is such high selectivity to non-condensation products may be due to high hydrogen surface coverages driving selectivity towards hydrogenation, as this phenomenon is not observed in a continuous flow reactor. However, these runs only achieved approximately 60% carbon balance. The missing carbon may be present as coke on the surface of the Cu/TiO₂ catalyst. Operation at higher H₂ pressures recovers most of this carbon, achieving over 90% carbon balance. This could be due to hydrogenation of the double bond resulting from condensation, inhibiting further condensations from taking place. The 300 psi H₂ run additionally features significantly higher selectivity to higher hydrocarbon products, most notably C₈ and C₉ products, relative to the 40 psi runs, indicating that these products may be recovered at 300 psi H₂ but not at the lower pressure, 40 psi. High selectivities to products with odd numbers of carbon atoms suggest that significant decarbonylation takes place over the PtMo function. This should be a function of H₂ pressure, but operation at higher H₂ pressures does not significantly decrease selectivity towards decarbonylated products, possibly due to the formation of additional decarbonylation products from carbon that is unrecovered in the low pressure system.

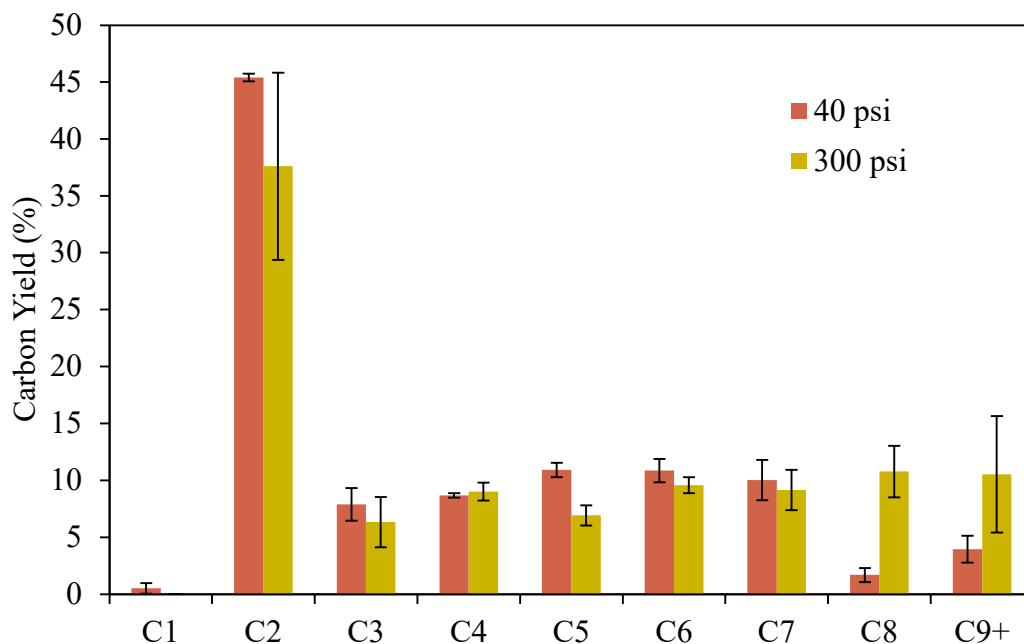


Figure 7: Product carbon distribution resulting from glycolaldehyde aldol condensation over 2% Cu/TiO₂ followed by HDO over 5% PtMo/MWCNTs under hydrogen pressures of 40 psi and 300 psi.

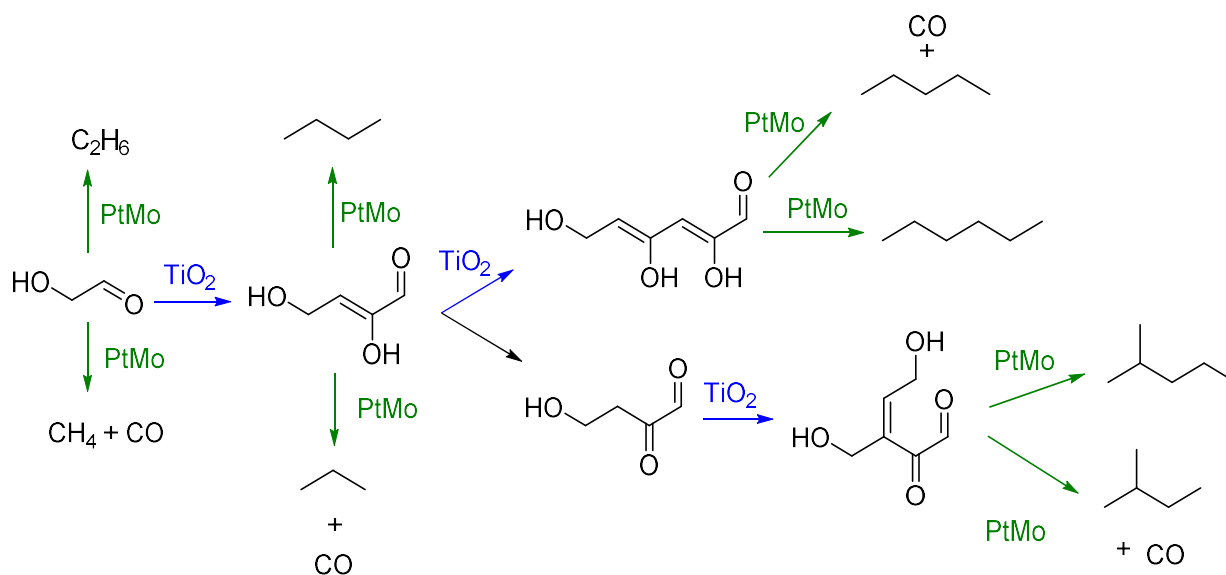


Figure 8: Reaction pathways observed for aldol condensation and hydrodeoxygenation of glycolaldehyde, including side reactions resulting in the formation of decarbonylated products

1.3.4 Sequential Aldol Condensation and Hydrodeoxygenation HDO of Cellulose Pyrolysis Vapors

Cellulose was then pyrolyzed, with the resulting vapors passed through the aldol condensation-hydrodeoxygenation system, with results products shown in Figure 9. Aldol condensation plus hydrodeoxygenation of cellulose pyrolysis vapors leads to increased selectivity to C₇ and C₈ products relative to hydrodeoxygenation alone. It had been hypothesized that glycolaldehyde-glycolaldehyde self-condensation would take place in the cellulose pyrolysis vapor system. Based on these results, it might be expected that 50% of glycolaldehyde would be transformed to aldol condensation products, with the formation of products at every carbon number from C₃ through C₉. However, this is not observed; C₄ selectivity remains unchanged relative to HDO alone. C₁-C₃ selectivity decreases, suggesting that glycolaldehyde still undergoes aldol condensation, but it forms cross-condensation products instead of self-condensation products. The drop in selectivity to C₅ and C₆ corresponding with a rise in selectivity to C₇ and C₈ suggests that C₂-C₅ and C₂-C₆ coupling may take place. Furan-based products, namely the C₅ molecule furfural and the C₆ molecules 5-hydroxymethylfurfural and levoglucosenone, are produced during fast-hydropyrolysis. Although the furfural structure contains aldehyde functionality, it lacks the hydrogen at the α -position relative to the carbonyl group that is necessary to form an enolate and initiate the aldol condensation reaction. Glycolaldehyde therefore would initiate aldol condensation and couple with furfural. These products could also be the result of condensation between glycolaldehyde and levoglucosenone.

The experiments performed in the pyroprobe pulse reactor were also extended to a fixed-bed cyclone reactor, the details of which have been provided in previous work [1,8]. In this work, cellulose was pyrolyzed at 480°C, with carbon selectivities to products reported in Figure 10. Significant carbon was lost with the inclusion of an aldol condensation catalyst, with only 69% carbon balance in aldol condensation plus HDO experiments. It might be speculated that the lost carbon is due to aldol condensation of lighter species which couple and ultimately form coke on the catalyst surface. However, this is inconsistent with the small difference in selectivity to C₁-C₃ products between HDO and aldol plus HDO experiments. 41% selectivity to C₄₊ products is observed in HDO experiments, but only 18% selectivity to C₄₊ products is observed in aldol plus HDO experiments. This suggests that C₄₊ products are susceptible to coking reactions over Cu/TiO₂, possibly due to participation in aldol condensation, but also possibly due to undesirable

side reactions. Although additional work is needed to fully understand the reactions which C_{4+} species undergo over the Cu/TiO₂ catalyst in the cyclone reactor, it is clear from these results that C_1 - C_3 products only play a minor role in these reactions. These results are consistent with the results from the pulse-flow pyroprobe reactor, and together these results suggest that the principal reactions which take place over Cu/TiO₂ in biomass pyrolysis vapors involve higher molecular weight species, such as 5-hydroxymethylfurfural (5-HMF) or levoglucosenone.

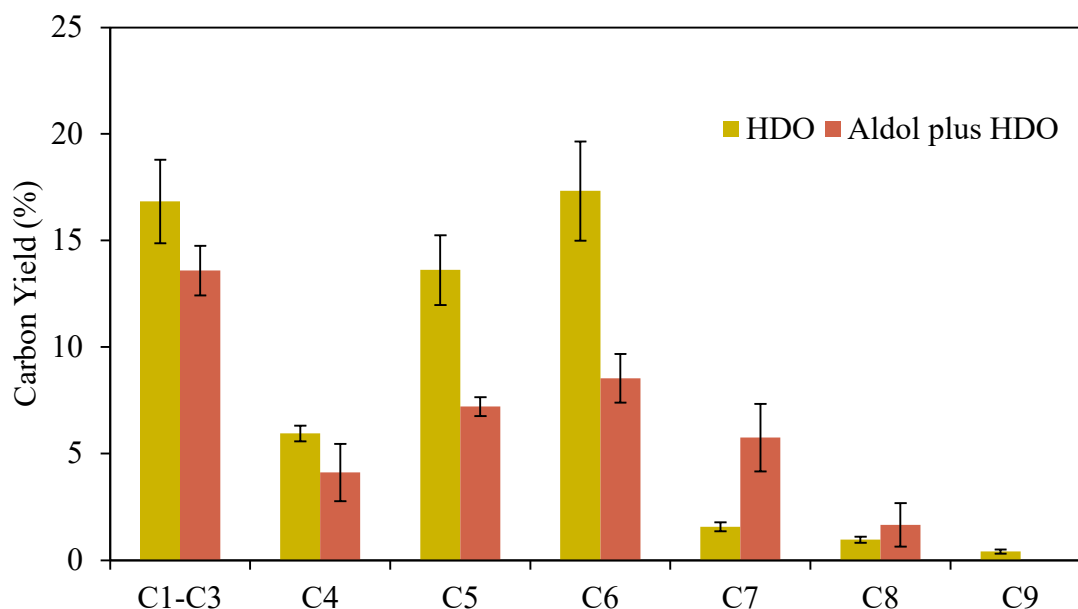


Figure 9: Product carbon distributions followed by HDO alone over 5% PtMo/MWCNTs and by aldol condensation over 2% Cu/TiO₂ followed by HDO over 5% PtMo/MWCNTs of cellulose pyrolysis vapors at 45 psi H₂.

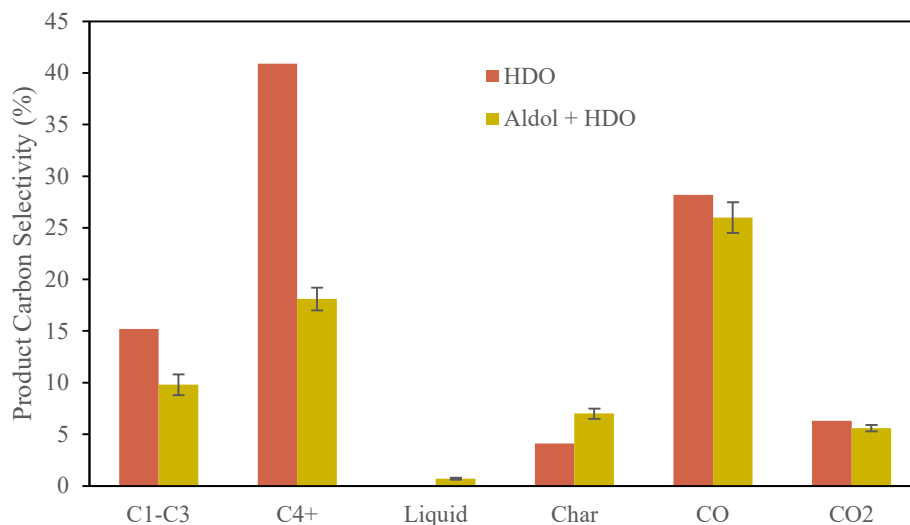


Figure 10: Comparison of product selectivity from sequential aldol condensation and hydrodeoxygenation of cellulose pyrolysis vapors and HDO alone of pyrolysis vapors, carried out at 300°C 350 psi total pressure, 3 bar H₂ partial pressure.

1.3.5 Sequential Aldol Condensation and Hydrodeoxygenation of Levoglucosenone and 5-HMF

In order to study reactions of higher molecular weight carbonyl-containing species, solutions containing levoglucosenone and glycolaldehyde were synthesized in a 1:1 molar ratio in water. Although this molar ratio is not truly representative of cellulose fast pyrolysis vapors, the high relative concentrations of levoglucosenone are expected to favor higher selectivity to cross-condensation products than might be expected in the pyrolysis feed stream, providing an upper-bound on these products. Water was chosen as a solvent due to its ability to dissolve all model compounds of interest. Solutions of levoglucosenone in water and of glycolaldehyde in water were first vaporized and analyzed without catalysis to verify that water does not interact with the model compounds in the vapor phase. The aqueous solution of levoglucosenone and the aqueous solution of glycolaldehyde and levoglucosenone were vaporized and passed over the 2% Cu/TiO₂ plus 5% PtMo/MWCNTs system, with results shown in Figure 11 and Figure 12, respectively.

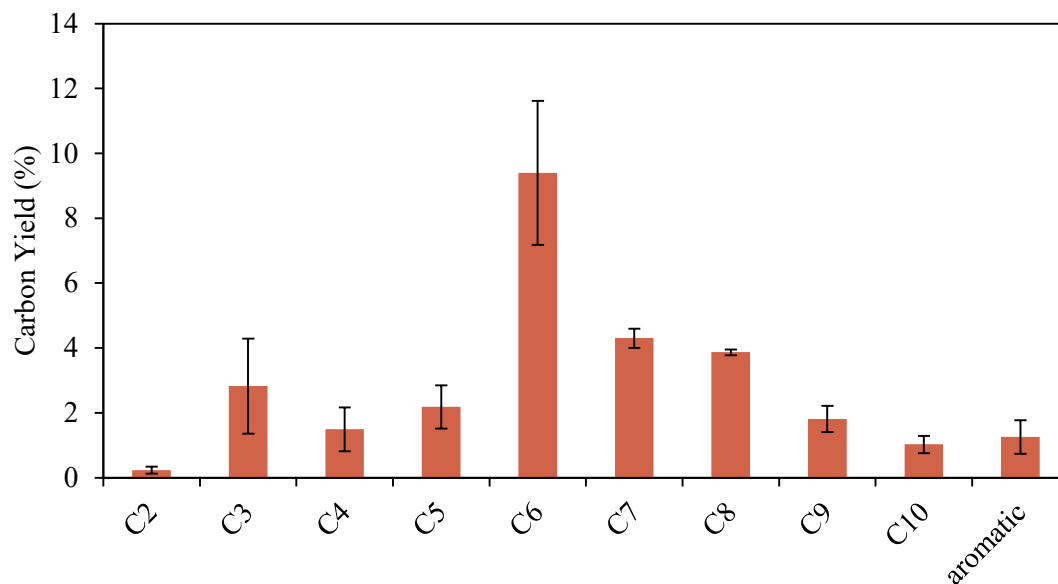


Figure 11: Aldol condensation over 2% Cu/TiO₂ followed by HDO of levoglucosenone solution over 5% PtMo/MWCNTs at 45 psi and 300°C

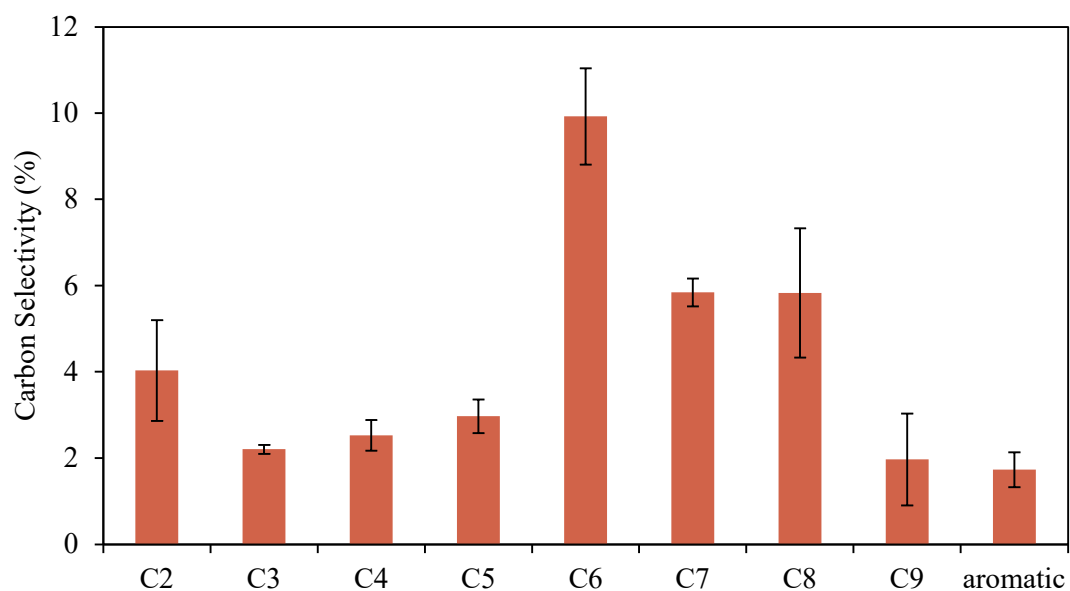


Figure 12: Aldol condensation over 2% Cu/TiO₂ followed by HDO of glycolaldehyde and levoglucosenone solution over 5% PtMo/MWCNTs at 45 psi and 300°C

Although the formation of an enolate intermediate would be sterically unfavorable for levoglucosenone (prohibiting self-condensation), hydrogenation of the C-C double bond in

levoglucosenone could allow for the formation of an enolate, and this species might undergo aldol condensation, as in Reaction 4. No C₁₂ product was observed following aldol condensation and hydrodeoxygenation, but a wide range of lighter products were observed, which could result from cracking reactions on the C₁₂ species. The presence of C₇₊ products indicates that C-C coupling does take place in this system, and the low carbon balance (approximately **give number here**) for these runs suggests that significant carbon deposits may exist on the catalyst. We speculate that a C₁₂ aldol condensation product is formed, but does not survive to detection, either due to its propensity for coke formation or due to extensive C-C bond cleavage within the catalyst beds. The product carbon distribution for the glycolaldehyde-levoglucosenone solution is very similar to that of the levoglucosenone solution. In the mixed solution, higher selectivity to C₂ products is observed, likely a result of HDO of glycolaldehyde as was observed previously in pure glycolaldehyde experiments. Increased selectivity to C₄, C₇, and C₈ products is also observed, consistent with glycolaldehyde self-condensation and glycolaldehyde-levoglucosenone cross-condensation, with downstream decarbonylation accounting for the formation of C₇ products.

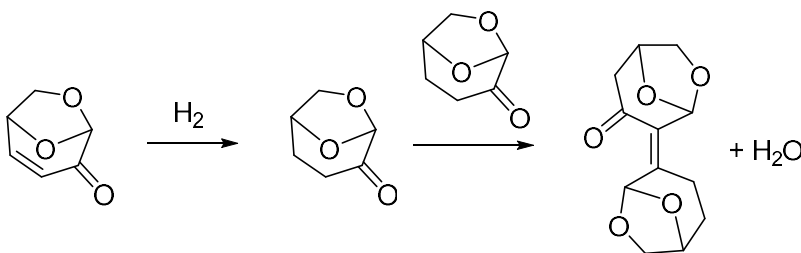


Figure 13. Sequential hydrogenation and self-condensation of levoglucosenone

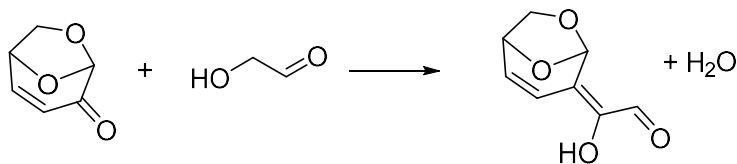


Figure 14. Aldol condensation of levoglucosenone and glycolaldehyde

However, the similarities between the two product distributions makes it difficult to distinguish between self- and cross-condensation, and so results from the glycolaldehyde self-condensation experiments shown in Figure 7 were combined with results from the levoglucosenone self-

condensation experiments shown in Figure 11 and extrapolated to glycolaldehyde and levoglucosenone concentrations equal to those found in the glycolaldehyde-levoglucosenone solution, then plotted alongside the results shown in Figure 12, resulting in the plot in Figure 15. Self-condensation alone results in a product distribution very similar to the product distribution from the mixture. When glycolaldehyde and levoglucosenone are both present, slightly higher selectivity to C_8 is observed at the expense of selectivity to C_{10+} and C_3 products, consistent with cross-coupling between glycolaldehyde and levoglucosenone. The small size of the difference between these two plots suggests that either self-coupling dominates or self- and cross-coupling yield identical products following treatment by the HDO catalyst.

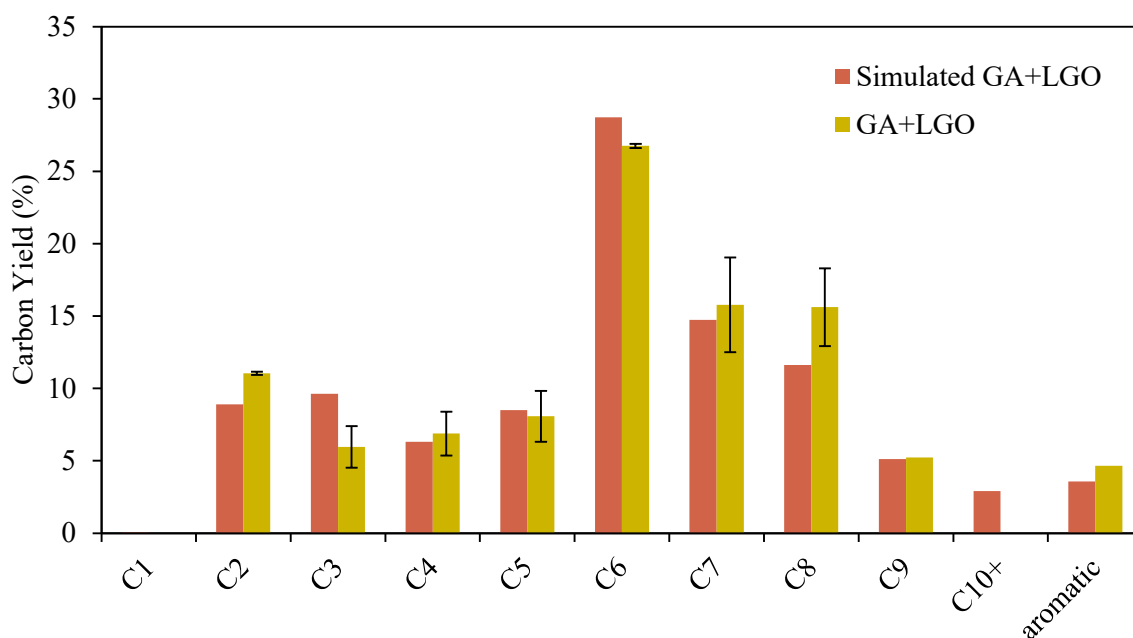


Figure 15: Comparison of extrapolated glycolaldehyde (GA) and levoglucosenone (LGO) self-coupling data at 45 psi with GA + LGO data from the aldol condensation plus HDO system

Based on the aldol condensation work with cellulose, it is important to understand which reactions may take place between furanic compounds and glycolaldehyde. In order to investigate this, additional experiments were performed on the pyroprobe reactor using 5-HMF and glycolaldehyde.

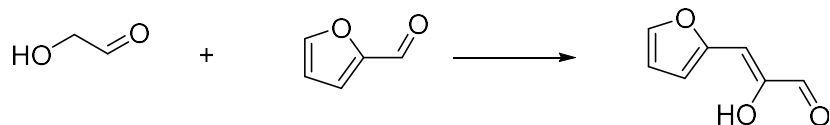


Figure 16. Cross-condensation of glycolaldehyde with furfural

Experiments examining glycolaldehyde and levoglucosenone were performed by making aqueous solutions of these molecules in water and passing these solutions over the aldol condensation-hydrodeoxygenation system. However, 5-HMF forms excessive amounts of char in the presence of water, and so solutions of 5-HMF and glycolaldehyde in methanol were prepared. A solution containing 11.6 wt% 5-HMF dissolved in balance methanol and a solution containing 6.8 wt% GA and 13.9 wt% 5-HMF dissolved in balance methanol were both passed through the Cu/TiO₂ + PtMo/MWCNTs system in order to examine their behavior in the presence of an aldol condensation catalyst. Based on the work shown previously involving glycolaldehyde condensation at varying H₂ pressures, these experiments were carried out at 45 psi H₂ and at 300 psi H₂ in order to determine whether H₂ pressure has any effect on coke formation and on cross- vs. self-coupling in the HMF-GA system. Three runs were performed for each solution at each condition. The results are shown in Figure 17 and Figure 18. Methanol-derived methane is not observed in high abundance in these experiments, possibly due to rapid evaporation of methanol from the 1 μL droplets used in these experiments. All methane observed is assumed to be derived from glycolaldehyde and HMF. This assumption then yields an upper limit on the carbon balance of these experiments. Methanol is assumed to not react with either glycolaldehyde or 5-HMF in this system due to its lack of aldehyde functionality. From this data, it can be seen that only very small amounts of >C₆ are produced in both the 45 psi H₂ system and the 300 psi H₂ system. However, the carbon balances for these runs are low, as shown in Table 2. This suggests that aldol condensation could be taking place, but condensation products are not desorbing from the catalyst surface, instead remaining as coke. Increasing hydrogen pressure to 300 psi does not significantly increase C₇₊ yields; despite an increase of 20% in carbon recovery, most of the increase is due to increased C₆ yield. One possible explanation is that the furfural structure may be susceptible to additional polymerization reactions that lead to coke formation, and any aldol products that are formed also go to coke formation. At elevated hydrogen partial pressures, more C₆ is recovered because more furan rings are hydrogenated before these polymerizations can take place.

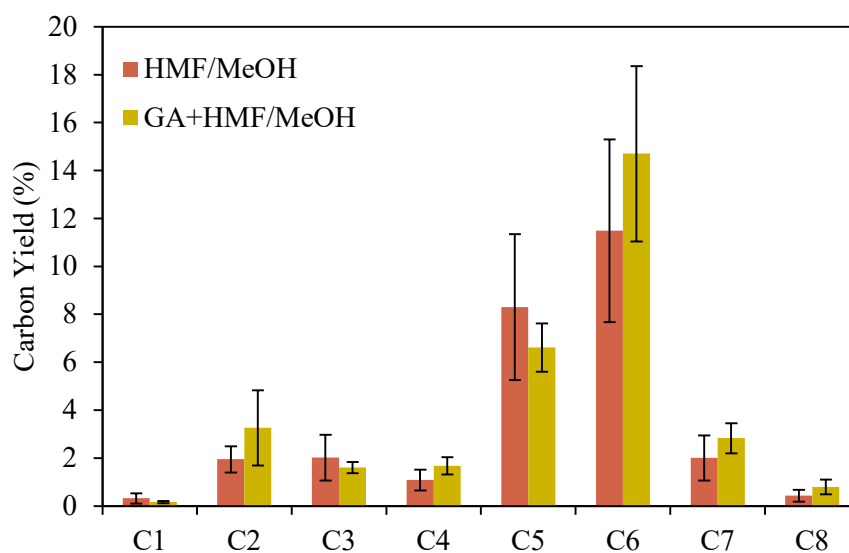


Figure 17: Aldol condensation over 2% Cu/TiO₂ plus HDO over PtMo/MWCNTs of HMF and GA+HMF dissolved in methanol under 45 psi H₂

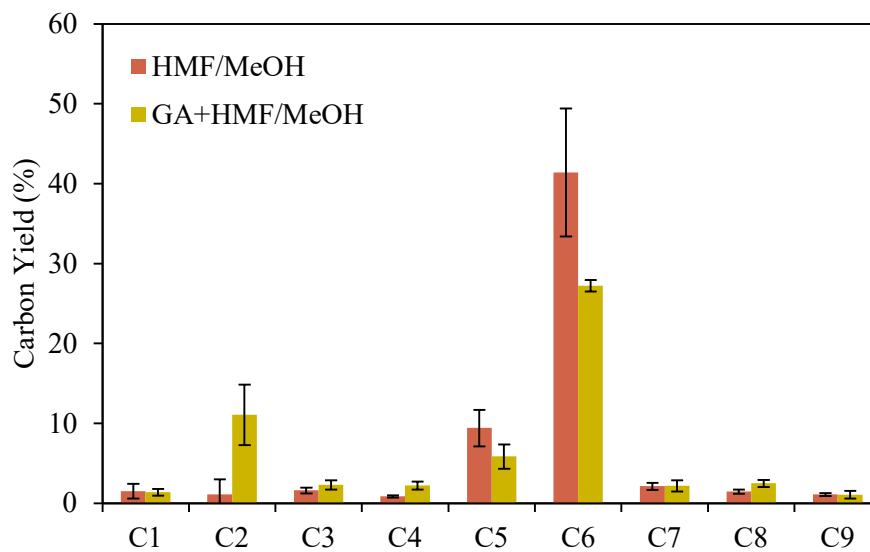


Figure 18: Aldol condensation over 2% Cu/TiO₂ plus HDO over PtMo/MWCNTs of HMF and GA+HMF dissolved in methanol under 300 psi H₂

Table 2: Carbon balances for aldol condensation over 2% Cu/TiO₂ plus HDO over PtMo/MWCNTs of HMF and GA+HMF dissolved in methanol

	45 psi H ₂	300 psi H ₂
HMF	27.6 ± 10.1	60.6 ± 12.4
GA + HMF	31.7 ± 7.4	55.7 ± 5.0

This data can be re-plotted to more directly examine the effects of hydrogen pressure on the reaction in Figure 19 and in Figure 20

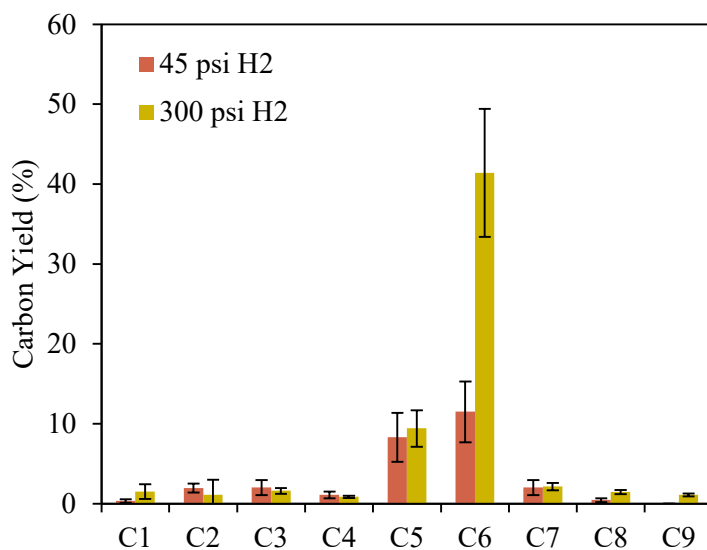


Figure 19: Aldol condensation plus HDO of HMF dissolved in methanol under 45 and 300 psi H₂

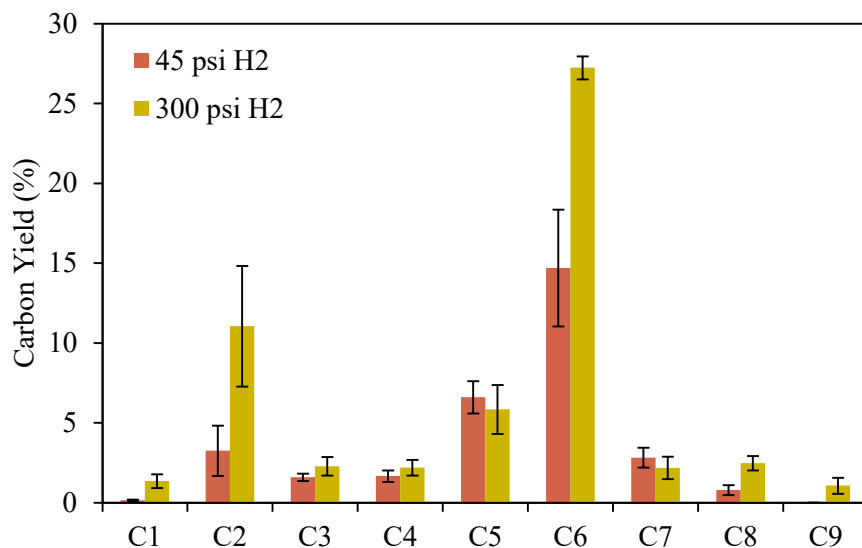


Figure 20: Aldol condensation plus HDO of GA+HMF dissolved in methanol under 45 and 300 psi H₂

The pyroprobe has been inadequate to study aldol condensation of HMF with glycolaldehyde. It is possible that this is due to the non-steady-state condition of the pyroprobe. Rapid deactivation of the Cu/TiO₂ catalyst could be taking place in the presence of HMF.

1.3.6 Dehydration of Levoglucosan

Although this work has sought to increase the C₁-C₃ fraction to C₄+ molecules, the ultimate goal of gasoline and diesel-range products will require upgrading of the C₄-C₆ fraction to higher carbon number products. Towards that end, it is vital that systems be developed that can upgrade levoglucosan, the major product of cellulose fast pyrolysis. Levoglucosan is a relatively stable product of fast hydrolysis, and does not have functionality that is readily susceptible to C-C coupling under the reaction conditions being considered here. As a result, in the current aldol condensation-hydrodeoxygenation system, levoglucosan is simply deoxygenated, leaving a C₆ hydrocarbon if no side reactions take place. Two competing pathways have been shown to dominate pyrolysis: unraveling and hydroxymethylene-assisted glycosidic bond cleavage (HAGBC) [12,45]. Levoglucosan is produced via HAGBC and glycolaldehyde is produced via the unraveling mechanism. Glycolaldehyde has been shown to readily undergo aldol condensation to form heavier hydrocarbons; suppression of levoglucosan formation in favor of glycolaldehyde

could result in an overall increase in C₇₊ hydrocarbon yield following aldol condensation and hydrodeoxygenation. In the absence of a strategy to suppress levoglucosan formation, levoglucosan must be activated so that it can undergo C-C coupling reactions (such as aldol condensation) in order to form C₇₊ products.

Levoglucosan lacks carbonyl groups that could be active for aldol condensation to increase the chain length of its derived hydrocarbons. However, it contains many hydroxyl groups which may be dehydrated to ultimately result in the formation of aldehyde or ketone functional groups, which can then undergo aldol condensation. Activating reactions for this purpose have been conducted in literature. Catalytic pyrolysis of cellulose has been conducted using sulfated ZrO₂, sulfated TiO₂-Fe₃O₄, and with ionic liquids to produce levoglucosenone [46–48]. A strongly acidic catalyst is needed to dehydrate levoglucosan to levoglucosenone [46,48].

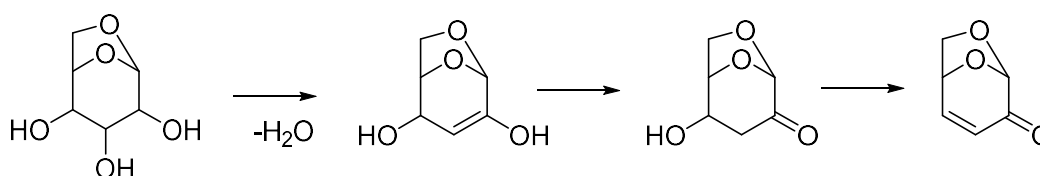


Figure 21: Sequential dehydrations of levoglucosan and keto-enol tautomerization to form levoglucosenone

However, levoglucosenone has been shown to isomerize to 5-HMF. It has been proposed in aqueous-phase literature that levoglucosenone isomerization is a Bronsted-acid catalyzed reaction analogous to the Lewis-acid catalyzed glucose isomerization reaction [49].

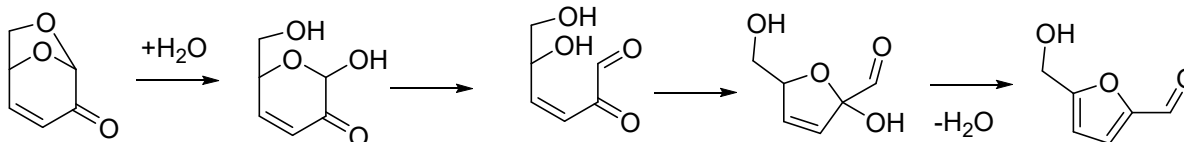


Figure 22: Isomerization of levoglucosenone in the presence of water to 5-HMF

Although levoglucosenone has ketone functionality, it cannot self-couple through aldol condensation; it is sterically hindered from forming an enolate in the ring structure due to the lack of valid sites for C-C double bond formation. Cu in the Cu/TiO₂ catalyst can play two roles in the levoglucosenone system: it was originally intended to hydrogenate aldol condensation products to

reduce coke formation, but it can additionally hydrogenate the levoglucosenone ring double bond to permit the formation of the required enolate for aldol condensation, enabling self-coupling to take place. Alternatively, glycolaldehyde could form the enolate and couple with levoglucosenone to form higher carbon chain length molecules to form a C₈ backbone molecule. A strongly acidic catalyst might transform levoglucosan present in the cellulose pyrolysis feed stream to levoglucosenone, allowing aldol condensation to couple levoglucosan-derived products with glycolaldehyde.

Levoglucosan-doped HUSY was prepared in two ways, beginning with commercially available HUSY with Si/Al = 40. In the first, levoglucosan was dissolved in water and was added to the HUSY via incipient wetness impregnation, giving doped zeolite that will be referred to as “surface-doped”. In the second, HUSY was first baked at 350°C for 4 hours in order to remove water trapped in the zeolite pores prior to the incipient wetness impregnation procedure, giving a sample that will be referred to as “pore-doped”. It is hypothesized that most levoglucosan remains on or near the surface of the surface-doped HUSY particles, whereas in the pore-doped HUSY particles it is hypothesized that levoglucosan molecules penetrate deeper into the particles. Following levoglucosan loading, the catalyst was dried at 60°C overnight and then sieved to 125-250 µm particle sizes. The doped HUSY was then loaded into the py-GCMS unit and heated to 300°C at a rate of 1000°C/s for a hold time of 10 s. Product vapors were separated using a DB-1701 column and analyzed using FID and EIMS. The mass of doped HUSY was recorded both before and after reaction in an effort to quantify the amount of carbon remaining in the zeolite. However, these measurements revealed substantial mass loss exceeding input levoglucosan, indicating that catalyst itself was lost within the instrument during the experiment and could not be recovered for massing. As a result, the overall carbon balance could not be closed; substantial discoloration indicative of coking was observed on the used catalyst, but an accurate mass of that coke could not be collected. The product selectivity in these experiments is shown in Figure 23 for the surface-doped sample and in Figure 24 for the pore-doped sample. From this data, the visually observed coking could be due to degradation of furan-based dehydration reaction products. Many furfural derivatives were observed in minor abundance among reaction products. Interaction between furfural-derived products and water is known to lead to polymerization and char formation [50].

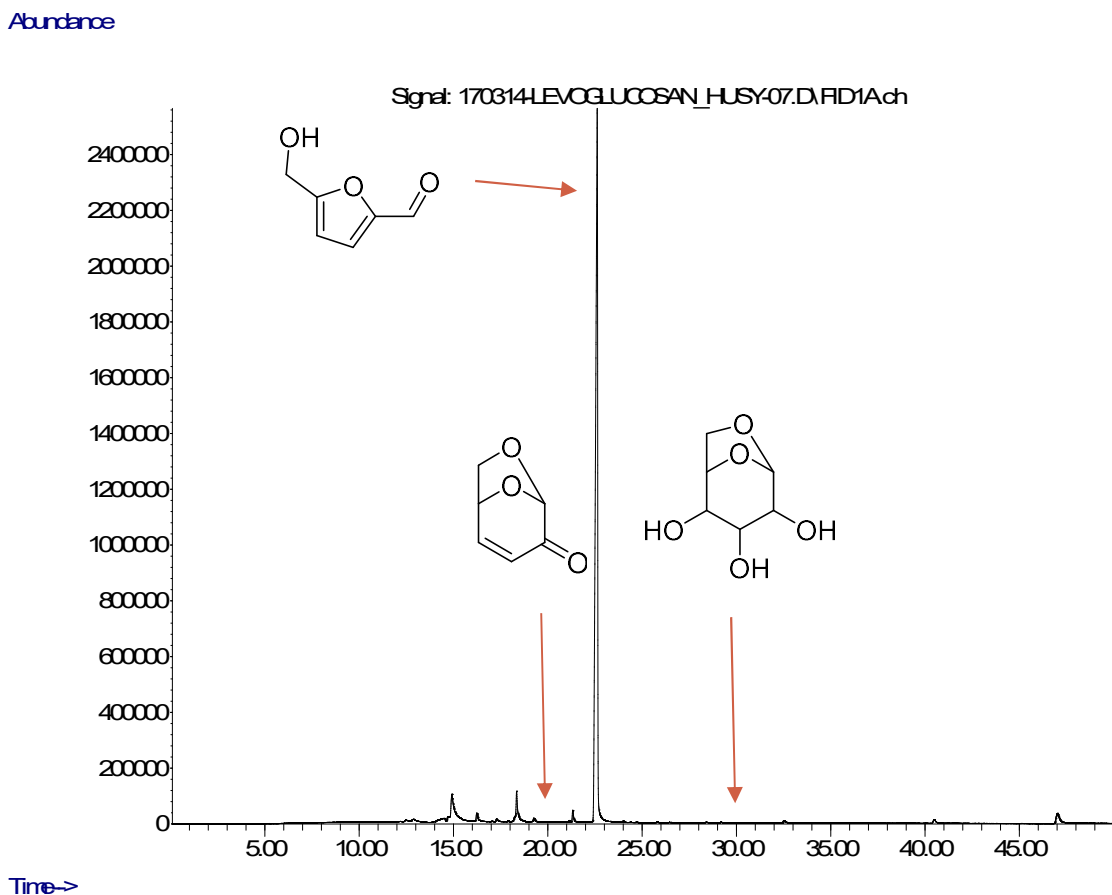


Figure 23: GC spectrum for pyrolysis of surface-doped HUSY at 300°C. Levoglucosan elutes at the 30 minute mark, levoglucosenone elutes at 20.5 minutes, and 5-HMF elutes at 22.5 minutes.

These results demonstrate that levoglucosan is dehydrated over HUSY. However, levoglucosenone is not detected in the surface-doped samples, and instead 5-HMF is the dominant observable product, with minor peaks associated with furfural-based molecules. In the pore-doped samples, levoglucosenone is observed as the dominant observable species, with a number of furfural-based products observed (but notably not 5-HMF). To explain this, it is hypothesized that the isomerization of levoglucosenone to 5-HMF occurs readily at the surface of the catalyst, but it may be inhibited within the pores of the zeolite. Non-HMF furanic species are observed, and thus it is speculated that HMF is formed but either remains trapped in the zeolite pores or is completely decomposed to other furanic products or coke precursors. Levoglucosenone that is formed escapes the catalyst surface and is flushed out of the tube before it can adsorb onto the catalyst surface and undergo further reaction.

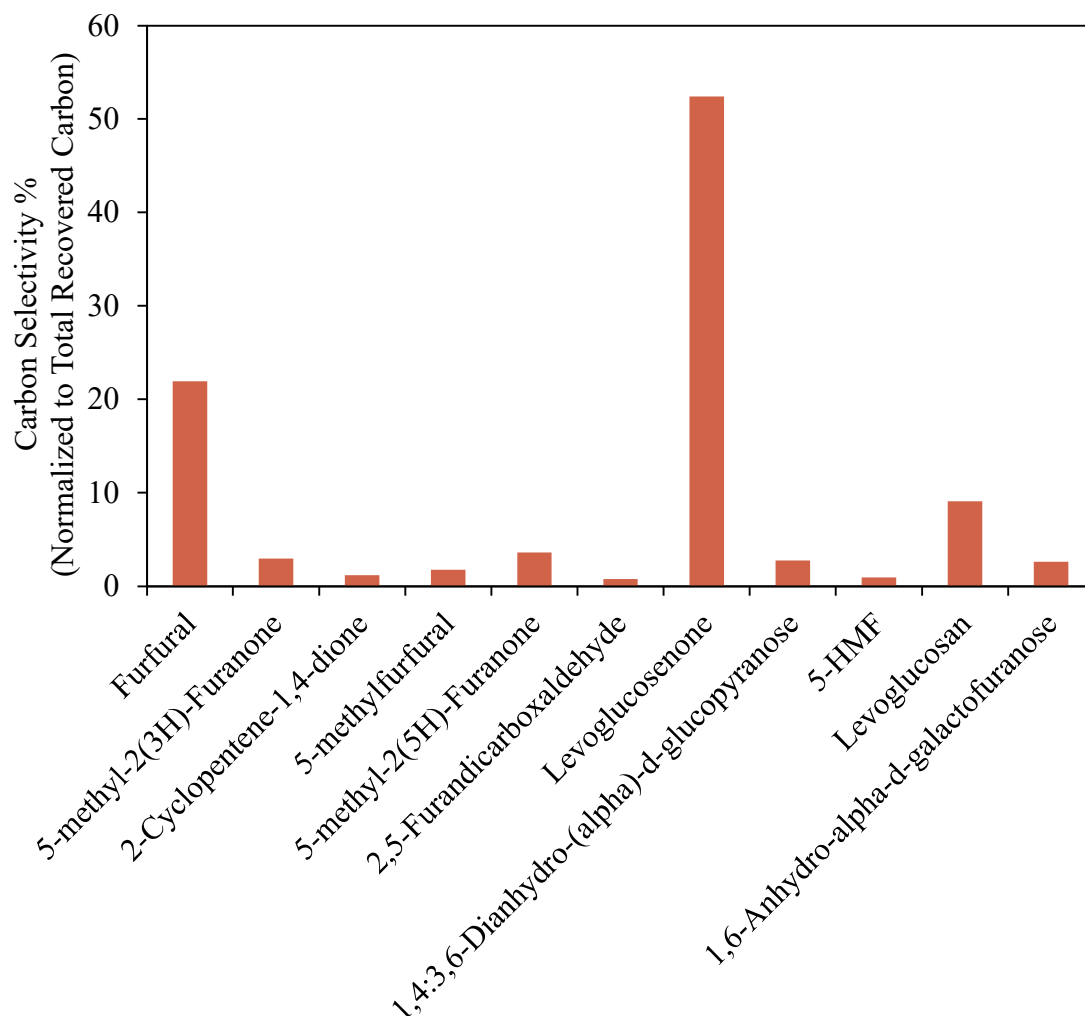


Figure 24: Carbon distribution following pyrolysis of pore-doped HUSY at 300°C. The plotted selectivity is normalized to total recovered carbon; overall carbon balance is ~40%

These results may motivate future work to develop a three-reactor system for upgrading cellulose fast pyrolysis vapors, in which dehydration converts high molecular weight species such as levoglucosan into levoglucosenone, then aldol condensation couples dehydrated products into higher molecular weight species and finally hydrodeoxygenation removes oxygen from the products. However, the effect that the incorporation of a dehydration catalyst would have on the other components of the pyrolysis product stream is currently unknown. The formation of coke on a dehydration catalyst could result in greater overall carbon losses than any gains in C₄₊ selectivity

achieved by the implementation of a dehydration-aldol condensation system relative to the solely HDO system.

1.4 Conclusions

It has been demonstrated that the pyroprobe pulse reactor can be used to screen for aldol condensation of individual aldehyde and ketone species which may be present within biomass pyrolysis vapors. However, application of the aldol condensation catalyst system to cellulose pyrolysis vapors does not result in an increase in C_{4+} selectivity relative to C_2 and C_3 selectivity, as would be expected if aldol condensation of light oxygenates readily took place. Rather, selectivity to C_6 species was decreased with a slight increase in selectivity to C_{7+} products. This suggests that higher molecular weight species participate in reactions over Cu/TiO₂. Experiments with levoglucosenone and 5-HMF have revealed that levoglucosenone passed over Cu/TiO₂ results in the formation of higher molecular weight species, a surprising result given that levoglucosenone is not expected to form the mechanistically required enolate for aldol condensation. The incorporation of a Cu hydrogenation promoter, originally intended to promote catalyst stability, likely enables aldol condensation of levoglucosenone by first hydrogenating the C-C double bond and allowing for the formation of an enolate. This suggests new pathways for upgrading biomass pyrolysis vapors in which selectivity to levoglucosenone is increased by the incorporation of a dehydration catalyst to transform the primary pyrolysis product levoglucosan to levoglucosenone prior to exposure to an aldol condensation catalyst. However, significant work is still needed to fully understand the role of aldol condensation in upgrading biomass pyrolysis vapors. Model compounds which can adequately simulate the structures of species present in biomass pyrolysis vapors need to be studied in a continuous flow reactor in order to measure the kinetics of aldol condensation and determine the extent of carbon accumulation on the catalyst, which has not been considered in the studies on the pyroprobe pulse reactor.

From these results, it can be seen that aldol condensation is effective at transforming key species contained within cellulose fast pyrolysis vapors containing carbonyl groups into higher chain hydrocarbons. Glycolaldehyde readily undergoes aldol condensation to form higher molecular weight species over Cu/TiO₂. However, cellulose pyrolysis vapors are far more complex, and the key aldol condensation reactions which take place in that system involve higher molecular weight species, most likely levoglucosan and furfural-derived species, which undergo aldol

condensation reactions both with themselves and with lighter molecular weight species such as glycolaldehyde.

2. ORIGINS OF CHAR FORMATION

2.1 Introduction

Fast hydropyrolysis of poplar leads to a carbon loss of 28.5% in the form of char [1]. This represents the single largest carbon loss during fast pyrolysis, and it is therefore desirable to understand the sources of char formation. Here, we consider char formation as a consequence of the chemical structure of biomass and char formation as a consequence of reactions catalyzed by inorganic impurities within biomass.

2.1.1 Effect of inorganic impurities

Cellobiose has been previously used as a model compound for cellulose in studies examining the mechanisms of fast pyrolysis [12,13,51], and it has been shown that mechanistic conclusions arrived at using cellobiose are consistent with cellulose pyrolysis results. Cellobiose pyrolysis has been found to proceed through two major pathways, hydroxymethylene-assisted glycosidic bond cleavage (HAGBC), resulting in the formation of levoglucosan, and unraveling of the reducing end by retro-aldol condensation, resulting in the formation of glycolaldehyde [12,45]. The use of cellobiose allows for more controlled fast pyrolysis, and allows for the use of Py-MS studies to more rigorously investigate the mechanisms by which inorganic species influence pyrolysis mechanisms. Cellobiose was therefore doped with several inorganic salts in order to investigate the effect of these species on char formation and on the pyrolysis product distribution. Inorganic alkali species such as NaCl, KCl, CaCl₂, and MgCl₂ are known to lead to increased yields of char during cellulose fast pyrolysis [10,11,52]. Here, we quantify the effect of such inorganic dopants on cellobiose fast pyrolysis, results which can be used to rationalize mechanistic studies of cellobiose fast pyrolysis using mass spectroscopy.

2.1.2 Influence of biomass components on char formation

Of the three main components of lignocellulosic biomass, cellulose is not known as a major contributor to char formation, evidenced by much higher char yields from intact biomass than from cellulose alone [1,7,52,53]. Lignin is known to be a major contributor to char formation, but the role of hemicellulose in char formation is obscured by the lack of adequate model compounds for

hemicellulose. Studies of char formation from xylan are convoluted by the presence of inorganic impurities in xylan, often in extremely high concentrations. The methods used to extract hemicellulose from biomass and create model compounds for hemicellulose often result in extremely high concentrations of alkali in the resulting xylans. Using ICP-MS, commercially available hemicellulose xylan (Carbosynth) was found to contain 14400 $\mu\text{g/g}$ sodium, whereas poplar was found to contain 84 $\mu\text{g/g}$ sodium. The high sodium concentration in xylan is a consequence of the harsh alkali treatment used to extract xylan from biomass. There is therefore a need to develop materials free of inorganic matter which allow us to elucidate the role of hemicellulose in char formation. Here, various pretreatments are used to selectively extract hemicellulose or lignin from intact poplar, and by their absence, we examine their influence on char yields.

2.2 Materials and Methods

2.2.1 Preparation of Inorganic-Doped Cellobiose

Doped cellobiose samples were prepared by incipient wetness impregnation of cellobiose (D-(+)-Cellobiose, >98%, Fluka Chemicals) with solutions of NaCl (Fischer Chemicals, >99.9%), KCl (J. T. Baker, 100%), CaCl_2 (anhydrous, Mallinckrodt, >94.7%), and MgCl_2 . The dopant solutions contained either 1 wt% or 10 wt% of the dopant salt dissolved in deionized water. Following doping, samples were dried overnight in air at 80°C. These samples are hereafter referred to by the concentration of dopant in the solution. For example, the sample labeled “1% NaCl” refers to cellobiose doped with a 1 wt% solution of NaCl dissolved in water.

2.2.2 Preparation of Hemicellulose-free and Lignin-free Samples

Hemicellulose was extracted from poplar biomass of the genus *Populus trichocarpa*, grown at Purdue, in order to study its effects on char formation. A maleic acid pretreatment described by Lu et al. was used in order to avoid exposing the sample to alkali species, which themselves contribute to char formation [54]. In this procedure, 1.35 g of dry solids were combined with 22.5 mL 250 mM maleic acid in 1 in. diameter stainless steel tubing and heated to a temperature of 160°C at a rate of approximately 12.7°C/min, holding for 19 minutes. The tubing was then cooled to room temperature with water. Vacuum filtration was used to recover

the solid residue, reserving the liquid for HPLC analysis. The filtered solids were triple rinsed using deionized water, reserving the liquid from the first rinse for analysis. The solids were then dried at 45°C for 24 hours. Samples were then analyzed using the NREL Laboratory Analytical Procedure (LAP) (details in Appendix B), the results of which can be seen in Table 3. The xylan content of the maleic acid-pretreated sample was found to be 0, indicating complete removal of hemicellulose.

Table 3. NREL LAP Analysis of Poplar and Maleic Acid Pretreated Poplar

Material	% AIL*	% ASL[#]	% Lignin^{\$}	% Cellulose^{\$}	% Xylan^{\$}
Poplar w/o bark	18.35	6.02	24.37	46.09	19.3
Maleic Acid Pretreatment	21.26	1.95	23.21	66.2	0.0

*AIL: Acid Insoluble Lignin

[#]ASL: Acid Soluble Lignin

^{\$}Extractive free

Lignin-free samples consisted of carbohydrate-rich residues from work by Parsell et al., which demonstrated selective conversion of lignin in biomass while leaving the carbohydrate fraction (containing cellulose and hemicellulose) intact in a process they refer to as the catalytic depolymerization of lignin (CDL) [15,55,56].

2.2.3 Py-GC/MS Reactor

In order to study the products of fast pyrolysis of inorganic-doped cellobiose, the pyroprobe pulsed-flow reactor, previously described in Section 1.2.2, was used to vaporize solid samples. Samples of mass 0.3-0.4 mg were loaded into a quartz tube (ID 0.15 cm, length 2.5 cm), which was subsequently secured within a platinum coil and inserted into the pyroprobe. The sample was swept with nitrogen prior, then pyrolyzed by heating the platinum coil to 500°C with a temperature ramp of 1000°C/s, held for 10 s. Pyrolysis vapors were swept out of the chamber by 30 mL/min He (99.995%, Indiana Oxygen) into a downstream GC/MS for analysis. The quartz tube was massed before and after pyrolysis in order to determine the mass of residual carbon left as char following pyrolysis.

In order to study the role of hemicellulose in char formation, the pyroprobe pulse-reactor was again used, with a downstream hydrodeoxygenation catalyst (5% PtMo/MWCNTs, described

previously in Section 1.2.1). Samples were loaded into the quartz tube and pyrolyzed at 500°C, with resulting vapors swept into the downstream catalyst bed held at 300°C by a hydrogen flow (100 mL/min). The resulting products were analyzed using GC/MS, and carbon residues in the quartz tube were determined by massing the tube before and after pyrolysis.

2.3 Results and Discussion

2.3.1 Effects of Inorganic Dopants on Cellobiose Pyrolysis

The doped samples were pyrolyzed using the pyroprobe, and the resulting vapors were analyzed using GC/MS. A large number of products were detected, but the major products are shown in Figure 25. Minor products were grouped together by key structural features. Furans represent products containing a furan ring, light oxygenates represent $C_1 - C_4$ oxygenated compounds, and sugars represent cyclic C_{6+} products. A detailed breakdown of the selectivity to individual products is provided for 1% NaCl and 10% NaCl samples in Appendix C.

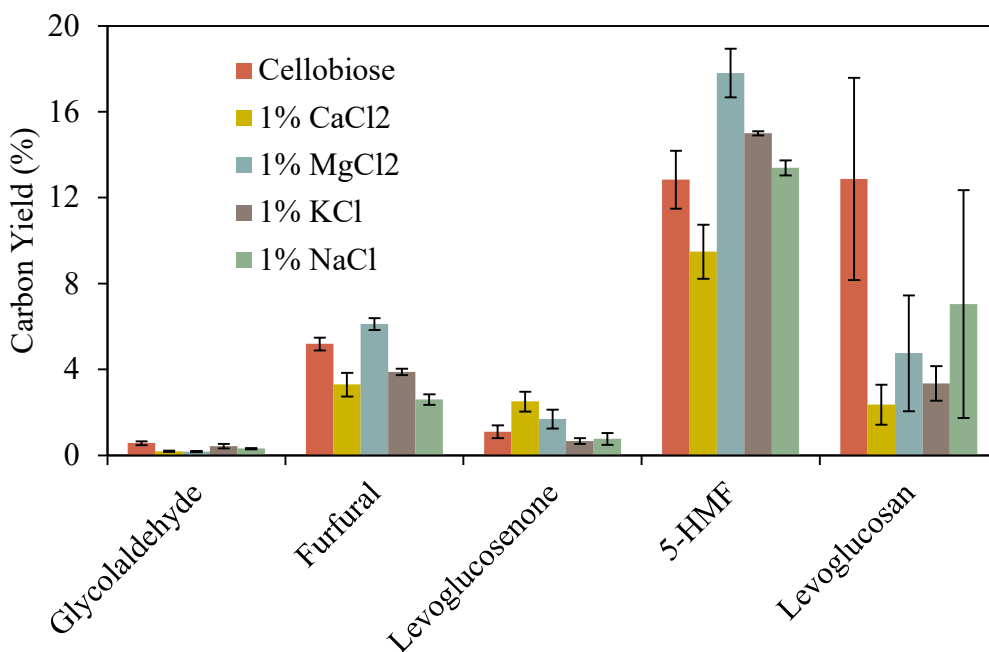


Figure 25. Product selectivity to major products following fast pyrolysis of cellobiose doped with CaCl₂, MgCl₂, KCl, and NaCl in 1 wt% solutions. Pyrolysis conducted at 500°C in 30 mL/min He.

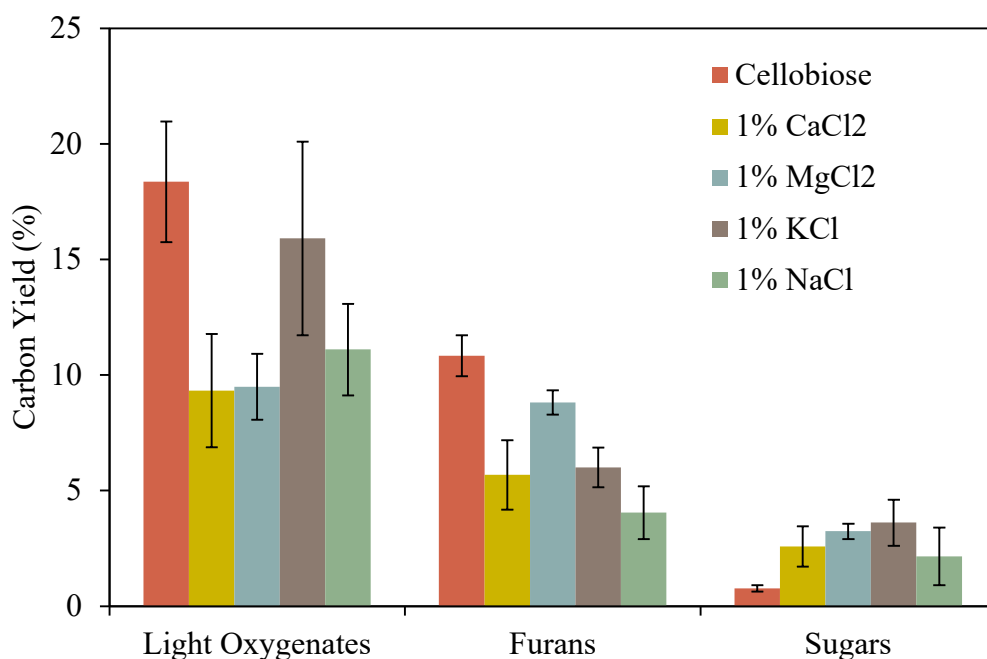


Figure 26. Product selectivity to products grouped by molecular structure following fast pyrolysis of cellobiose doped with CaCl₂, MgCl₂, KCl, and NaCl in 1 wt% solutions. Pyrolysis conducted at 500°C in 30 mL/min He.

As shown in Table 4, The incorporation of inorganic salts greatly increased char yields in cellobiose samples, consistent with previous literature reports. Quantification of the products following fast pyrolysis suggests that the presence of these inorganic compounds leads to an increase in selectivity to secondary pyrolysis products. The product selectivity to levoglucosan is greatly reduced in the presence of greatly reduced in all cases, suggesting involvement of levoglucosan in secondary reactions which lead to char formation. This is consistent with previous reports on the effect of an acid wash to remove metals from cellulose on char formation and secondary reactions of levoglucosan [57]. Product selectivities to products containing furan rings remained approximately unchanged at low concentrations of the inorganic dopant. These products primarily consist of 5-hydroxymethylfurfural and furfural, but also encompasses several other compounds containing furan rings but present in very low selectivity; they are thought to be secondary pyrolysis products, likely resulting from dehydration of the primary pyrolysis product levoglucosan to form 5-hydroxymethylfurfural. This reaction may take place in the pyrolysis melt phase, the liquid layer which exists at the surface of the solid biomass particle. This would suggest

that inorganic dopants act within this melt phase to catalyze dehydration reactions which degrade levoglucosan. At higher concentrations of the inorganic dopant, levoglucosan is undetectable among the products, and selectivity to furan-containing products also began to decrease. This is consistent with an increased dehydration rate that can be attributed to the increased concentration of inorganic dopants; concentrations of 5-HMF-derived products, such as furfural, remains significant even as selectivity to 5-HMF decreased.

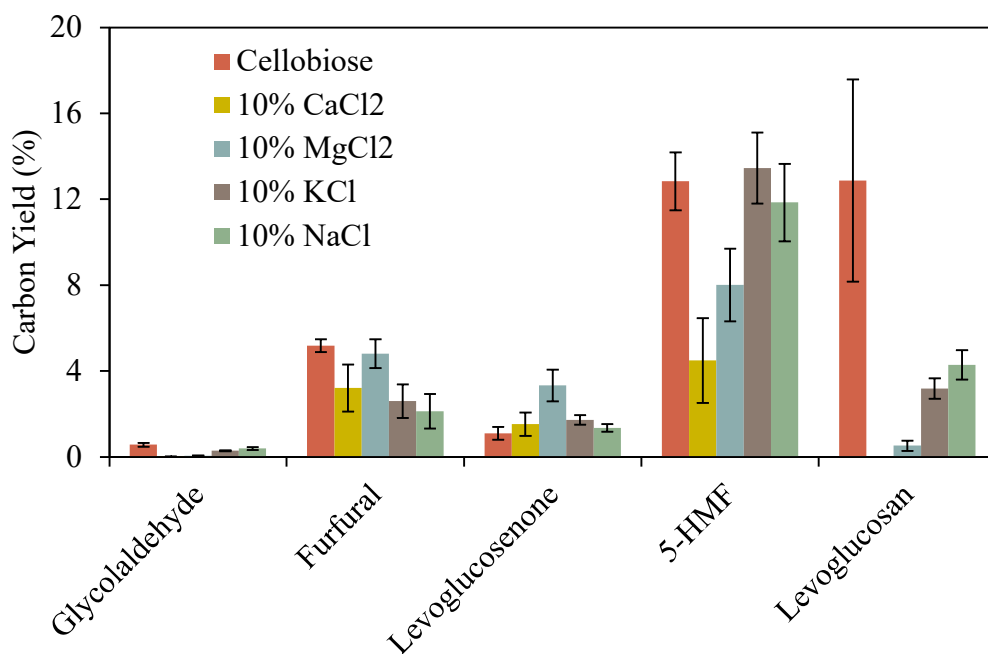


Figure 27. Product selectivity to major products following fast pyrolysis of cellobiose doped with CaCl₂, MgCl₂, KCl, and NaCl in 10 wt% solutions. Pyrolysis conducted at 500°C in 30 mL/min He.

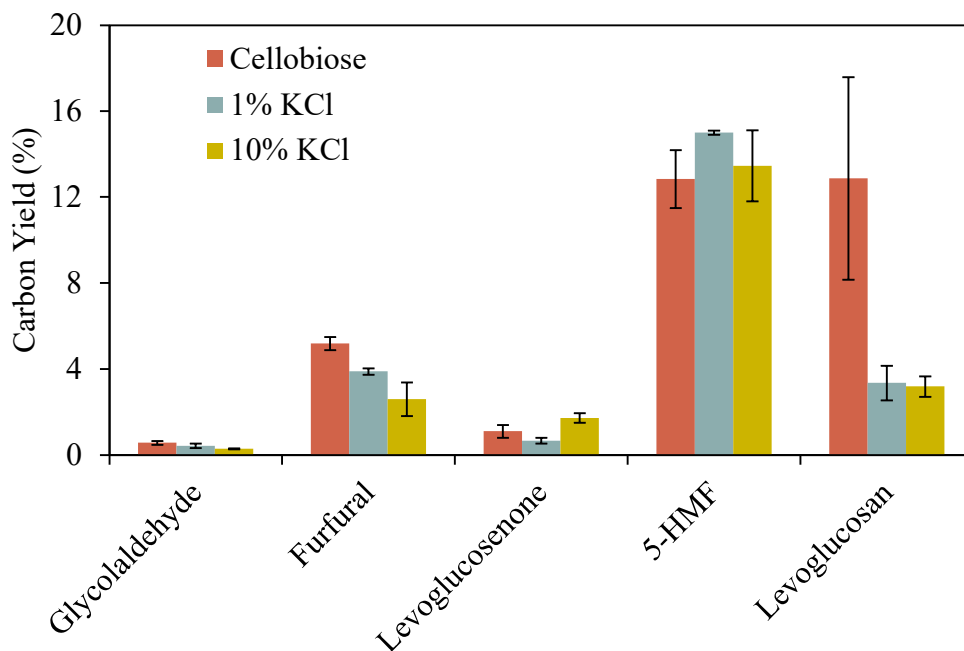


Figure 28. Effects of concentration of monovalent cation K^+ on product selectivities to major fast pyrolysis products of cellobiose. Pyrolysis conducted at 500°C in 30 mL/min He.

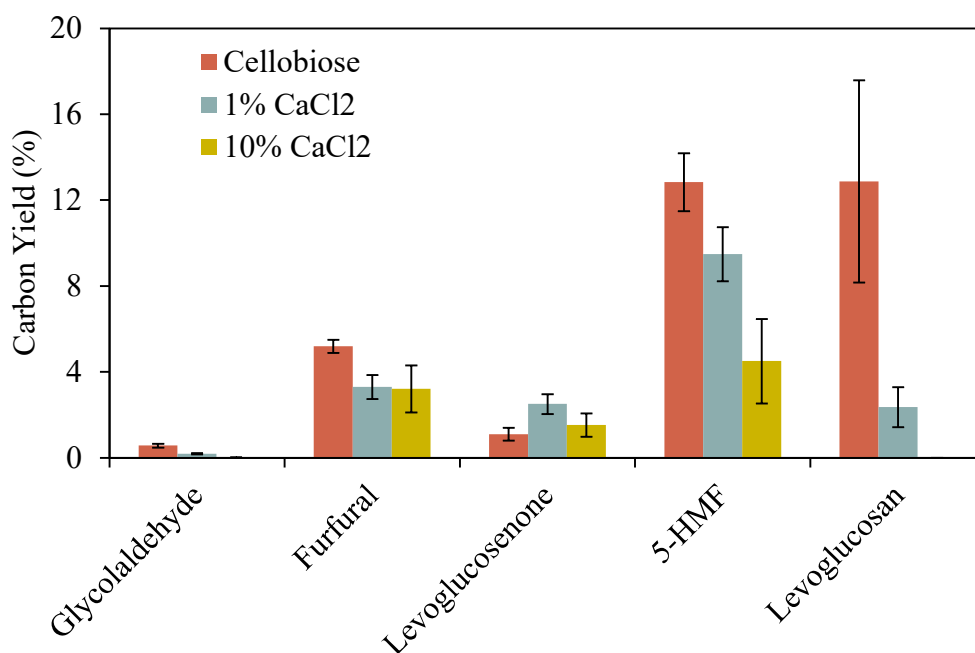


Figure 29. Effects of concentration of divalent cation Ca^{2+} on product selectivities to major fast pyrolysis products of cellobiose. Pyrolysis conducted at 500°C in 30 mL/min He.

Table 4. Carbon selectivity to char for cellobiose doped with 1% or 10% of various inorganic salts

Material	Char Carbon Yield (10%)	Char Carbon Yield (1%)
Cellobiose	33.0 ± 4.9 % ^a	33.0 ± 4.9 % ^a
Cellobiose – CaCl ₂	89.6 ± 5.1 %	78.5 ± 19.4 %
Cellobiose – MgCl ₂	55.9 ± 16.7 %	70.4 ± 9.9 %
Cellobiose – KCl	50.7 ± 11.4 %	65.1 ± 10.3 %
Cellobiose – NaCl	61.4 ± 23.9 %	82.3 ± 20.4 %

^aThe char carbon yield of undoped cellobiose is provided for reference

2.3.2 Contribution of Hemicellulose to Char Formation

The contributions of various components of biomass were investigated by conducting fast pyrolysis of cellulose, the CDL residue, and the maleic acid-pretreated sample. Since the purpose of these experiments was to focus on char yields, hydrodeoxygenation was used to simplify the product distribution by eliminating oxygen functionalities. This was expected to increase the overall carbon balance relative to pyrolysis without hydrodeoxygenation, as the slate of hydrocarbons formed by hydrodeoxygenation can be readily separated and identified via GC/MS, whereas the pyrolysis products themselves may contain unidentifiable species, or a product distribution containing many species with overlapping peaks. The previously mentioned PtMo/MWCNTs catalyst was used for hydrodeoxygenation. The resulting product distributions are shown in Figure 30. From this data, it is seen that cellulose char yields are much lower than char yields for intact poplar, delignified poplar, and the maleic acid-pretreated poplar. Very low yields of C₇₊ products were observed for cellulose; this is expected, since fast pyrolysis is expected to cleave the C-O linkages between C₆ monomeric species in cellulose; higher molecular weight species are expected to derive primarily from the lignin fraction. Poplar, delignified poplar, and the maleic acid pretreated poplar all had significant char yields; of these, the char yield for delignified sample had the lowest char yield. This is consistent with lignin as a major char contributor. However, char in this sample is much higher than for cellulose, indicating that lignin alone is not responsible for char formation. The maleic acid pretreated sample showed a decrease in char yield relative to intact poplar, indicating that hemicellulose does play a role in char

formation. Taken together, these results suggest that hemicellulose contributes more to char formation than cellulose, but less than lignin.

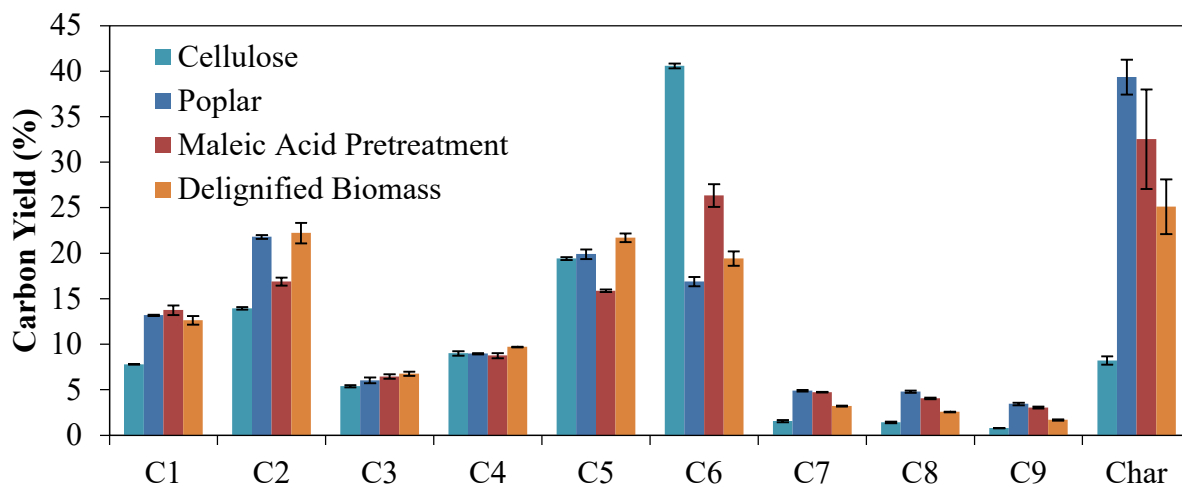


Figure 30. Product distribution following hydrodeoxygenation of fast pyrolysis vapors from cellulose, poplar, hemicellulose-lean residues, and delignified poplar. Pyrolysis was carried out at 500°C in 100 mL/min H₂ at 300 psi, with hydrodeoxygenation taking place over 5% PtMo/MWCNTs at 300°C

Table 5. Char yields and carbon balances following fast pyrolysis and hydrodeoxygenation of poplar, cellulose, delignified poplar, and maleic acid pretreated poplar.

Feed	Char (Carbon %)	Carbon balance (%)
Poplar Wild Type	38 ± 2	88 ± 4
Delignified Biomass	25 ± 4	83 ± 6
Maleic Acid Pretreatment	33 ± 4	83 ± 4
Cellulose	8 ± 0.3	95 ± 2

2.4 Conclusions

From this work, it can be seen that the presence of inorganic species leads to increased char formation. This is caused by degradation of levoglucosan, indicative of greatly increased

secondary reactions and suggesting that alkali species catalyze dehydration. These results could be used to quantitatively validate mechanistic studies using mass spectroscopy which are similar to previous work to understand cellulose pyrolysis mechanisms.

Although lignin was confirmed as the component of lignocellulosic biomass which contributes most significantly to char formation, hemicellulose was identified as a significant contributor. It might then be suggested that overall carbon losses to char from fast pyrolysis could be reduced, but not eliminated, by first extracting lignin from biomass via CDL, then subjecting the carbohydrate residue to hydrodeoxygenation for the formation of liquid fuels. This would have the advantage of preserving the aromatic structure of lignin for transformation into chemicals.

3. EFFECTS OF ETHENE PRESSURE ON THE DEACTIVATION OF NI-ZEOLITES DURING ETHENE OLIGOMERIZATION AT SUB-AMBIENT TEMPERATURES

3.1 Introduction

Alkene oligomerization is a key intermediate reaction in routes that upgrade light alkanes (C₁-C₄), which can be sourced from shale gas, into transportation fuel-range molecules.[58] Ni-exchanged zeolites and Brønsted-acidic zeolites are both commonly studied for alkene oligomerization, but Ni-exchanged zeolites can more efficiently catalyze ethene oligomerization at lower temperatures and more selectively form linear alkene products (e.g., 1-butene).[59–64] In both Ni-exchanged zeolites and Brønsted-acidic zeolites, deactivation is observed under typical reaction conditions for ethene oligomerization (393-573 K, 1-35 bar), with various mechanistic explanations proposed in the literature. Single-site deactivation mechanisms are typically ascribed to the formation of heavier alkene oligomers that remain strongly adsorbed at Ni active sites.[61,65] Dual-site deactivation mechanisms are proposed to reflect the formation of a bridging alkyl species between adjacent Ni sites, as supported by experimental evidence from Mlinar et al. for deactivation rates in Ni-Na-X zeolites that followed a hyperbolic function with time and were second-order in Ni site density,[66] and DFT evidence from Saxena et al. indicating that ethene dimerization barriers at alkyl-bridged Ni sites are much higher than at isolated Ni sites.[67]

Alkene oligomerization carried out under near-supercritical conditions has been proposed to attenuate deactivation via the solvation of carbonaceous species that serve as coke precursors[68–72], reminiscent of regeneration treatments using supercritical alkane phases to remove coke from zeolite catalysts during hydrocarbon processing.[73–77] Mitigated deactivation was reported during ethene oligomerization on Ni-H-Beta and Ni-Al-SBA-15 under supercritical conditions by Jan et al.,[70] and during heavier alkene (e.g., 1-butene, 1-hexene) oligomerization on H-FER, H-MFI, and H-FAU under near-supercritical conditions.[69,71] The use of high pressures and low temperatures can also lead to capillary condensation of reactant alkenes within mesoporous voids, at temperatures and reduced pressures that can be predicted by the Kelvin equation.[78,79] Agirrezabal-Telleria and Iglesia investigated ethene oligomerization over mesoporous Ni-MCM-41 at temperatures as low as 243 K and ethene pressures up to 15 bar; although deactivation is rapid at 448 K, it becomes negligible at sub-ambient temperatures and sufficiently high ethene

pressures that lead to an intrapore condensed ethene phase, proposed to promote oligomer desorption over formation of deactivating species.[78,79] The use of reaction conditions that would nominally cause alkene capillary condensation within microporous voids (<2 nm in diameter) that confine Ni and H⁺ active sites has not been fully explored as a potential strategy to confer stability during alkene oligomerization, and it remains unclear whether bulk-like liquid phases can be stabilized within the spatial constraints of zeolitic micropores.

3.2 Materials and Methods

Ni-MCM-41, Ni-Beta, and several samples of Ni-FAU were synthesized. Ni-MCM-41 (Si/Al = 18, Ni/Al = 0.24) was prepared starting from a commercial sample of Al-MCM-41 (Sigma Aldrich, 643650, lot MKCC8589). Ni-Beta (Si/Al = 12.5, Ni/Al = 0.28) was prepared starting from a commercial sample of NH₄-Beta (Zeolyst International, CP814E, lot number 2493-65). Ni-FAU (Si/Al = 6, Ni/Al = 0.07) was prepared starting from a commercial sample of NH₄-Y (Zeolyst International, CBV712, lot number 712014001708), while Ni-FAU (Si/Al = 40, Ni/Al = 0.20) and Ni-Li-FAU (Si/Al = 40, Ni/Al = 0.26) were prepared starting from a commercial sample of NH₄-Y (Zeolyst International, CBV780, lot number 78004N00C548).

Ni-Beta was prepared by first converting NH₄-Beta into H-Beta via oxidative treatment under flowing dry air (100 cm³ s⁻¹ g_{cat}⁻¹, 99.999% UHP, Indiana Oxygen) at 773 K for 4 h. The dried sample was then subjected to Ni ion exchange using 100 mL g_{cat}⁻¹ of 0.3 M Ni(NO₃)₂ (Sigma Aldrich, 99.999%) at 348 K for 16 h. Following exchange, solids were removed via centrifugation and washed with Millipore water (18.2 MΩ cm). The catalyst was then treated again in dry air (100 cm³ s⁻¹ g_{cat}⁻¹, 99.999% UHP, Indiana Oxygen) at 773 K for 4 h. Ni-MCM-41, Ni-FAU-6, and Ni-FAU-40 were prepared using nearly identical procedures, differing only in the exchange solutions used. Ni-MCM-41 was prepared using an exchange solution of 50 mL g_{cat}⁻¹ of 0.075 M Ni(NO₃)₂; Ni-FAU-6 was prepared using 100 mL g_{cat}⁻¹ 0.025 M Ni(NO₃)₂; and Ni-FAU-40 was prepared using 100 mL g_{cat}⁻¹ 0.010 M Ni(NO₃)₂. Preparation of Ni-Li-Y was synthesized using the same starting material and oxidative treatment as Ni-FAU-40, but the first exchange step was a Li cation exchange of Ni-Y using 100 mL g_{cat}⁻¹ of 0.84 M LiNO₃. The exchange was carried out for 24 h, with periodic adjustment of the solution pH to 7 by adding a solution of 0.1 M LiOH. Following exchange, solids were separated out via centrifuge and washed. The resulting Li-Y was treated at 773 K for 4 h in flowing dry air (100 cm³ s⁻¹ cat⁻¹). Li-Y was then subjected to Ni and Li

co-cation exchange, using 100 mL $\text{g}_{\text{cat}}^{-1}$ of 0.04 M $\text{Ni}(\text{NO}_3)_2$ and 0.84 M LiNO_3 for 24 h. The pH was again periodically adjusted to 7 by adding a solution of 0.1 M LiOH . Solids were separated by centrifugation, washed, dried, and heated in dry air ($100 \text{ cm}^3 \text{ s}^{-1} \text{ g}_{\text{cat}}^{-1}$) at 773 K for 4 h. Following synthesis, Si, Al, Ni, and Li contents were quantified by inductive coupled plasma-optical emission spectrometry (ICP-OES) using a Thermo Scientific iCAP 7000 Plus Series spectrometer. Pore diameter distributions for Ni-MCM-41, Ni-Beta, Ni-FAU-6, and Ni-Li-FAU-40 were obtained from Ar adsorption isotherms (87 K) using a Micromeritics 3Flex Adsorption Analyzer.

Ethene oligomerization catalytic experiments were carried out in a plug-flow reactor at 243 K and 258 K. Sub-ambient temperatures were achieved by cooling by liquid nitrogen flow through a copper heat exchanging coil wrapped around a 316 stainless steel reactor and controlled by a switching valve. Experiments were conducted over a range of ethene partial pressures ranging from 1 to 24 bar. Helium (99.999%, Indiana Oxygen) was used as an inert in the system during experiments conducted at 1 bar. 500 sccm ethene (99.95%, Matheson) was passed through a fixed catalyst bed during reactions at ethene partial pressures above 1 bar. For experiments conducted at 1 bar ethene partial pressure, 500 sccm total flow was used, with 74 sccm ethene and 426 sccm helium. 5 sccm methane (99.995%, Matheson) was co-fed as an internal standard for gas chromatography (GC) analysis. A small ethane impurity in the ethene cylinder was detected, and was used as an internal standard following quantification with methane and confirming that alkene hydrogenation did not occur on the catalyst. Oligomerization products were analyzed using an Agilent Technologies 6890N Gas Chromatograph using a flame ionization detector. Prior to flow experiments, catalysts were pretreated in flowing dry air, heating at a rate of 2 K min^{-1} up to 773 K and holding for 3 h before decreasing the temperature to the reaction temperature. In the case of Ni-FAU, a significant activation period was seen. The following H_2 pretreatment (99.995%, Praxair) was performed with these samples in order to eliminate the activation period: following heating in air to 773 K at a rate of 2 K min^{-1} and holding for 3 h, the sample was cooled to 453 K and exposed to 1% H_2/He for 8 h before cooling to reaction temperature of 258 K. 5 sccm hydrogen was co-fed over the course of experiments with Ni-FAU at 1% concentration in the feed stream. Reaction conditions were otherwise identical to those described previously.

The transient decay in ethene oligomerization STY was modeled using the generalized deactivation rate equation derived by Butt and Peterson, where k_d is the apparent deactivation

constant, r is the ethene oligomerization rate at a given time t , r_0 is the initial rate at time 0, and n is the deactivation order.[67,80]

$$r = \frac{r_0}{(1+(n-1)k_d r_0^{n-1} t)^{\frac{1}{n-1}}} \quad (3.1)$$

A Python code previously developed and used by Saxena et al. was used to fit the experimental data in Figure 31 to Eq. (3.1) in order to estimate the best-fit deactivation parameters (additional details in Appendix G), which are reported for each catalyst and condition in Table 6.

3.3 Results and Discussion

The overarching goal of this work is to investigate how varying the ethene pressure (1–24 bar) at sub-ambient temperatures (243–258 K) influences the kinetics of deactivation during ethene oligomerization on Ni-exchanged microporous and mesoporous materials. Ni-MCM-41 (Si/Al = 18, Ni/Al = 0.24), Ni-Beta (Si/Al = 12.5, Ni/Al = 0.28), Ni-FAU (Si/Al = 6, Ni/Al = 0.07, labeled hereafter Ni-FAU-6), and Ni-FAU (Si/Al = 40, Ni/Al = 0.20, labeled hereafter Ni-FAU-40) were synthesized. Ethene oligomerization rates were measured at 243 K and 7-17 bar C₂H₄ for mesoporous Ni-MCM-41, and at 258 K and 1-24 bar C₂H₄ for microporous Ni-Beta and Ni-FAU, shown in Figure 31 for each sample at various ethene reduced pressures (P/P_0), where P_0 is the ethene saturation pressure ($P_0 = 19.3$ bar at 243 K; $P_0 = 28.6$ bar at 258 K). Butene was the sole detectable product in experiments involving Ni-Beta under the conditions studied. Minor amounts of hexene isomers were formed over Ni-FAU-6 (<1% selectivity) and Ni-FAU-40 (<3% selectivity), and Ni-MCM-41 (<5% selectivity). Minor amounts of octene isomers (<0.5% selectivity) were also detected for Ni-MCM-41 at the highest pressure studied. Rate data are calculated as the total formation rates of all product alkene oligomers, normalized to total Ni content, and expressed in terms of the equivalent ethene consumption rate. Ethene oligomerization rates were also measured on Ni-Li-FAU and on the proton-form of Al-MCM-41 as control experiments in order to confirm that Brønsted acid sites did not significantly influence the deactivation behavior observed under these conditions (additional details in Appendix F).

The kinetic behavior measured on Ni-MCM-41 is consistent with previous reports, as ethene oligomerization rates (0.90 mol ethene (mol Ni)⁻¹ s⁻¹ at 243 K and 17 bar ($P/P_0 = 0.89$), Table 6) are similar (within 4x) to that reported by Agirrezabal-Telleria et al. (0.22 mol ethene (mol Ni)⁻¹

s⁻¹ at 243 K and 15 bar) [78]. Ethene oligomerization rates on Ni-MCM-41 remained stable (varied by <4% over 4 h time-on-stream) at ethene $P/P_0 > 0.71$ (Figure 31a), consistent with the report of Agirrezabal-Telleria et al. that rates on Ni-MCM-41 were stable at $P/P_0 > 0.6$ [78]. Ethene oligomerization rates showed evidence of deactivation at $P/P_0 = 0.36$, with a deactivation order of approximately two (1.9 ± 0.3 ; Table 6). Agirrezabal-Telleria et al. modeled deactivation in MCM-41 using a first-order expression for conditions of $P/P_0 > 0.45$ [78]; our attempts to model the rate data reported in that work at 243 K and 9 bar (corresponding to $P/P_0 = 0.48$) to the generalized deactivation model by Butt and Peterson (Eq. (3.1)) resulted in fitting a deactivation order of 2.0 ± 0.8 (additional details in Appendix G), indicating consistency (within the model fitting uncertainty) between the Ni-MCM-41 data reported here and in prior work, and suggesting that a multi-site deactivation mechanism may prevail for Ni-MCM-41 at conditions that approach capillary condensation.

Ethene oligomerization rates (per Ni) in Ni-Beta (Figure 31b) were considerably lower than in Ni-MCM-41 (Figure 31a), with initial rates (258 K, 23.8 bar) that were two orders-of-magnitude lower than measured on Ni-MCM-41 at lower temperature and pressure (243 K, 17 bar; Table 6). Deactivation was observed on Ni-Beta zeolites at all ethene reduced pressures studied, including at values that are nominally above the point of capillary condensation according to the Kelvin equation ($P/P_0 > 0.51$, details in Appendix E). Deactivation was not attenuated with increasing ethene pressure, and was found to be approximately second-order in Ni site density in Ni-Beta for all pressures studied. This observation of second-order deactivation kinetics in Ni-Beta with high active Ni site density ($\text{Si/Al} = 11$, $\text{Ni/Al} = 0.28$, average Ni-Ni distance = 0.8 nm) was also reported by Saxena et al. on Ni-Beta samples of similar Ni site density ($\text{Si/Al} = 11$, $\text{Ni/Al} = 0.25$, average Ni-Ni distance = 1 nm), albeit for rates measured at higher temperatures (453 K) and lower ethene pressures (0.1-1.0 kPa C₂H₄).[67]

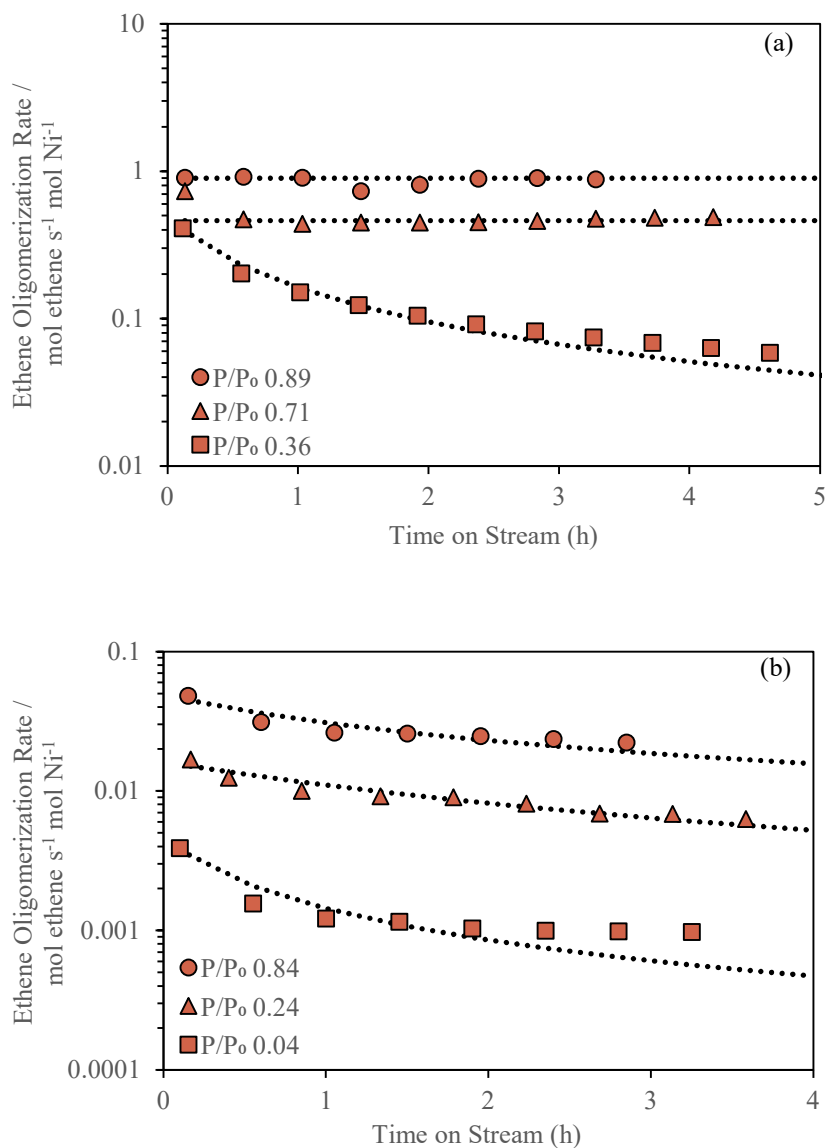
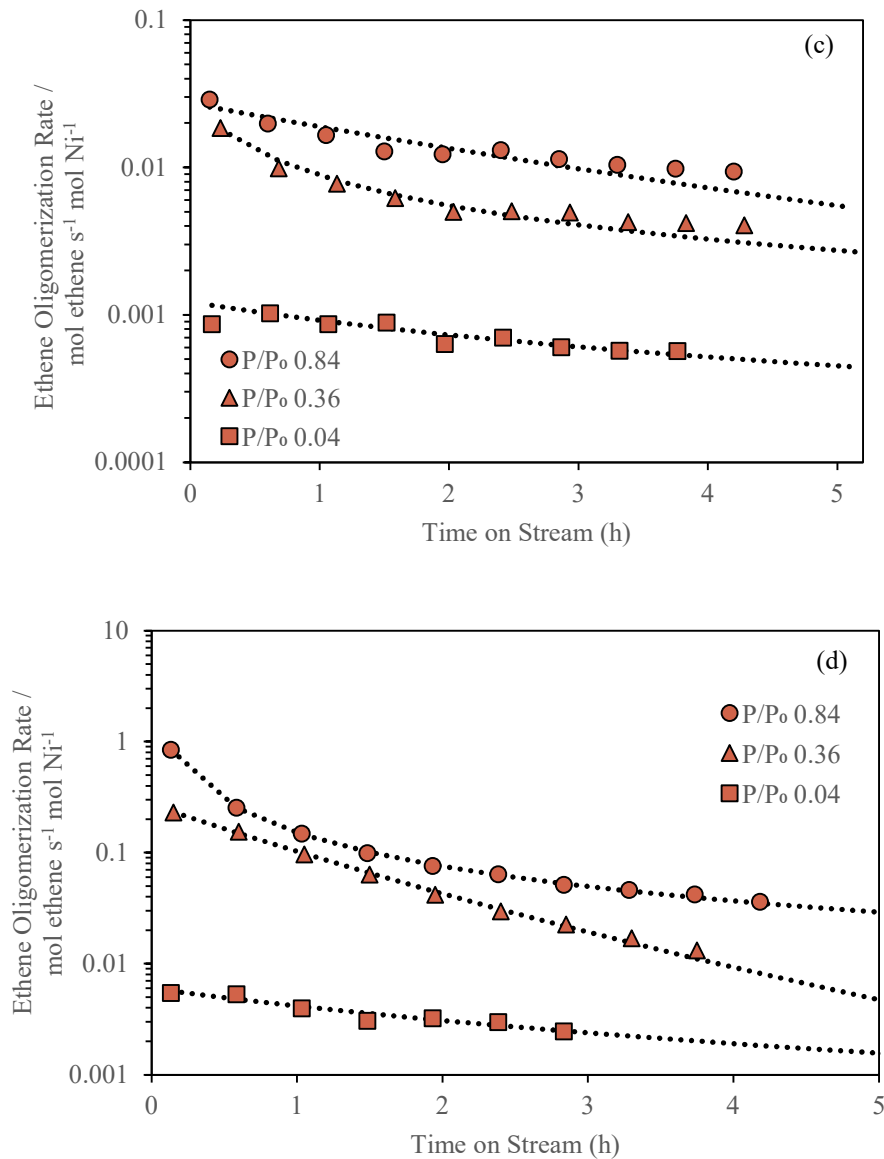


Figure 31. Ethene oligomerization rates as a function of time-on-stream collected for (a) Ni-MCM-41 (Si/Al = 18, Ni/Al = 0.24) at 243 K, (b) Ni-Beta (Si/Al = 12.5, Ni/Al = 0.28) at 258 K, (c) Ni-FAU-6 (Si/Al = 6, Ni/Al = 0.07) at 258 K, and (d) Ni-FAU-40 (Si/Al = 40, Ni/Al = 0.20) at 258 K. A H₂ co-feed was present in Ni-FAU experiments as 1% of total flow. Dotted lines represent fits to deactivation models according to a generalized deactivation model (Eq. (3.1)), with best-fit parameters summarized in Table 6.

Figure 31 continued



Ethene oligomerization rates (per Ni) in Ni-FAU-6 were lower (Figure 31c) than in Ni-Beta (Figure 31b), and deactivation was observed at all pressures studied as in the case of Ni-Beta, including at values that are nominally above the point of capillary condensation ($P/P_0 > 0.54$; Appendix E). Deactivation in Ni-FAU-6 was also found to be approximately second-order in Ni site density at all pressures studied (Table 6) for this composition of material ($Si/Al = 6$, $Ni/Al = 0.07$), suggesting a deactivation mechanism involving two Ni sites, likely via the formation of a bridging alkyl species between adjacent Ni sites as proposed by Mlinar et. al. for Ni-Na-X (Si/Al

= 1.3 , Ni/Al = 0.28)[66] and Saxena et. al. for Ni-Li-Beta at high Ni site densities (Si/Al = 11, Ni/Al = 0.25)[67].

Table 6. Deactivation constants (k_d) and orders (n), and initial ethene dimerization rates (r_0) for Ni-MCM-41, Ni-Beta, Ni-FAU-6, and Ni-FAU-40 measured at different ethene reduced pressures (P/P_0). Statistical estimates of goodness-of-fit and uncertainties are reported in Table 12 (Appendix G).

Sample	P/P_0	k_d^a	r_0 (mol ethene s^{-1} mol Ni^{-1})	n
Ni-MCM-41	0.36	3.15	0.493	1.9
Ni-MCM-41	0.71	0	0.463	0
Ni-MCM-41	0.89	0	0.899	0
Ni-Beta	0.04	6.07×10^{-4}	4.59×10^{-3}	2 ^b
Ni-Beta	0.24	8.49×10^{-3}	1.62×10^{-2}	1.8
Ni-Beta	0.84	3.90×10^{-2}	4.90×10^{-2}	2.2
Ni-FAU-6	0.04	3.04×10^2	1.23×10^{-3}	2.0
Ni-FAU-6	0.36	2.13×10^3	2.82×10^{-2}	2.2
Ni-FAU-6	0.84	1.52×10^{-3}	2.72×10^{-2}	1.2
Ni-FAU-40	0.04	0.741	6.00×10^{-3}	1.6
Ni-FAU-40	0.36	9.98×10^{-4}	0.271	1.1
Ni-FAU-40	0.84	16.1	2.37	1.9

^aUnits for k_d : mol Ni^{n-1} (mol ethene)¹⁻ⁿ s^{-n-2} .

^bFitting data to Eq.(3.1) was not possible within specified limits ($n < 2.3$, standard error < 0.05); thus, data were fit to power-law deactivation models with either $n = 1$ or $n = 2$ and the value reported corresponds to the best-fit determined by R^2 values (additional details in Appendix G)

To study the effect of Ni site density on the prevalent deactivation order and mechanism, Ni-FAU-40 was prepared with lower Ni density (0.3 wt% Ni, average Ni-Ni distance = 2.6 nm for Ni-FAU-40 as compared to 0.7 wt% Ni, average Ni-Ni distance = 1.3 nm for Ni-FAU-6). Ethene oligomerization rates on Ni-FAU-6 and Ni-FAU-40 are shown in Figure 31c and Figure 31d, with accompanying deactivation constants and orders reported in Table 6. Rates on Ni-FAU-40 are significantly higher (by up to 100x at $P/P_0 = 0.84$, Table 6) than observed on Ni-FAU-6, which may reflect the presence of larger mesoporous voids in Ni-FAU-40 (3.5-10 nm diam.; Appendix E) than the microporous voids in Ni-FAU-6 (1.4-1.7 nm diam.; Appendix E).[81] Deactivation kinetics in Ni-FAU-40 were first-order at $P/P_0 = 0.36$ ($n = 1.1 \pm 0.1$) and at $P/P_0 = 0.04$ ($n = 1.6 \pm$

1.3), suggesting deactivation by the formation of heavier oligomers adsorbed at Ni sites according to a single-site mechanism. Differences in deactivation order between Ni-FAU-40 ($n \sim 1$) and Ni-FAU-6 ($n \sim 2$) at the same P/P_0 (0.04-0.36) suggest that Ni sites in Ni-FAU-40 are sufficiently isolated so as to prevent the formation of bridging alkene species, which are proposed as the primary cause of deactivation in Ni-FAU-6. However, second-order deactivation was observed in Ni-FAU-40 at $P/P_0 = 0.84$ ($n = 1.9 \pm 0.02$), suggesting a dual-site deactivation mechanism that involves two Ni sites. A transition from a single-site deactivation mechanism to a dual-site deactivation mechanism suggests that higher ethene pressures result in higher densities of Ni sites formed *in situ* at initial reaction times, as evidenced from the higher initial rate values (Table 6). Additionally, second-order deactivation kinetics may be facilitated by the mobilization of Ni active sites at high ethene pressures, given DFT calculations by Brogaard et al. on Ni-SSZ-24 indicating that active sites for ethene oligomerization may also include mobile Ni ions coordinated with two ethene molecules,[82] motivating future theoretical work to evaluate this hypothesis using DFT-derived phase diagrams of ethene coverages on Ni(II) sites in zeolites as a function of temperature and ethene pressure.

A similar transition from first- to second-order deactivation kinetics was also reported by Saxena et al. in Ni-Beta zeolites of low Ni site density ($\text{Si}/\text{Al} = 11$, $\text{Ni}/\text{Al} = 0.06$, average Ni-Ni distance = 4 nm) with increasing co-fed H_2 pressure, which was proposed to occur because of the *in situ* generation of a larger number of Ni(II)-hydride that rapidly transform to active Ni(II)-ethyl reactive intermediates, resulting in an increase in the active Ni site density at initial reaction times.[67] In the current study, H_2 was co-fed during experiments with Ni-FAU in order to eliminate the observed activation period, and the presence of H_2 in combination with high C_2H_4 pressures generated a larger number of active Ni(II)-ethyl sites so as to result in an increase in initial active Ni site density at these conditions. This activation period may be the result of Ni migration from hexagonal prisms and sodalite cages in FAU into supercages, which has been shown to be mediated by coordinating ligands such as water and propene [66], and which might also be mediated by hydrogen. Activation transients were not observed in Ni-Beta because this framework does not contain hexagonal prisms and thus Ni^{2+} cations within the 12-membered ring (12-MR) are accessible to ethene, and because the high ethene reactant pressures used in this study led to an attenuation of the activation transient caused by ethene-assisted formation of Ni(II)-hydride species, consistent with previous work [59]. We find that in the absence of co-fed H_2 ,

deactivation in Ni-FAU-40 is first-order ($n = 1.3 \pm 1.2$) in Ni site density at $P/P_0 = 0.04$ and second-order ($n = 1.8 \pm 0.2$) in Ni site density at $P/P_0 = 0.84$, as shown in Figure 32. Following an activation period (1 h), rates between the experiments with and without co-fed H_2 are similar (within 1.15x), and deactivation parameters are nearly identical as shown in Table 7. This suggests that co-fed H_2 does not significantly influence the deactivation kinetics of Ni-FAU-40, suggesting that increasing ethene pressure is the predominant cause of the transition in deactivation order and implying that Ni solvation and mobilization by alkene reactants might be a more plausible explanation for the observed transition in deactivation order.

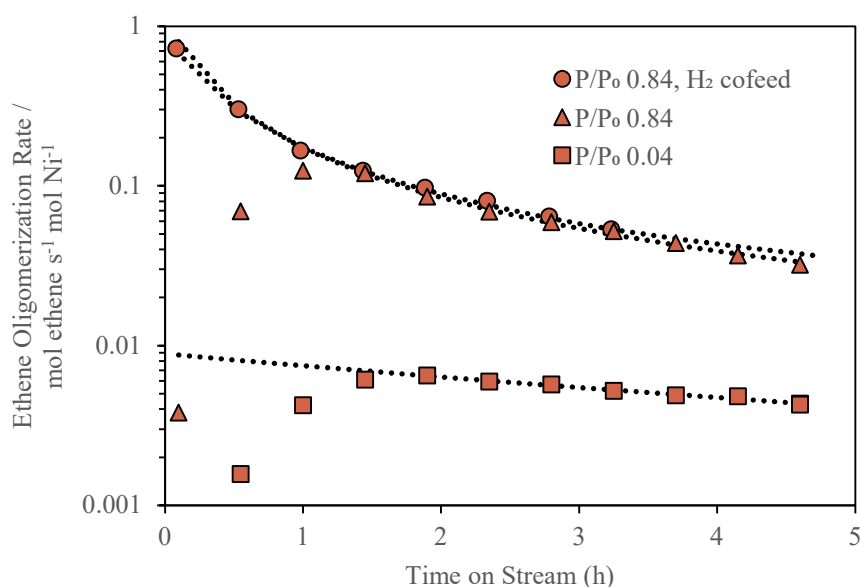


Figure 32. Ethene oligomerization rates as a function of time-on-stream at 258 K for Ni-FAU-40 (Si/Al = 40, Ni/Al = 0.20) at conditions with and without 1% H_2 co-feed. Dashed lines represent fits to deactivation models according to a generalized deactivation model (Eq. (3.1)), with parameters calculated in Table 7.

The stabilization of mesoporous Ni-MCM-41 materials at high ethene pressures that lead to capillary condensation is unique among the porous materials tested here, suggesting that the spatial constraints imposed by microporous voids (<2 nm in diameter) may prevent the formation of liquid-like ethene phases that are effective at solvating and desorbing bound intermediates that are precursors to deactivating compounds. At capillary condensation conditions within mesoporous voids, a sufficiently high degree of coordination among confined ethene molecules causes formation of liquid-like phases, which result concomitantly in effective van der Waals interactions

between multiple intrapore ethene molecules and bound surface species that solvate them and lower their desorption barriers.[79] By contrast, the severe spatial constraints within microporous voids restrict the degree of coordination among confined ethene molecules, which is reflected in the inability of the Kelvin equation to accurately describe intrapore condensation in pores sufficiently small (<3.6 nm diameter) that cause adsorbed multilayers to interact with the pore surface despite the thickness of the condensed fluid layer, preventing the formation of a stable intrapore condensed phase.[83] Loosely confined ethene molecules within microporous voids are also less effective at solvating bound surface species and thus facilitating their desorption, suggesting that operation even at high ethene pressures is unable to mitigate deactivation in microporous materials. The deactivation observed at capillary condensation conditions in Ni-FAU-40, which contains significant fractions of mesoporous regions, further suggest that active Ni species are contained predominantly within the microporous rather than the mesoporous voids of this sample.

Table 7. Deactivation constants (k_d) and orders (n), and initial ethene dimerization rates (r_0) for Ni-FAU-40 at different ethene reduced pressures (P/P_0) with and without H_2 co-feed and pretreatment. Statistical estimates of goodness-of-fit and uncertainties are reported in Table 12 (SI).

H₂ Pressure (bar)	P/P₀	k_d	r₀ (mol ethene s⁻¹ mol Ni⁻¹)	n
0	0.04	1.06 x 10 ⁻²	8.95 x 10 ⁻³	1.4
0	0.84	3.93	1.20	1.8
0.24	0.84	3.94	0.963	1.8

^aUnits for k_d : mol Niⁿ⁻¹ (mol ethene)¹⁻ⁿ sⁿ⁻².

3.4 Conclusions

In summary, the deactivation of Ni-exchanged microporous and mesoporous materials during ethene oligomerization proceeds by different mechanisms, and the dominant deactivation mechanism depends strongly on both reaction conditions and catalyst material properties. As shown previously by Agirrezabal-Telleria and Iglesia[78,79] and reproduced here, the deactivation of mesoporous Ni-MCM-41 can be suppressed by operation at low temperatures and high ethene

pressures that lead to capillary condensation of liquid-like ethene within mesoporous voids, which has been proposed to solvate heavier hydrocarbons that cause deactivation and facilitate their transport to external fluid phases.[78,79] By contrast, operation under temperature and pressure conditions that should nominally cause capillary condensation within micropores does not attenuate the deactivation in Ni-exchanged zeolites (Ni-Beta, Ni-FAU) in an analogous manner, which appears to reflect the inability of ethene to form liquid-like structures within the spatial constraints of microporous voids. Second-order deactivation kinetics are observed on high Ni-site density zeolite samples, while deactivation orders transition from first- to second-order with increasing ethene pressure on low Ni-site density zeolite samples, indicating that both ethene pressure and Ni site density influence the prevalent deactivation mechanisms in Ni-zeolites. An intrapore condensed ethene phase appears to be capable of solvating the molecular species that serve as precursors to deactivation in both the first- or second-order deactivation regimes, but only larger mesoporous voids appear capable of condensing such a structured liquid-like phase.

APPENDIX A. QUANTIFICATION OF PYROLYSIS PRODUCTS USING FID AND EFFECTIVE CARBON NUMBER ESTIMATES

Flame ionization detectors give quantitative compositions of an inlet stream in the form of peak areas. Different components in the product stream have different combustion efficiencies, which are typically represented in the form of response factors. Although FID peak areas are not directly comparable, the choice of a reference compound and the normalization of all peak areas to that reference compound can be used to directly calculate a product distribution. These response factors can be determined through the injection of samples of varying but known composition containing the components of interest into the GC. However, it is not always practical to do so if these components are not readily available commercially. The response factor for a given component is related to its molecular structure. Therefore, if the molecular structure of a product molecule can be determined using MS, a response factor may be estimated. FID peak areas from the fixed bed reactor and pyroprobe experiments for the aldol condensation of butanal were analyzed using a group contribution method described by Scanlon and Willis [84]. In this method, an effective carbon number for a species is calculated based on its molecular structure. For the compounds of interest in this report, Table 8 shows the effective carbon number contribution used for each potentially relevant functional group, reproduced from the work by Scanlon and Willis [84].

Table 8: Effective carbon number contributions for relevant functional groups for the estimation of FID response factors based on molecular structure

Atom	Atomic Bonding	ECN contribution
C	Aliphatic or Aromatic	1
C	Olefinic	0.95
C	Carbonyl or Carboxyl	0
O	Ether	-1.0
O	Primary alcohol	-0.5
O	Secondary alcohol	-0.75

The effective carbon number (ECN) for a species is determined by the summation of effective carbon number contributions from each relevant atom. Based on the calculated effective carbon number, a response factor for the molecule may be calculated according to

$$\text{Molar Response Factor} = \frac{\text{ECN}_{\text{ref}}}{\text{ECN}_{\text{component}}} \quad (\text{A.1})$$

ECN_{ref} is the effective carbon number of a reference compound, and $\text{ECN}_{\text{component}}$ is the effective carbon number of a compound of interest. For the work conducted here with butanal, butanal is the reference compound and ECN_{ref} is equal to 3. Corrected peak areas are calculated according to

$$\text{Area}_{\text{corrected}} = \text{Area}_{\text{uncorrected}} * \text{Molar Response Factor} \quad (\text{A.2})$$

This technique was used to analyze GC data produced from the continuous-flow reactor. In all pyroprobe experiments in which oxygenates were detected, the ECN method was also used. However, when only hydrocarbon products were detected, such as with the sequential aldol condensation plus HDO experiments, a calibration had been developed for the GC relating peak area to product hydrocarbon mass, allowing for the analysis of GC data without the ECN method.

APPENDIX B. NREL LAP PROCEDURE

A procedure developed by NREL and published in the LAP manual was used to analyze the content of biomass-derived samples [85]. Filtering crucibles containing sample were heated in a muffle furnace at $575 \pm 25^{\circ}\text{C}$ for a period of at least four hours, after which they were removed from the furnace and placed in a desiccator to cool for one hour. 300.0 ± 10.0 mg of the sample or QA standard were weighed out into a pressure tube. 3.00 ± 0.01 mL (equivalent to 4.92 ± 0.01 g) of 72% sulfuric acid was added to each tube and stirred to ensure thorough mixing with the sample. The pressure tubes were then incubated in a water bath held at $30 \pm 3^{\circ}\text{C}$ for 60 ± 5 minutes to hydrolyze the sample, stirring every 5-10 minutes. The pressure tubes were then removed from the water bath and 84.00 ± 0.04 mL deionized water was added in order to dilute the acid to a concentration of 4%. The tubes and sugar recovery standards were then held at 121°C for an hour in an autoclave. After treatment in the autoclave, solutions in the pressure tubes were vacuum filtered using the filtering crucibles, retaining the filtrate in a filtering flask. The crucibles containing the acid insoluble residue were dried at $105 \pm 3^{\circ}\text{C}$ for approximately 4 hours, until the mass of the sample was constant within 0.1 mg. The crucibles and acid insoluble residue were then heated in a muffle furnace at $575 \pm 25^{\circ}\text{C}$ for 24 ± 6 hours, resulting in the formation of ash. The mass of the ash was then recorded. The acid soluble fraction was analyzed using absorbance and HPLC. Concentrations of carbohydrates were determined using HPLC and a known calibration. Acid soluble lignin content was determined by diluting samples to an absorbance range of 0.7-1.0 using either deionized water or 4% sulfuric acid, using the diluent as a blank.

APPENDIX C. DETAILED PRODUCT DISTRIBUTION OF PYROLYSIS OF NA-DOPED CELLOBIOSE

Table 9: Complete product selectivities for pyrolysis of cellobiose and cellobiose doped with 1 wt% NaCl solution and with 10 wt% NaCl solution

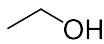
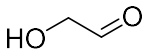
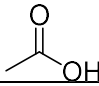
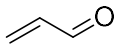
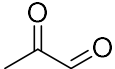
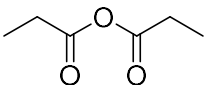
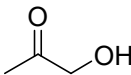
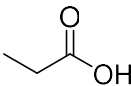
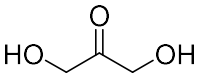
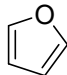
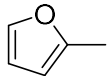
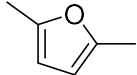
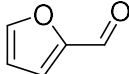
Peak	Cellobiose	1 wt % NaCl	10 wt % NaCl
	n.d.	0.45 ± 0.06	0.57 ± 0.02
	1.23 ± 0.23	1.18 ± 0.19	1.03 ± 0.04
	0.14 ± 0.01	0.28 ± 0.05	0.45 ± 0.06
	0.40 ± 0.08	0.25 ± 0.06	0.18 ± 0.02
	0.67 ± 0.10	1.29 ± 0.18	1.34 ± 0.06
	0.21 ± 0.02	0.31 ± 0.04	0.33 ± 0.01
	0.23 ± 0.01	0.92 ± 0.11	1.37 ± 0.03
	0.11 ± 0.02	0.13 ± 0.03	0.19 ± 0.02
	0.16 ± 0.04	0.23 ± 0.09	0.20 ± 0.05
	0.17 ± 0.01	0.03 ± 0.00	0.02 ± 0.01
	0.40 ± 0.02	0.49 ± 0.12	0.68 ± 0.11
	0.35 ± 0.04	0.49 ± 0.12	0.63 ± 0.04
	6.82 ± 0.41	4.87 ± 0.74	4.05 ± 0.21

Table 9 continued

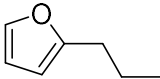
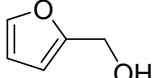
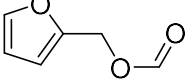
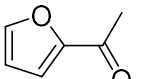
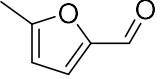
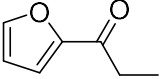
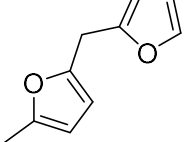
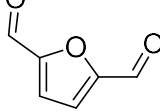
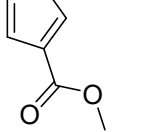
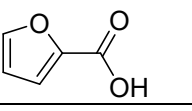

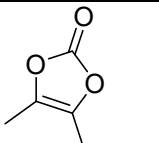
	0.57 ± 0.05	0.45 ± 0.07	0.46 ± 0.05
	0.23 ± 0.05	0.18 ± 0.13	0.71 ± 0.18
	0.03 ± 0.03	0.23 ± 0.07	0.20 ± 0.07
	0.13 ± 0.02	0.18 ± 0.03	0.23 ± 0.02
	1.16 ± 0.06	2.71 ± 0.35	1.65 ± 0.25
	0.26 ± 0.04	0.10 ± 0.00	0.10 ± 0.01
	0.23 ± 0.04	0.26 ± 0.05	0.32 ± 0.07
	0.46 ± 0.13	0.74 ± 0.04	0.78 ± 0.22
	0.59 ± 0.05	0.47 ± 0.11	0.40 ± 0.26
	0.22 ± 0.02	0.44 ± 0.07	0.64 ± 0.02
	0.13 ± 0.02	0.27 ± 0.08	0.35 ± 0.09
	0.10 ± 0.01	0.07 ± 0.03	0.06 ± 0.02

Table 9 continued

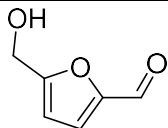
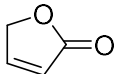
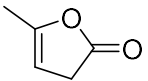
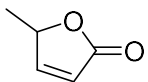
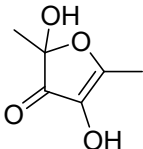
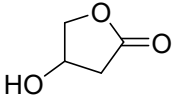
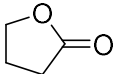
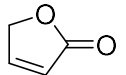
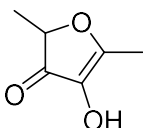
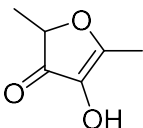
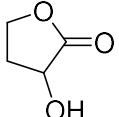
	15.68 ± 0.66	19.83 ± 4.58	18.16 ± 0.91
	1.99 ± 0.24	1.34 ± 0.25	1.86 ± 0.02
	0.12 ± 0.01	0.20 ± 0.05	0.22 ± 0.01
	0.03 ± 0.00	0.07 ± 0.01	0.10 ± 0.01
	0.02 ± 0.01	0.05 ± 0.02	0.05 ± 0.00
	0.64 ± 0.09	0.36 ± 0.05	0.28 ± 0.02
	0.10 ± 0.01	0.11 ± 0.03	0.12 ± 0.00
	0.19 ± 0.02	0.39 ± 0.07	0.53 ± 0.02
	0.08 ± 0.02	0.42 ± 0.06	0.44 ± 0.06
	0.38 ± 0.07	0.66 ± 0.09	0.84 ± 0.02
	0.06 ± 0.02	0.17 ± 0.02	0.29 ± 0.03

Table 9 continued

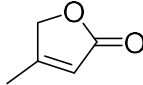
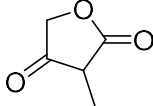
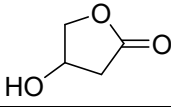
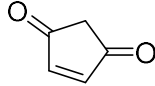
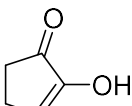
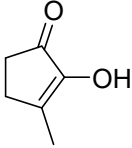
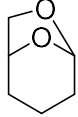
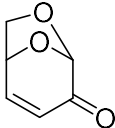
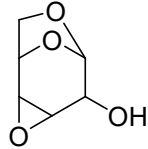
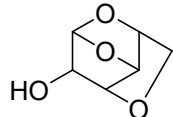
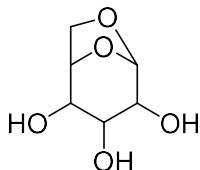
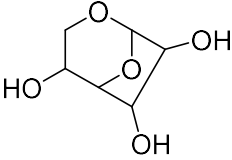
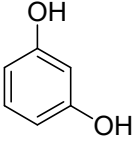
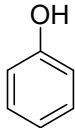
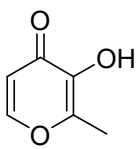
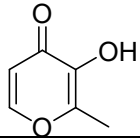
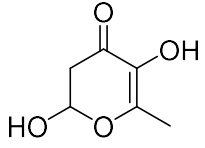
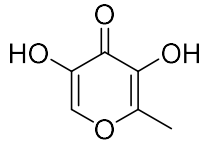
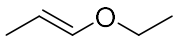
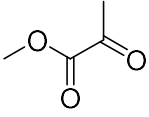
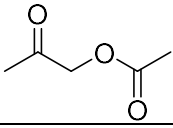
	0.04 ± 0.01	0.10 ± 0.01	0.16 ± 0.01
	0.07 ± 0.00	0.13 ± 0.02	0.15 ± 0.01
	0.16 ± 0.02	0.23 ± 0.05	0.20 ± 0.03
	0.08 ± 0.01	0.12 ± 0.01	0.18 ± 0.00
	0.88 ± 0.11	1.51 ± 0.21	1.52 ± 0.01
	0.40 ± 0.02	1.09 ± 0.19	1.35 ± 0.11
	0.71 ± 0.07	0.48 ± 0.04	0.59 ± 0.01
	2.31 ± 0.03	0.84 ± 0.08	1.92 ± 0.01
	0.11 ± 0.04	0.08 ± 0.01	0.26 ± 0.04
	1.59 ± 0.09	0.67 ± 0.05	1.06 ± 0.10
	4.63 ± 0.94	4.50 ± 1.34	3.02 ± 0.06

Table 9 continued

	0.38 ± 0.60	0.16 ± 0.11	0.07 ± 0.03
	0.18 ± 0.01	0.28 ± 0.04	0.45 ± 0.02
	0.16 ± 0.02	0.12 ± 0.03	0.12 ± 0.04
	0.09 ± 0.05	0.09 ± 0.02	0.20 ± 0.35
	0.22 ± 0.02	0.33 ± 0.03	0.43 ± 0.01
	0.35 ± 0.03	0.55 ± 0.13	0.52 ± 0.02
	0.18 ± 0.05	0.25 ± 0.08	0.55 ± 0.04
	0.18 ± 0.02	0.19 ± 0.03	0.22 ± 0.00
	0.05 ± 0.02	0.30 ± 0.03	0.33 ± 0.02
	0.02 ± 0.00	0.14 ± 0.03	0.14 ± 0.01

APPENDIX D. N₂ ADSORPTION ISOTHERMS FOR NI-MCM-41, NI-BETA, NI-FAU-6, AND NI-FAU-40

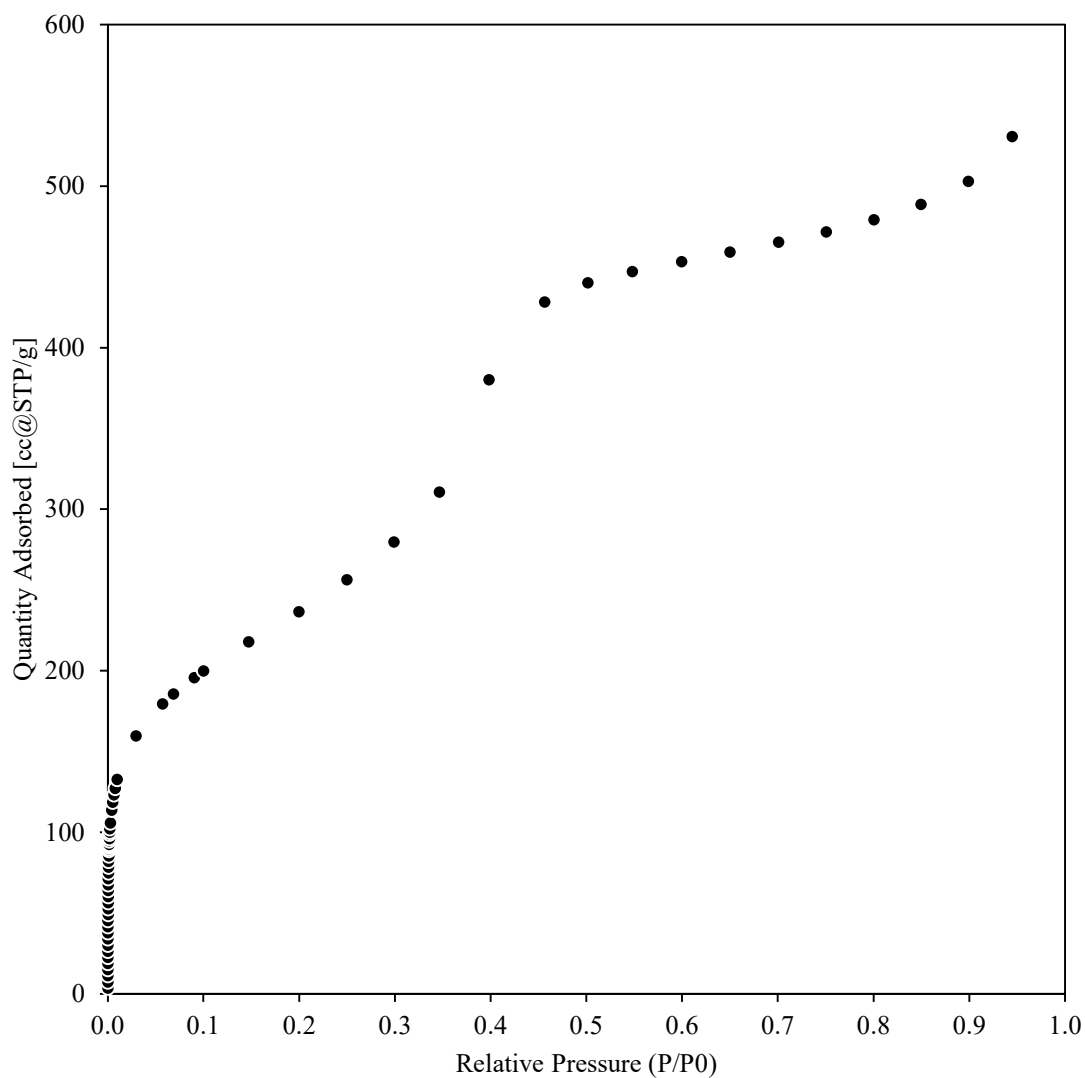


Figure 33. N₂ adsorption-desorption (77 K) isotherm for Ni-MCM-41.

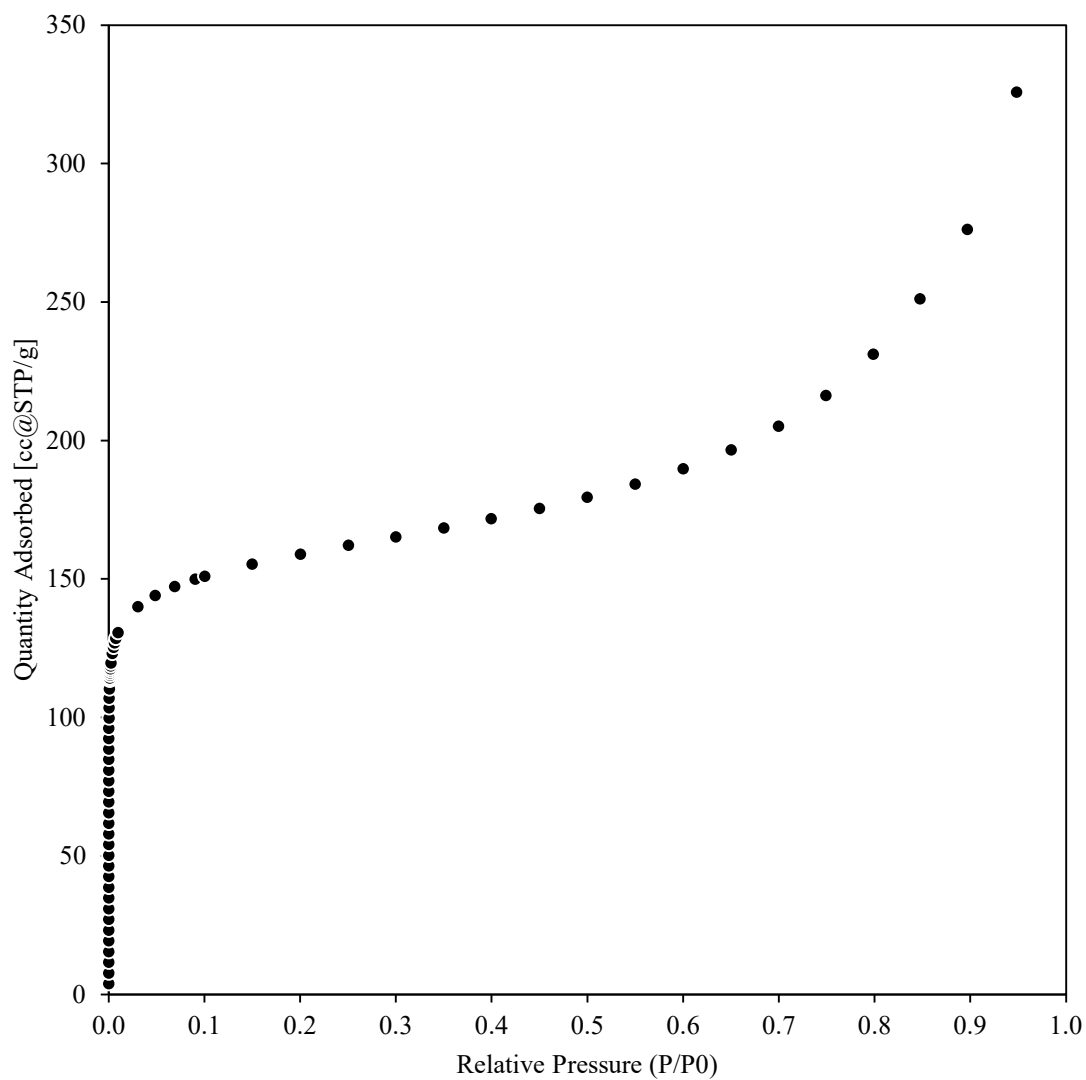


Figure 34. N₂ adsorption-desorption (77 K) isotherm for Ni-Beta.

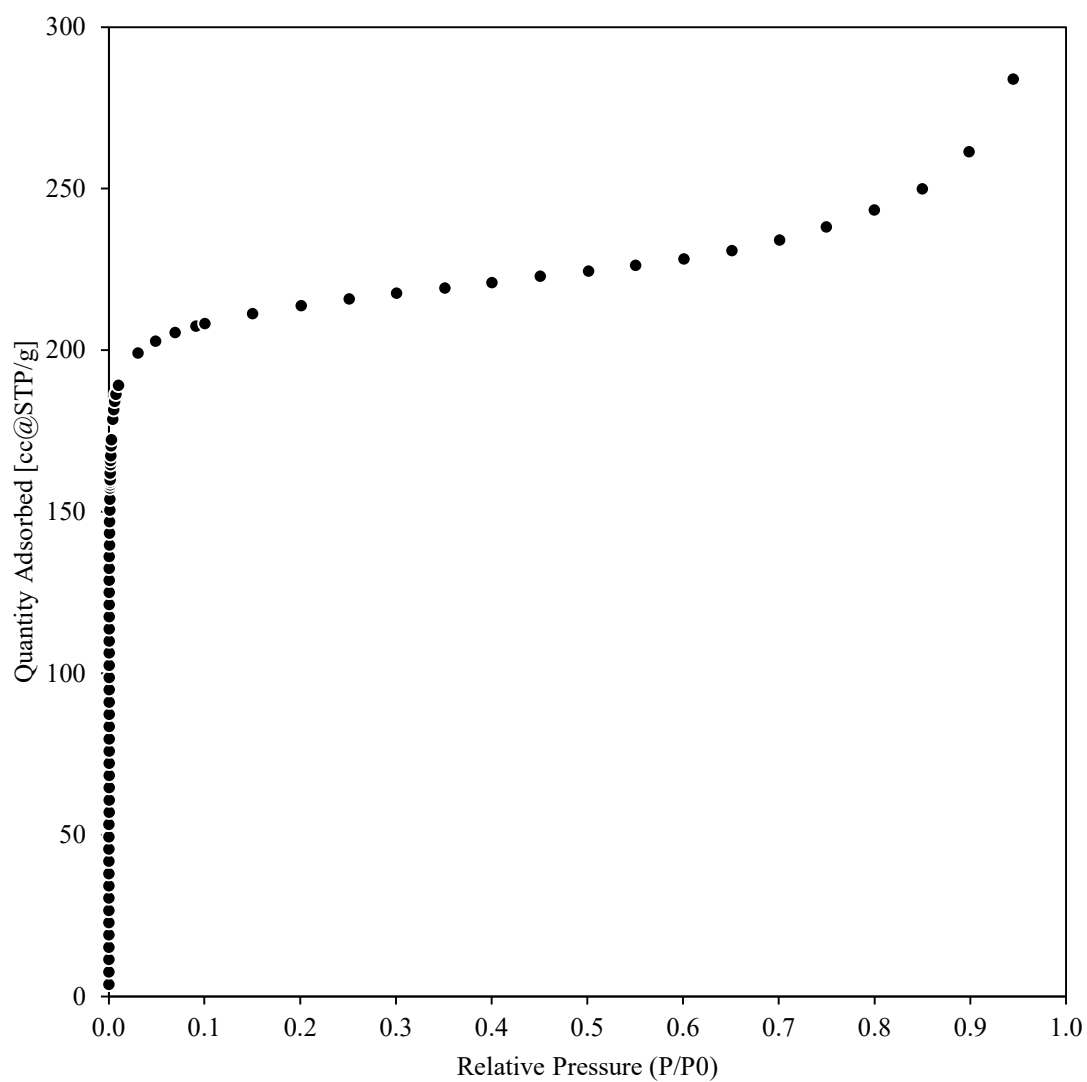


Figure 35. N_2 adsorption-desorption (77 K) isotherm for Ni-FAU-6.

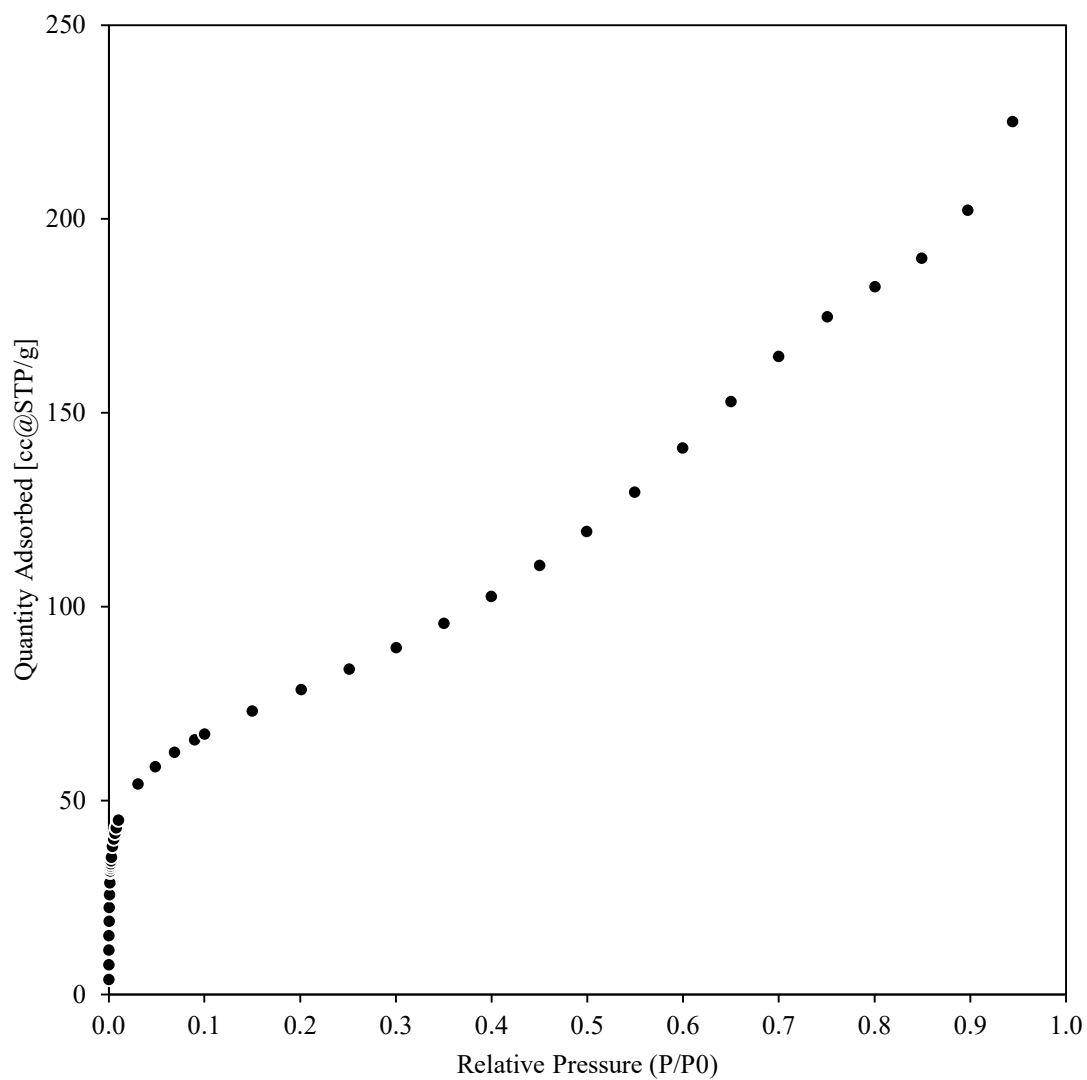


Figure 36. N₂ adsorption-desorption (77 K) isotherm for Ni-Li-FAU-40

APPENDIX E. PORE SIZE DISTRIBUTIONS FOR NI-MCM-41, NI-BETA, NI-FAU-6, AND NI-FAU-40

Ar adsorption isotherms (87 K) were also measured for these samples in order to determine their pore size distributions, with the exception of Ni-Li-FAU-40, for which N₂ adsorption isotherms (77 K) were measured instead.

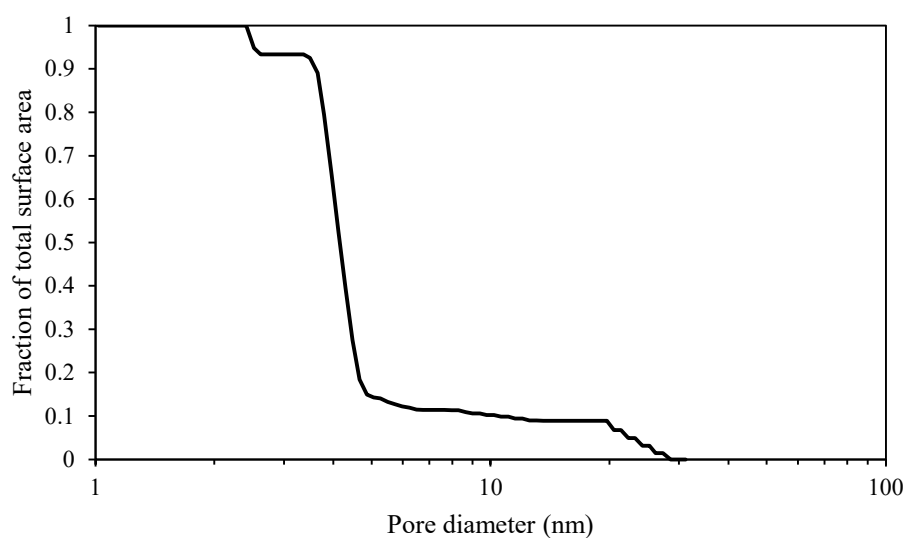


Figure 37. Fraction of total surface area contained within a given pore diameter for 0.63 wt% Ni-MCM-41. The bulk of the surface area is contained in pores between 3-5 nm in diameter, with 85% of total surface area contained in pores <5 nm in diameter.

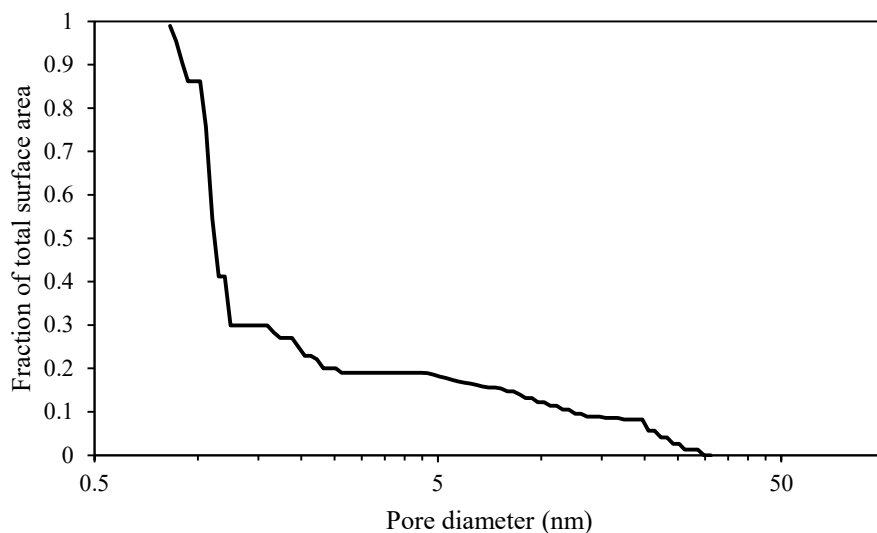


Figure 38. Fraction of total surface area contained within a given pore diameter for Ni-Beta. Most of the surface area is contained within pores <1.2 nm diameter, with 70% of total surface area in pores <1.3 nm in diameter.

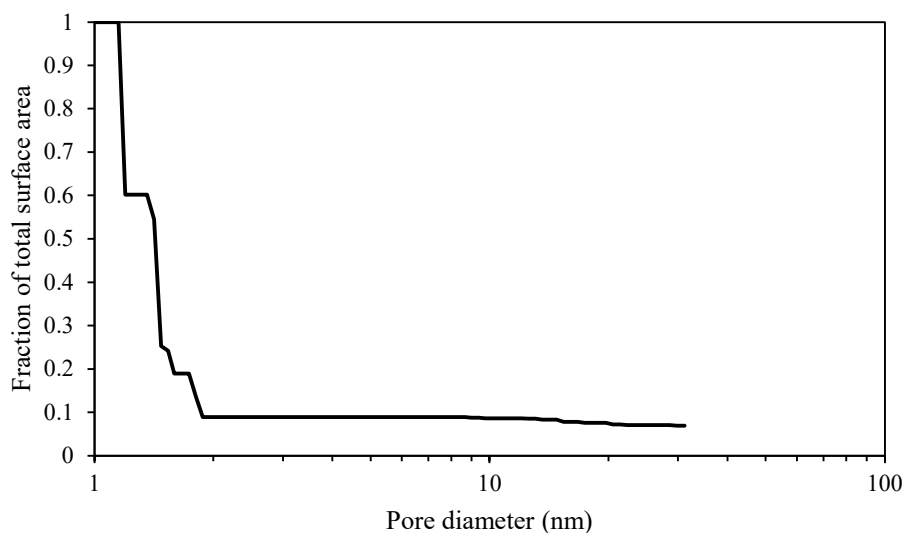


Figure 39. Fraction of total surface area contained within a given pore diameter for Ni-FAU-6. Most surface area is contained within pores of <1.5 nm diameter, with 90% of total surface area in pores <1.9 nm diameter.

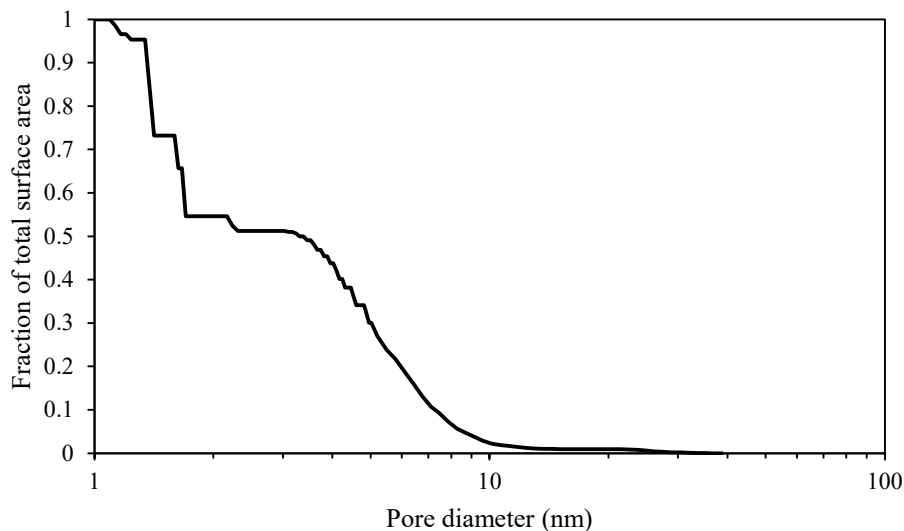


Figure 40. Fraction of total surface area contained within a given pore diameter for Ni-Li-FAU-40. Surface area is split between micropores and mesopores. Approximately 50% of total surface area lies in micropores with 1.4-1.7 nm diameter, while the remaining 50% of total surface area lies in mesopores with 3.5-10 nm diameter.

Pore diameters obtained from pore size distributions can then be used to estimate capillary condensation pressures according to the Kelvin equation:

$$\ln\left(\frac{P}{P_0}\right) = \frac{2\sigma M}{\rho r RT} \quad (\text{E.1})$$

where P is the pressure, P_0 is the bulk saturation pressure ($P_0 = 19.3$ bar at 243 K; $P_0 = 28.6$ bar at 258 K), σ is the surface tension, M is the molecular weight, ρ is the fluid density, r is the pore diameter, R is the ideal gas constant, and T is the temperature. Estimates of the capillary condensation pressure for each material are shown in Table 10, using a liquid ethene density of 0.016 N/m and a density of 5.67×10^5 g/m³. Calculations are performed at 243 K for Ni-MCM-41 and at 258 K for Ni-Beta, Ni-FAU-6, and Ni-FAU-40.

The number of Ni per unit cell was calculated from the unit cell formula and structural composition data (Ni/Al, H⁺/Al, and Si/Al) for Beta and FAU samples. The average Ni-Ni distance was estimated by dividing the shortest unit cell length ($a = b = 1.26$ nm for Beta; $a = b = c = 2.43$ nm for FAU) by the number of Ni per unit cell. The Ni site density (Table 10) was calculated as

(Ni atoms per g_{zeolite})/(micropore volume per g_{zeolite}) using the measured Ni loading (wt. %) and micropore volume from N₂ adsorption.

Table 10. Summary of pore characterization for Ni-MCM-41, Ni-Beta, and Ni-FAU samples

Sample	Pore diam. (nm)	Micropore volume (cm³ g⁻¹)	Ni loading (wt. %)	Ni site density (Ni/nm³)	Ni atoms per unit cell	Avg. Ni-Ni distance (nm)	Capillary Condensation Pressure (bar)
Ni-MCM-41	3 – 5	0.62 ^a	1.1	0.18			14.6 ^b
Ni-Beta	1.1 – 1.3	0.16	1.4	0.93	1.3	0.8	14.4 ^c
Ni-FAU-6	1.2 – 1.5	0.21	0.7	0.33	1.9	1.3	15.3 ^c
Ni-FAU-40	1.4 – 1.7	0.27	0.3	0.12	0.9	2.6	16.7 ^c

^aDenotes mesopore volume for Ni-MCM-41 rather than micropore volume.

^bCapillary condensation pressure calculated at 243 K

^cCapillary condensation pressure calculated at 258 K

APPENDIX F. EFFECTS OF BRØNSTED ACID SITES ON DEACTIVATION

The role of Brønsted acid sites in deactivation of Ni-FAU was also investigated to eliminate their presence as a potential lurking variable in observed deactivation phenomena. Acid sites were eliminated from Ni-FAU-40 by performing a Li exchange of FAU prior to Ni exchange, ultimately resulting in the formation of Ni-Li-FAU. Ethene oligomerization rates were measured over Ni-Li-FAU-40 under the same conditions as that for Ni-H-FAU-40 (Ni-FAU-40), with data reported in Figure 41. Total alkene formation rates (per Ni) in both catalysts decay to approximately the same value over time, suggesting that acid sites do not significantly contribute to observed rates, as expected based on the low rates of Brønsted-acid catalyzed reactions at temperatures below 298 K. Ethene oligomerization rates in H-MCM-41 at 258 K will be discussed later, and are shown in Figure 42. However, there exist significant differences between the activation periods of Ni-Li-FAU and Ni-H-FAU. An activation period observed in Ni-H-FAU can be entirely suppressed by H₂ co-feed, while the same co-feed only eliminates a portion of the activation period of Ni-Li-FAU.

Deactivation in Ni-Li-FAU was slower than in Ni-H-FAU, but the activation period for Ni-Li-FAU could not be deconvoluted from deactivation fits. First- and second-order models provided similarly good fits to the data. The difference in deactivation constants could be due to the convoluting influence of a lengthy activation period, or could also suggest that either elimination of residual acid sites or their exchange with Li ions may influence deactivation. Regardless, operation under capillary condensation conditions did not affect deactivation in Ni-Li-FAU.

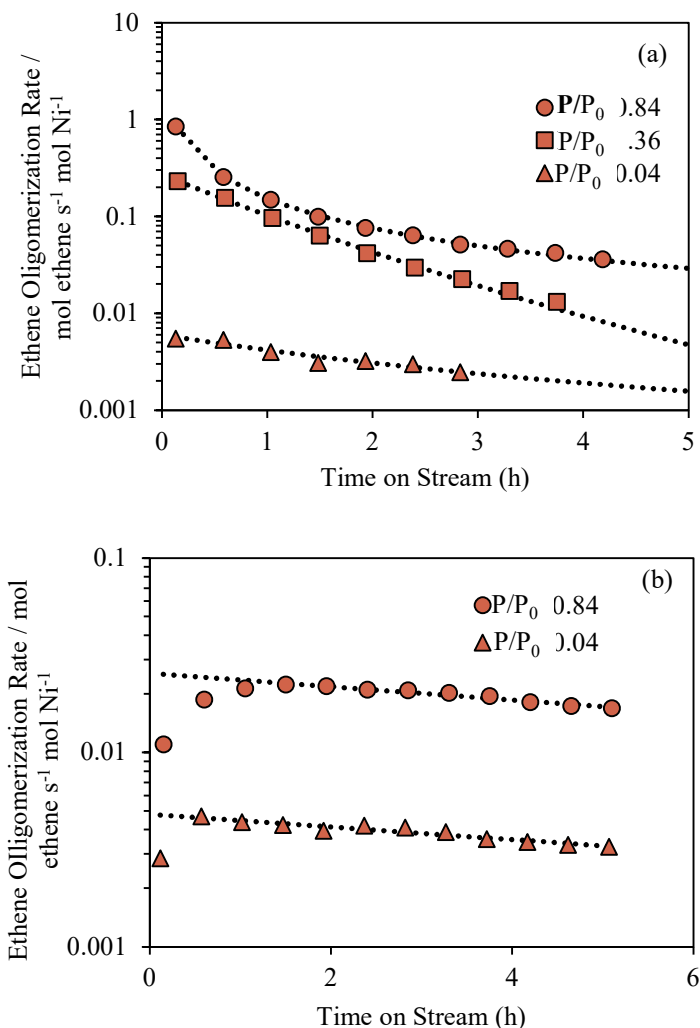


Figure 41. Ethene oligomerization rates as a function of time-on-stream for (a) Ni-FAU-40 (Si/Al = 40, Ni/Al = 0.20, 0.3 wt. % Ni) and (b) Ni-Li-FAU-40 (Si/Al = 40, Ni/Al = 0.26, 0.5 wt. % Ni), collected at 258 K. Fits to deactivation models are shown in dashed lines. H₂ was co-fed at a concentration of 1% of the total feed.

H-form Al-MCM-41 was also examined for ethene oligomerization at reaction conditions similar to those used for the Ni-exchanged samples. In order to observe any formation of butene, these experiments were conducted at 258 K and not at 243 K. Rates on a per-gram basis can be seen in Figure 42. Although butene formation was observed, oligomerization rates were several orders of magnitude lower ($10^{-7} - 10^{-8}$ mol ethene g⁻¹ s⁻¹ for H-MCM-41 at 258 K) than those observed for Ni-exchanged samples ($10^{-4} - 10^{-5}$ mol ethene g⁻¹ s⁻¹ for Ni-MCM-41 at 243 K).

Steady deactivation was observed at pressures below and above the capillary condensation threshold on H-MCM-41. We speculate that alkenes may bind more tightly to Brønsted acid sites than to active Ni species, such that solvation by a condensed ethene phase is insufficient to overcome desorption barriers for heavier products in H-MCM-41.

Table 11. Fitted parameters to the Butt-Peterson deactivation model (Eq. (3.1) for Ni-Li-FAU-40.

Sample	P/P ₀	k _d ^a	r ₀ (mol ethene s ⁻¹ mol Ni ⁻¹)	n	R ²
Ni-Li-FAU-40	0.04	2.41 x 10 ⁻⁵ ± 0.97 x 10 ⁻⁵	4.80 x 10 ⁻³ ± 0.19 x 10 ⁻⁴	1.0 ± 2.2	0.92
Ni-Li-FAU-40	0.84	2.50 x 10 ⁻⁵ ± 0.63 x 10 ⁻⁵	2.55 x 10 ⁻² ± 0.16 x 10 ⁻³	1.0 ± 2.1	0.96

^aUnits for k_d: mol Niⁿ⁻¹ (mol C₂)¹⁻ⁿ sⁿ⁻².

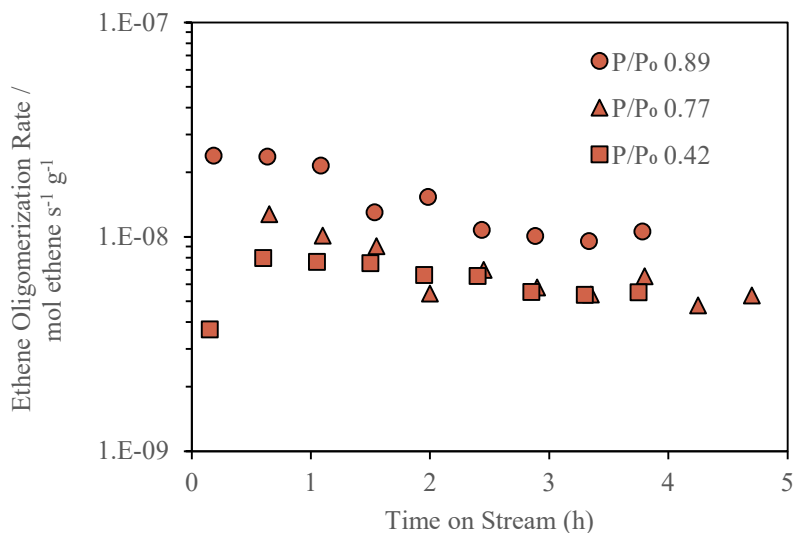


Figure 42. Ethene oligomerization rates on H-MCM-41 at 258 K and 12-26 bar ethene ($P_0 = 28.4$ bar for ethene at 258 K). $0.85 \text{ mol ethene g}^{-1} \text{ h}^{-1}$ flow at $P/P_0 = 0.42$ and $1.9 \text{ mol ethene g}^{-1} \text{ h}^{-1}$ at $P/P_0 = 0.77$ and $P/P_0 = 0.89$.

APPENDIX G. STATISTICAL GOODNESS-OF-FIT ANALYSIS OF DEACTIVATION PARAMETER FITTING

Deactivation of Ni sites was modeled according to the method previously developed by Butt [80] and discussed in detail by Saxena et al. [67], yielding the final equation:

$$r = \frac{r_0}{(1 + (n-1)k_d r_0^{n-1} t)^{\frac{1}{n-1}}} \quad (\text{G.1})$$

A Python code previously used by Saxena et al. [67] was modified and used to fit data to this equation by minimizing least-squared errors.

For many of the data sets reported here, this approach resulted in apparent over-fitting of deactivation orders, resulting in deactivation orders as high as $n = 5$ for some data sets. For data sets that yielded deactivation orders $n > 2.3$, values of n were fixed in increments of 0.01 starting at $n = 1.01$ and ending at $n = 2.3$, and at each increment the Python code was used to find values of k_d and r_0 , and a corresponding standard error was calculated according to Eq. (G.2):

$$\% \text{ standard error} = \sqrt{\frac{\sum \left(\frac{r_{\text{predicted}} - r_{\text{measured}}}{r_{\text{predicted}}} \right)^2}{\text{Number of data points}}} \quad (\text{G.2})$$

Once a deactivation order was found for which the standard error was less than 5%, the corresponding values of r_0 and k_d were reported at this condition. In the event that a standard error less than 5% could not be achieved without exceeding the imposed limit of $n < 2.3$, the data was fit with power-law models of $n = 1$ and $n = 2$, and the result with higher R^2 value is reported. Deactivation model parameters and their corresponding errors are reported in Table 12. Large uncertainties result when fitting deactivation orders for samples and conditions that lead to low measured rates (Ni-Beta, Ni-FAU-6, and Ni-FAU-40 at $P/P_0 = 0.04$). For samples and conditions

that lead to higher measured rates (Ni-FAU-40 at $P/P_0 = 0.36$ and $P/P_0 = 0.84$; Ni-MCM-41 at $P/P_0 = 0.36$), the uncertainty in fitted deactivation orders are diminished.

Table 12. Deactivation model parameters for Ni-MCM-41, Ni-Beta, Ni-FAU-6, and Ni-FAU-40 at 258 K

Sample	P/P_0	k_d^a	r_0 (mol ethene s^{-1} mol Ni $^{-1}$)	n	R^2	% standard error
Ni-MCM-41	0.36	3.15 ± 0.61	0.493 ± 0.038	1.93 ± 0.30	0.98	4.9
Ni-MCM-41	0.71	0	0.463 ± 0.018	0		
Ni-MCM-41	0.89	0	0.899 ± 0.013	0		
Ni-Beta	0.04	$6.07 \times 10^{-4} \pm$ 1.72×10^{-4}	$4.59 \times 10^{-3} \pm$ 0.59×10^{-3}	2^b	0.90	12.8
Ni-Beta	0.24	$8.49 \times 10^{-3} \pm$ 53.9×10^{-3}	$1.62 \times 10^{-2} \pm$ 0.16×10^{-2}	1.76 ± 1.05	0.90	3.0
Ni-Beta	0.84	$3.90 \times 10^{-2} \pm$ 31.5×10^{-2}	$4.90 \times 10^{-2} \pm$ 0.73×10^{-2}	2.22 ± 1.65	0.85	4.3
Ni-FAU-6	0.04	$3.04 \times 10^2 \pm$ 1.53×10^2	$1.23 \times 10^{-3} \pm$ 0.22×10^{-3}	1.95 ± 1.59	0.91	2.3
Ni-FAU-6	0.36	$2.13 \times 10^3 \pm$ 0.50×10^3	$2.82 \times 10^{-2} \pm$ 0.57×10^{-2}	2.18 ± 0.30	0.97	5.0
Ni-FAU-6	0.84	$1.52 \times 10^{-3} \pm$ 0.90×10^{-3}	$2.72 \times 10^{-2} \pm$ 0.31×10^{-2}	1.21 ± 0.94	0.87	5.0
Ni-FAU-40	0.04	0.741 ± 0.321	$6.00 \times 10^{-3} \pm$ 0.55×10^{-3}	1.58 ± 1.25	0.92	2.9
Ni-FAU-40	0.36	$9.98 \times 10^{-4} \pm$ 0.44×10^{-4}	0.271 ± 0.005	1.11 ± 0.05	1.00	4.1
Ni-FAU-40	0.84	16.1 ± 0.3	2.37 ± 0.11	1.94 ± 0.02	1.00	0.9

^aUnits for k_d : mol Ni $^{n-1}$ (mol ethene) $^{1-n}$ s $^{-n-2}$.

^bFitting to the generalized deactivation model could not be achieved within specified limits ($n < 2.3$, standard error < 0.05) and data were thus fit to either $n = 1$ or $n = 2$ power law models.

Alternatively, deactivation can be modeled using a power law model:

$$\frac{d}{dt} \left(\frac{r}{r_0} \right) = -k_d \left(\frac{r}{r_0} \right)^n \quad (G.3)$$

Values of $n = 1$ and 2 can be assumed to obtain the following equations describing the rate for first-order (Eq. G.4) and second-order (Eq. G.5) deactivation:

$$r = r_0 \exp(-k_d t) \quad (G.4)$$

$$r = \frac{r_0}{1 + k_d t} \quad (G.5)$$

Deactivation model parameters can then be calculated for the first-order and second-order models for each catalyst and condition, comparing the quality of fit by calculating R^2 in order to determine the appropriate deactivation order. Fits to the first-order deactivation model (Eq. G.4) are shown in Table 13, while fits to the second-order deactivation model (Eq. G.5) are shown in Table 14. Comparing R^2 values between the assumed first-order and second-order models confirms conclusions from fitting to the Butt model. The second-order model is more accurate for Ni-Beta and Ni-FAU-6 under all conditions. The first-order model is more accurate for Ni-FAU-40 at $P/P_0 = 0.36$ and the second-order model is more accurate for Ni-FAU-40 at $P/P_0 = 0.84$. At $P/P_0 = 0.04$, first-order and second-order models fit the data equally well for Ni-FAU-40, reflecting the uncertainty in ethene oligomerization rate measurements at this condition.

Table 13. Deactivation model parameters for Ni-MCM-41, Ni-Beta, Ni-FAU-6, and Ni-FAU-40 at 258 K according to a first-order deactivation model.

Sample	P/P_0	k_d (s^{-1})	r_0 (mol ethene s^{-1} mol Ni^{-1})	R^2
Ni-MCM-41	0.36	$9.98 \times 10^{-5} \pm 0.9 \times 10^{-5}$	0.228 ± 0.013	0.951
Ni-MCM-41	0.71	0	0.463 ± 0.018	0
Ni-MCM-41	0.89	0	0.899 ± 0.013	0
Ni-Beta	0.04	$4.92 \times 10^{-5} \pm 1.05 \times 10^{-5}$	$1.57 \times 10^{-3} \pm 0.11 \times 10^{-3}$	0.808
Ni-Beta	0.24	$5.84 \times 10^{-5} \pm 0.57 \times 10^{-5}$	$1.28 \times 10^{-2} \pm 0.05 \times 10^{-2}$	0.947
Ni-Beta	0.84	$3.75 \times 10^{-5} \pm 0.68 \times 10^{-5}$	$3.23 \times 10^{-2} \pm 0.14 \times 10^{-2}$	0.883
Ni-FAU-6	0.04	$5.70 \times 10^{-5} \pm 0.83 \times 10^{-5}$	$1.13 \times 10^{-3} \pm 0.07 \times 10^{-3}$	0.888
Ni-FAU-6	0.36	$7.67 \times 10^{-5} \pm 1.1 \times 10^{-5}$	$1.07 \times 10^{-2} \pm 0.09 \times 10^{-2}$	0.876
Ni-FAU-6	0.84	$6.14 \times 10^{-5} \pm 0.97 \times 10^{-5}$	$2.10 \times 10^{-2} \pm 0.14 \times 10^{-2}$	0.872
Ni-FAU-40	0.04	$8.78 \times 10^{-5} \pm 1.21 \times 10^{-5}$	$5.82 \times 10^{-3} \pm 0.33 \times 10^{-3}$	0.919
Ni-FAU-40	0.36	$2.53 \times 10^{-4} \pm 0.11 \times 10^{-4}$	0.261 ± 0.011	0.993
Ni-FAU-40	0.84	$2.06 \times 10^{-4} \pm 0.24 \times 10^{-4}$	0.361 ± 0.038	0.941

While the uncertainties in fitted deactivation orders from the Butt model preclude an unambiguous estimate of deactivation orders in some data sets, first-order deactivation can be concluded for Ni-FAU-40 at $P/P_0 = 0.36$ and second-order deactivation can be concluded for Ni-FAU-40 at $P/P_0 = 0.84$. Although the large uncertainty in deactivation order for Ni-FAU-40 at $P/P_0 = 0.04$ cannot unambiguously distinguish between first- and second-order deactivation at this condition, first-order deactivation would be the more consistent option, given the first-order deactivation observed at $P/P_0 = 0.36$ and the low Ni density of this sample. Similarly, second-order deactivation is most consistent with the calculated deactivation orders for Ni-Beta and Ni-FAU-6, given the high Ni densities of these samples.

Table 14. Deactivation model parameters for Ni-MCM-41, Ni-Beta, Ni-FAU-6, and Ni-FAU-40 at 258 K according to a second-order deactivation model.

Sample	P/P_0	k_d (s^{-1})	r_0 (mol ethene s^{-1} mol Ni $^{-1}$)	R^2
Ni-MCM-41	0.36	$2.83 \times 10^{-4} \pm 0.15 \times 10^{-4}$	0.314 ± 0.009	0.996
Ni-MCM-41	0.71	0	0.463 ± 0.018	0
Ni-MCM-41	0.89	0	0.899 ± 0.013	0
Ni-Beta	0.04	$7.63 \times 10^{-5} \pm 1.89 \times 10^{-5}$	$1.68 \times 10^{-3} \pm 0.13 \times 10^{-3}$	0.858
Ni-Beta	0.24	$9.23 \times 10^{-5} \pm 1.08 \times 10^{-5}$	$1.37 \times 10^{-2} \pm 0.05 \times 10^{-2}$	0.964
Ni-Beta	0.84	$4.91 \times 10^{-5} \pm 1.02 \times 10^{-5}$	$3.32 \times 10^{-2} \pm 0.15 \times 10^{-2}$	0.901
Ni-FAU-6	0.04	$9.52 \times 10^{-5} \pm 1.96 \times 10^{-5}$	$1.23 \times 10^{-3} \pm 0.09 \times 10^{-3}$	0.907
Ni-FAU-6	0.36	$1.93 \times 10^{-4} \pm 0.35 \times 10^{-4}$	$1.40 \times 10^{-2} \pm 0.14 \times 10^{-2}$	0.948
Ni-FAU-6	0.84	$1.12 \times 10^{-4} \pm 0.23 \times 10^{-4}$	$2.37 \times 10^{-2} \pm 0.19 \times 10^{-2}$	0.914
Ni-FAU-40	0.04	$1.36 \times 10^{-4} \pm 0.27 \times 10^{-4}$	$6.11 \times 10^{-3} \pm 0.41 \times 10^{-3}$	0.922
Ni-FAU-40	0.36	$4.43 \times 10^{-3} \pm 8.55 \times 10^{-3}$	1.55 ± 2.78	0.954
Ni-FAU-40	0.84	$4.39 \times 10^{-3} \pm 1.71 \times 10^{-3}$	2.54 ± 0.92	0.997

As previously mentioned, if the value of n is unconstrained and Eq. (G.1) is fit to the data by minimizing least-squared error, significant over-fitting of data can be observed. These model parameters and their corresponding errors are given in Table 15 for reference.

Table 15. Deactivation model parameters for Ni-MCM-41, Ni-Beta, Ni-FAU-6, and Ni-FAU-40 at 258 K without constraint on the deactivation order n and fit by minimizing least squares

Sample	P/P ₀	k _d ^a	r ₀ (mol ethene s ⁻¹ mol Ni ⁻¹)	n	R ²
Ni-MCM-41	0.36	3.76 x 10 ³ ± 0.12 x 10 ³	3.92 x 10 ⁻² ± 0.21 x 10 ⁻²	2.62 ± 0.04	0.999
Ni-MCM-41	0.71	0	0.463 ± 0.018	0	
Ni-MCM-41	0.89	0	0.899 ± 0.013	0	
Ni-Beta	0.04	3.10 x 10 ¹⁰ ± 1.43 x 10 ¹⁰	3.92 x 10 ⁻² ± 0.21 x 10 ⁻²	3.22 ± 0.54	0.981
Ni-Beta	0.24	5.50 x 10 ⁴ ± 16.4 x 10 ⁴	0.159 ± 0.038	4.35 ± 0.5	0.984
Ni-Beta	0.84	9.72 x 10 ³ ± 42.7 x 10 ³	0.488 ± 0.520	4.75 ± 0.9	0.98
Ni-FAU-6	0.04	2.82 x 10 ⁷ ± 1.38 x 10 ⁷	1.34 x 10 ⁻³ ± 0.38 x 10 ⁻³	2.65 ± 1.61	0.91
Ni-FAU-6	0.36	1.21 x 10 ⁷ ± 0.16 x 10 ⁷	0.186 ± 0.145	2.81 ± 0.17	0.995
Ni-FAU-6	0.84	1.97 x 10 ¹⁰ ± 0.42 x 10 ¹⁰	4.01 x 10 ⁻² ± 0.63 x 10 ⁻²	3.49 ± 0.39	0.986
Ni-FAU-40	0.04	0.740 ± 0.321	6.00 x 10 ⁻³ ± 0.55 x 10 ⁻³	1.59 ± 1.25	0.924
Ni-FAU-40	0.36	9.98 x 10 ⁻⁴ ± 0.44 x 10 ⁻⁴	0.271 ± 0.005	1.11 ± 0.05	0.998
Ni-FAU-40	0.84	16.1 ± 0.3	2.37 ± 0.11	1.94 ± 0.02	0.999

^aUnits for k_d: mol Niⁿ⁻¹ (mol ethene)¹⁻ⁿ sⁿ⁻².

APPENDIX H. MODELING OF DEACTIVATION TRANSIENTS IN DATA FROM AGIRREZABAL-TELLERIA AND IGLESIA

The Butt-Peterson model (Eq. (3.1)) used to calculate fitting parameters for data measured in this work can also be applied to data reported in the literature for comparison. Agirrezabal-Telleria and Iglesia reported on deactivation during ethene oligomerization in Ni-MCM-41 at 243 K and high ethene pressures and reported first-order deactivation constants at all pressures tested [78]. This is in apparent contrast to the finding reported in this work, where deactivation model fitting to data on Ni-MCM-41 at 6.8 bar resulted in estimating a deactivation order of 1.9. Application of the Butt-Peterson model to the data reported by Agirrezabal-Telleria and Iglesia shows that an order closer to 2 can be obtained.

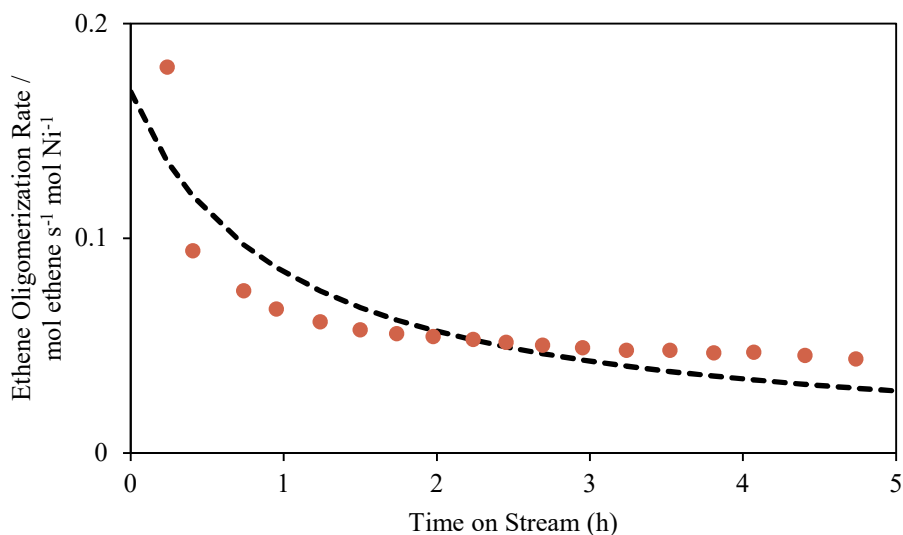


Figure 43. Fit of ethene oligomerization data on Ni-MCM-41 at 243 K and 9 bar ethene from Agirrezabal-Telleria and Iglesia to the Butt-Peterson deactivation model (Eq. (3.1)). Data shown is extracted from Figure 5 of Agirrezabal-Telleria and Iglesia [78].

Table 16. Deactivation model parameters for Ni-MCM-41.

Sample	P/P₀	k_d	r₀ (mol ethene s⁻¹ mol Ni⁻¹)	n	R²
Ni-MCM-41[78]	0.48	2.77 ± 20.28	0.456 ± 0.043	2.04 ± 0.76	0.96

^aUnits for k_d: mol Niⁿ⁻¹ (mol ethene)¹⁻ⁿ sⁿ⁻².

REFERENCES

- [1] V.K. Venkatakrishnan, W.N. Delgass, F.H. Ribeiro, R. Agrawal, Oxygen removal from intact biomass to produce liquid fuel range hydrocarbons via fast-hydropyrolysis and vapor-phase catalytic hydrodeoxygenation, *Green Chem.* 17 (2014) 178–183.
<https://doi.org/10.1039/C4GC01746C>.
- [2] Annual Energy Outlook 2015 - Energy Information Administration, (n.d.).
<http://www.eia.gov/forecasts/archive/aeo15/> (accessed July 16, 2016).
- [3] S. Singh, S. Jain, V. PS, A.K. Tiwari, M.R. Nouni, J.K. Pandey, S. Goel, Hydrogen: A sustainable fuel for future of the transport sector, *Renewable and Sustainable Energy Reviews.* 51 (2015) 623–633. <https://doi.org/10.1016/j.rser.2015.06.040>.
- [4] R. Agrawal, N.R. Singh, Synergistic routes to liquid fuel for a petroleum-deprived future, *AIChE J.* 55 (2009) 1898–1905. <https://doi.org/10.1002/aic.11785>.
- [5] R. Agrawal, N.R. Singh, F.H. Ribeiro, W.N. Delgass, Sustainable fuel for the transportation sector, *PNAS.* 104 (2007) 4828–4833. <https://doi.org/10.1073/pnas.0609921104>.
- [6] N. Mosier, C. Wyman, B. Dale, R. Elander, Y.Y. Lee, M. Holtzapple, M. Ladisch, Features of promising technologies for pretreatment of lignocellulosic biomass, *Bioresource Technology.* 96 (2005) 673–686. <https://doi.org/10.1016/j.biortech.2004.06.025>.
- [7] P.R. Patwardhan, D.L. Dalluge, B.H. Shanks, R.C. Brown, Distinguishing primary and secondary reactions of cellulose pyrolysis, *Bioresource Technology.* 102 (2011) 5265–5269. <https://doi.org/10.1016/j.biortech.2011.02.018>.
- [8] V.K. Venkatakrishnan, J.C. Degenstein, A.D. Smeltz, W.N. Delgass, R. Agrawal, F.H. Ribeiro, High-pressure fast-pyrolysis, fast-hydropyrolysis and catalytic hydrodeoxygenation of cellulose: production of liquid fuel from biomass, *Green Chemistry.* 16 (2014) 792. <https://doi.org/10.1039/c3gc41558a>.
- [9] P.R. Patwardhan, J.A. Satrio, R.C. Brown, B.H. Shanks, Product distribution from fast pyrolysis of glucose-based carbohydrates, *Journal of Analytical and Applied Pyrolysis.* 86 (2009) 323–330. <https://doi.org/10.1016/j.jaap.2009.08.007>.
- [10] P.R. Patwardhan, R.C. Brown, B.H. Shanks, Product Distribution from the Fast Pyrolysis of Hemicellulose, *ChemSusChem.* 4 (2011) 636–643. <https://doi.org/10.1002/cssc.201000425>.

- [11] P.R. Patwardhan, R.C. Brown, B.H. Shanks, Understanding the Fast Pyrolysis of Lignin, *ChemSusChem*. 4 (2011) 1629–1636. <https://doi.org/10.1002/cssc.201100133>.
- [12] J.C. Degenstein, P. Murria, M. Easton, H. Sheng, M. Hurt, A.R. Dow, J. Gao, J.J. Nash, R. Agrawal, W.N. Delgass, F.H. Ribeiro, H.I. Kenttämä, Fast Pyrolysis of ¹³C-Labeled Cellobioses: Gaining Insights into the Mechanisms of Fast Pyrolysis of Carbohydrates, *J. Org. Chem.* 80 (2015) 1909–1914. <https://doi.org/10.1021/jo5025255>.
- [13] J.C. Degenstein, M. Hurt, P. Murria, M. Easton, H. Choudhari, L. Yang, J. Riedeman, M.S. Carlsen, J.J. Nash, R. Agrawal, W.N. Delgass, F.H. Ribeiro, H.I. Kenttämä, Mass Spectrometric Studies of Fast Pyrolysis of Cellulose, *European Journal of Mass Spectrometry*. 21 (2015) 321–326.
- [14] P. McKendry, Energy production from biomass (part 1): overview of biomass, *Bioresource Technology*. 83 (2002) 37–46. [https://doi.org/10.1016/S0960-8524\(01\)00118-3](https://doi.org/10.1016/S0960-8524(01)00118-3).
- [15] T. Parsell, S. Yohe, J. Degenstein, T. Jarrell, I. Klein, E. Gencer, B. Hewetson, M. Hurt, J.I. Kim, H. Choudhari, B. Saha, R. Meilan, N. Mosier, F. Ribeiro, W.N. Delgass, C. Chapple, H.I. Kenttämä, R. Agrawal, M.M. Abu-Omar, A synergistic biorefinery based on catalytic conversion of lignin prior to cellulose starting from lignocellulosic biomass, *Green Chem.* 17 (2015) 1492–1499. <https://doi.org/10.1039/C4GC01911C>.
- [16] S.L. Yohe, H.J. Choudhari, P.J. Dietrich, M.D. Detwiler, C. Akatay, D.D. Mehta, A.R. Dow, H.I. Kenttämä, W.N. Delgass, R. Agrawal, F.H. Ribeiro, High-Pressure Vapor-Phase Hydrodeoxygenation of Lignin-Derived Oxygenates to Hydrocarbons by a PtMo Bimetallic Catalyst: Product Selectivity, Reaction Pathway, and Structural Characterization, (2013).
- [17] H.J. Choudhari, V.K. Venkatakrishnan, I. Smith, I. Klein, M.M. Abu-Omar, W.N. Delgass, R. Agrawal, F.H. Ribeiro, Effect of Hydrogen Pressure during Hydrodeoxygenation of Pyrolysis Products from Biomass and Constituent Polymers, (2014).
- [18] J.D. Wagner, G.R. Lappin, J.R. Zietz, Alcohols, Higher Aliphatic, Synthetic Processes, in: *Kirk-Othmer Encyclopedia of Chemical Technology*, John Wiley & Sons, Inc., 2000. <http://onlinelibrary.wiley.com/doi/10.1002/0471238961.1925142023010714.a01/abstract> (accessed July 7, 2016).
- [19] H. Tsuji, F. Yagi, H. Hattori, H. Kita, Self-Condensation of n-Butyraldehyde over Solid Base Catalysts, *Journal of Catalysis*. 148 (1994) 759–770. <https://doi.org/10.1006/jcat.1994.1262>.

- [20] J.E. Rekoske, M.A. Barteau, Kinetics, Selectivity, and Deactivation in the Aldol Condensation of Acetaldehyde on Anatase Titanium Dioxide, *Ind. Eng. Chem. Res.* 50 (2011) 41–51. <https://doi.org/10.1021/ie100394v>.
- [21] Z.D. Young, S. Hanspal, R.J. Davis, Aldol Condensation of Acetaldehyde over Titania, Hydroxyapatite and Magnesia, *ACS Catal.* (2016). <https://doi.org/10.1021/acscatal.6b00264>.
- [22] L. Wu, T. Moteki, A.A. Gokhale, D.W. Flaherty, F.D. Toste, Production of Fuels and Chemicals from Biomass: Condensation Reactions and Beyond, *Chem.* (n.d.). <https://doi.org/10.1016/j.chempr.2016.05.002>.
- [23] T. Moteki, D.W. Flaherty, Mechanistic Insight to C–C Bond Formation and Predictive Models for Cascade Reactions among Alcohols on Ca- and Sr-Hydroxyapatites, *ACS Catal.* (2016). <https://doi.org/10.1021/acscatal.6b00556>.
- [24] J. Li, J. Tai, R.J. Davis, Hydrocarbon oxidation and aldol condensation over basic zeolite catalysts, *Catalysis Today*. 116 (2006) 226–233. <https://doi.org/10.1016/j.cattod.2006.01.032>.
- [25] S. Wang, K. Goulas, E. Iglesia, Condensation and esterification reactions of alkanals, alkanones, and alkanols on TiO₂: Elementary steps, site requirements, and synergistic effects of bifunctional strategies, *Journal of Catalysis*. 340 (2016) 302–320. <https://doi.org/10.1016/j.jcat.2016.05.026>.
- [26] J.I. Di Cosimo, V.K. Díez, C.R. Apesteguía, Base catalysis for the synthesis of α,β -unsaturated ketones from the vapor-phase aldol condensation of acetone, *Applied Catalysis A: General*. 137 (1996) 149–166. [https://doi.org/10.1016/0926-860X\(95\)00289-8](https://doi.org/10.1016/0926-860X(95)00289-8).
- [27] W.T. Reichle, Catalytic reactions by thermally activated, synthetic, anionic clay minerals, *Journal of Catalysis*. 94 (1985) 547–557. [https://doi.org/10.1016/0021-9517\(85\)90219-2](https://doi.org/10.1016/0021-9517(85)90219-2).
- [28] S. Malinowski, S. Basinski, Kinetics of aldolic reactions in the gaseous phase on solid catalysts of basic character, *Journal of Catalysis*. 2 (1963) 203–207. [https://doi.org/10.1016/0021-9517\(63\)90044-7](https://doi.org/10.1016/0021-9517(63)90044-7).
- [29] F.M. Scheidt, Vapor-phase aldol condensations over heterogeneous catalysts, *Journal of Catalysis*. 3 (1964) 372–378. [https://doi.org/10.1016/0021-9517\(64\)90042-9](https://doi.org/10.1016/0021-9517(64)90042-9).
- [30] E.L. Kunkes, E.I. Gürbüz, J.A. Dumesic, Vapour-phase C–C coupling reactions of biomass-derived oxygenates over Pd/CeZrO_x catalysts, *Journal of Catalysis*. 266 (2009) 236–249. <https://doi.org/10.1016/j.jcat.2009.06.014>.

- [31] E. Dumitriu, N. Bilba, M. Lupascu, A. Azzouz, V. Hulea, G. Cirje, D. Nibou, Vapor-Phase Condensation of Formaldehyde and Acetaldehyde into Acrolein over Zeolites, *Journal of Catalysis*. 147 (1994) 133–139. <https://doi.org/10.1006/jcat.1994.1123>.
- [32] J. Dijkmans, W. Schutyser, M. Dusselier, B.F. Sels, Sn β -zeolite catalyzed oxido-reduction cascade chemistry with biomass-derived molecules, *Chem. Commun.* 52 (2016) 6712–6715. <https://doi.org/10.1039/C6CC00199H>.
- [33] E. Dumitriu, V. Hulea, N. Bilba, G. Carja, A. Azzouz, Synthesis of acrolein by vapor phase condensation of formaldehyde and acetaldehyde over oxides loaded zeolites, *Journal of Molecular Catalysis*. 79 (1993) 175–185. [https://doi.org/10.1016/0304-5102\(93\)85100-8](https://doi.org/10.1016/0304-5102(93)85100-8).
- [34] M. Ai, Vapor-Phase Aldol Condensation of Formaldehyde with Propionic Acid on Vanadium Pentoxide—Phosphorus Pentoxide, *Applied Catalysis*. 36 (1988) 221–230. [https://doi.org/10.1016/S0166-9834\(00\)80117-7](https://doi.org/10.1016/S0166-9834(00)80117-7).
- [35] M.I. Zaki, M.A. Hasan, L. Pasupulety, Surface Reactions of Acetone on Al₂O₃, TiO₂, ZrO₂, and CeO₂: IR Spectroscopic Assessment of Impacts of the Surface Acid–Base Properties, *Langmuir*. 17 (2001) 768–774. <https://doi.org/10.1021/la000976p>.
- [36] J.I. Di Cosimo, G. Torres, C.R. Apesteguía, One-Step MIBK Synthesis: A New Process from 2-Propanol, *Journal of Catalysis*. 208 (2002) 114–123. <https://doi.org/10.1006/jcat.2002.3551>.
- [37] D.G. Hanna, S. Shylesh, Y.-P. Li, S. Krishna, M. Head-Gordon, A.T. Bell, Experimental and Theoretical Study of n-Butanal Self-Condensation over Ti Species Supported on Silica, *ACS Catal.* 4 (2014) 2908–2916. <https://doi.org/10.1021/cs500704b>.
- [38] H.E. Swift, J.E. Bozik, F.E. Massoth, Vapor-phase aldol condensation of n-butyraldehyde using a reduced tin-silica catalyst, *Journal of Catalysis*. 15 (1969) 407–416. [https://doi.org/10.1016/0021-9517\(69\)90310-8](https://doi.org/10.1016/0021-9517(69)90310-8).
- [39] W. Shen, G.A. Tompsett, R. Xing, W. Curtis Conner Jr., G.W. Huber, Vapor phase butanal self-condensation over unsupported and supported alkaline earth metal oxides, *Journal of Catalysis*. 286 (2012) 248–259. <https://doi.org/10.1016/j.jcat.2011.11.009>.
- [40] S. Luo, J.L. Falconer, Aldol condensation of acetaldehyde to form high molecular weight compounds on TiO₂, *Catalysis Letters*. 57 (n.d.) 89–93. <https://doi.org/10.1023/A:1019003817314>.

- [41] S. Luo, J.L. Falconer, Acetone and Acetaldehyde Oligomerization on TiO₂ Surfaces, *Journal of Catalysis*. 185 (1999) 393–407. <https://doi.org/10.1006/jcat.1999.2511>.
- [42] W.T. Reichle, Pulse microreactor examination of the vapor-phase aldol condensation of acetone, *Journal of Catalysis*. 63 (1980) 295–306. [https://doi.org/10.1016/0021-9517\(80\)90082-2](https://doi.org/10.1016/0021-9517(80)90082-2).
- [43] H. Idriss, K.S. Kim, M.A. Barteau, Carbon–Carbon Bond Formation via Aldolization of Acetaldehyde on Single Crystal and Polycrystalline TiO₂ Surfaces, *Journal of Catalysis*. 139 (1993) 119–133. <https://doi.org/10.1006/jcat.1993.1012>.
- [44] S. Kim, T.J. Evans, C. Mukarakate, L. Bu, G.T. Beckham, M.R. Nimlos, R.S. Paton, D.J. Robichaud, Furan production from light oxygenates in HZSM-5, *ACS Sustainable Chem. Eng.* (2016). <https://doi.org/10.1021/acssuschemeng.6b00101>.
- [45] H.B. Mayes, M.W. Nolte, G.T. Beckham, B.H. Shanks, L.J. Broadbelt, The Alpha–Beta of Glucose Pyrolysis: Computational and Experimental Investigations of 5-Hydroxymethylfurfural and Levoglucosan Formation Reveal Implications for Cellulose Pyrolysis, *ACS Sustainable Chem. Eng.* 2 (2014) 1461–1473. <https://doi.org/10.1021/sc500113m>.
- [46] S. Kudo, Z. Zhou, K. Norinaga, J. Hayashi, Efficient levoglucosenone production by catalytic pyrolysis of cellulose mixed with ionic liquid, *Green Chemistry*. 13 (2011) 3306–3311. <https://doi.org/10.1039/C1GC15975E>.
- [47] Q. Lu, X. Ye, Z. Zhang, C. Dong, Y. Zhang, Catalytic fast pyrolysis of cellulose and biomass to produce levoglucosenone using magnetic SO₄²⁻/TiO₂–Fe₃O₄, *Bioresource Technology*. 171 (2014) 10–15. <https://doi.org/10.1016/j.biortech.2014.08.075>.
- [48] Z. Wang, Q. Lu, X.-F. Zhu, Y. Zhang, Catalytic Fast Pyrolysis of Cellulose to Prepare Levoglucosenone Using Sulfated Zirconia, *ChemSusChem*. 4 (2011) 79–84. <https://doi.org/10.1002/cssc.201000210>.
- [49] S.H. Krishna, T.W. Walker, J.A. Dumesic, G.W. Huber, Kinetics of Levoglucosenone Isomerization, *ChemSusChem*. 10 (2017) 129–138. <https://doi.org/10.1002/cssc.201601308>.
- [50] X. Hu, R.J. M. Westerhof, L. Wu, D. Dong, C.-Z. Li, Upgrading biomass-derived furans via acid-catalysis/hydrogenation: the remarkable difference between water and methanol as the solvent, *Green Chemistry*. 17 (2015) 219–224. <https://doi.org/10.1039/C4GC01826E>.

- [51] M.W. Easton, J.J. Nash, H.I. Kenttämä, Dehydration Pathways for Glucose and Cellobiose During Fast Pyrolysis, *J. Phys. Chem. A*. 122 (2018) 8071–8085. <https://doi.org/10.1021/acs.jpca.8b02312>.
- [52] P.R. Patwardhan, J.A. Satrio, R.C. Brown, B.H. Shanks, Influence of inorganic salts on the primary pyrolysis products of cellulose, *Bioresource Technology*. 101 (2010) 4646–4655. <https://doi.org/10.1016/j.biortech.2010.01.112>.
- [53] V.K. Venkatakrishnan, J.C. Degenstein, A.D. Smeltz, W.N. Delgass, R. Agrawal, F.H. Ribeiro, High-pressure fast-pyrolysis, fast-hydropyrolysis and catalytic hydrodeoxygenation of cellulose: production of liquid fuel from biomass, *Green Chem.* 16 (2014) 792–802. <https://doi.org/10.1039/C3GC41558A>.
- [54] Y. Lu, N.S. Mosier, Kinetic modeling analysis of maleic acid-catalyzed hemicellulose hydrolysis in corn stover, *Biotechnology and Bioengineering*. 101 (2008) 1170–1181. <https://doi.org/10.1002/bit.22008>.
- [55] T.H. Parsell, B.C. Owen, I. Klein, T.M. Jarrell, C.L. Marcum, L.J. Hauptert, L.M. Amundson, H.I. Kenttämä, F. Ribeiro, J.T. Miller, M.M. Abu-Omar, Cleavage and hydrodeoxygenation (HDO) of C–O bonds relevant to lignin conversion using Pd/Zn synergistic catalysis, *Chem. Sci.* 4 (2013) 806–813. <https://doi.org/10.1039/C2SC21657D>.
- [56] I. Klein, B. Saha, M.M. Abu-Omar, Lignin depolymerization over Ni/C catalyst in methanol, a continuation: effect of substrate and catalyst loading, *Catal. Sci. Technol.* 5 (2015) 3242–3245. <https://doi.org/10.1039/C5CY00490J>.
- [57] F. Ronsse, X. Bai, W. Prins, R.C. Brown, Secondary reactions of levoglucosan and char in the fast pyrolysis of cellulose, *Environmental Progress & Sustainable Energy*. 31 (2012) 256–260. <https://doi.org/10.1002/ep.11633>.
- [58] T. Ridha, Y. Li, E. Genç, J.J. Siirola, J.T. Miller, F.H. Ribeiro, R. Agrawal, Valorization of Shale Gas Condensate to Liquid Hydrocarbons through Catalytic Dehydrogenation and Oligomerization, *Processes*. 6 (2018) 139. <https://doi.org/10.3390/pr6090139>.
- [59] R. Joshi, G. Zhang, J.T. Miller, R. Gounder, Evidence for the Coordination–Insertion Mechanism of Ethene Dimerization at Nickel Cations Exchanged onto Beta Molecular Sieves, *ACS Catal.* 8 (2018) 11407–11422. <https://doi.org/10.1021/acscatal.8b03202>.

- [60] R.D. Andrei, M.I. Popa, F. Fajula, V. Hulea, Heterogeneous oligomerization of ethylene over highly active and stable Ni-*AlSBA-15* mesoporous catalysts, *Journal of Catalysis*. 323 (2015) 76–84. <https://doi.org/10.1016/j.jcat.2014.12.027>.
- [61] V. Hulea, F. Fajula, Ni-exchanged *AlMCM-41*—An efficient bifunctional catalyst for ethylene oligomerization, *Journal of Catalysis*. 225 (2004) 213–222. <https://doi.org/10.1016/j.jcat.2004.04.018>.
- [62] M. Meloni, R.C. Runnebaum, Tuning supported Ni catalysts by varying zeolite Beta heteroatom composition: effects on ethylene adsorption and dimerization catalysis, *Catal. Sci. Technol.* 11 (2021) 3393–3401. <https://doi.org/10.1039/D1CY00308A>.
- [63] J. Thakkar, X. Yin, X. Zhang, Ethylene Oligomerization to Select Oligomers on Ni-*ETS-10*, *ChemCatChem*. 10 (2018) 4234–4237. <https://doi.org/10.1002/cctc.201800650>.
- [64] H. Olivier-Bourbigou, P.A.R. Breuil, L. Magna, T. Michel, M.F. Espada Pastor, D. Delcroix, Nickel Catalyzed Olefin Oligomerization and Dimerization, *Chem. Rev.* 120 (2020) 7919–7983. <https://doi.org/10.1021/acs.chemrev.0c00076>.
- [65] A. Finiels, F. Fajula, V. Hulea, Nickel-based solid catalysts for ethylene oligomerization – a review, *Catal. Sci. Technol.* 4 (2014) 2412–2426. <https://doi.org/10.1039/C4CY00305E>.
- [66] A.N. Mlinar, G.B. Baur, G.G. Bong, A. “Bean” Getsoian, A.T. Bell, Propene oligomerization over Ni-exchanged Na-X zeolites, *Journal of Catalysis*. 296 (2012) 156–164. <https://doi.org/10.1016/j.jcat.2012.09.010>.
- [67] A. Saxena, R. Joshi, R.R. Seemakurthi, E. Koninckx, L.J. Broadbelt, J. Greeley, R. Gounder, Effect of Nickel Active Site Density on the Deactivation of Ni-Beta Zeolite Catalysts during Ethene Dimerization, *ACS Eng. Au.* (2021). <https://doi.org/10.1021/acsengineeringau.1c00014>.
- [68] J.P.G. Pater, P.A. Jacobs, J.A. Martens, 1-Hexene Oligomerization in Liquid, Vapor, and Supercritical Phases over Beidellite and Ultrastable Y Zeolite Catalysts, *Journal of Catalysis*. 179 (1998) 477–482. <https://doi.org/10.1006/jcat.1998.2250>.
- [69] Y.T. Kim, J.P. Chada, Z. Xu, Y.J. Pagan-Torres, D.C. Rosenfeld, W.L. Winniford, E. Schmidt, G.W. Huber, Low-temperature oligomerization of 1-butene with H-ferrierite, *Journal of Catalysis*. 323 (2015) 33–44. <https://doi.org/10.1016/j.jcat.2014.12.025>.

- [70] O. Jan, K. Song, A. Dichiara, F.L.P. Resende, Oligomerization of supercritical ethylene over nickel-based silica-alumina catalysts, *Chemical Engineering Science*. 197 (2019) 212–222. <https://doi.org/10.1016/j.ces.2018.12.018>.
- [71] J. Wang, F. Hassan, P.I. Chigada, S.P. Rigby, B. Al-Duri, J. Wood, Coke Formation and Characterization During 1-Hexene Isomerization and Oligomerization over H-ZSM-5 Catalyst under Supercritical Conditions, *Ind. Eng. Chem. Res.* 48 (2009) 7899–7909. <https://doi.org/10.1021/ie801466d>.
- [72] G.V.S. Seufitelli, F.L.P. Resende, Study of the catalytic reactions of ethylene oligomerization in subcritical and supercritical media over a NiBEA catalyst, *Applied Catalysis A: General*. 576 (2019) 96–107. <https://doi.org/10.1016/j.apcata.2019.01.015>.
- [73] L.M. Petkovic, D.M. Ginosar, K.C. Burch, Supercritical fluid removal of hydrocarbons adsorbed on wide-pore zeolite catalysts, *Journal of Catalysis*. 234 (2005) 328–339. <https://doi.org/10.1016/j.jcat.2005.06.027>.
- [74] G. Manos, H. Hofmann, Coke removal from a zeolite catalyst by supercritical fluids, *Chemical Engineering & Technology*. 14 (1991) 73–78. <https://doi.org/10.1002/ceat.270140111>.
- [75] B. Subramaniam, Enhancing the stability of porous catalysts with supercritical reaction media, *Applied Catalysis A: General*. 212 (2001) 199–213. [https://doi.org/10.1016/S0926-860X\(00\)00848-6](https://doi.org/10.1016/S0926-860X(00)00848-6).
- [76] B. Subramaniam, S. Saim, In situ mitigation of coke buildup in porous catalysts with supercritical reaction media, US5725756A, 1998. <https://patents.google.com/patent/US5725756A/en> (accessed May 14, 2019).
- [77] H. Tiltscher, H. Wolf, J. Schelchshorn, A Mild and Effective Method for the Reactivation or Maintenance of the Activity of Heterogeneous Catalysts, *Angewandte Chemie International Edition in English*. 20 (1981) 892–894. <https://doi.org/10.1002/anie.198108921>.
- [78] I. Agirrezabal-Telleria, E. Iglesia, Stabilization of active, selective, and regenerable Ni-based dimerization catalysts by condensation of ethene within ordered mesopores, *Journal of Catalysis*. 352 (2017) 505–514. <https://doi.org/10.1016/j.jcat.2017.06.025>.
- [79] I. Agirrezabal-Telleria, E. Iglesia, Mechanistic insights and consequences of intrapore liquids in ethene, propene, and butene dimerization on isolated Ni²⁺ sites grafted within

- aluminosilicate mesopores, *Journal of Catalysis*. 389 (2020) 690–705.
<https://doi.org/10.1016/j.jcat.2020.06.038>.
- [80] J. Butt, *Activation, Deactivation, and Poisoning of Catalysts*, Elsevier, San Diego, 2012.
- [81] M. Lallemand, A. Finiels, F. Fajula, V. Hulea, Catalytic oligomerization of ethylene over Ni-containing dealuminated Y zeolites, *Applied Catalysis A: General*. 301 (2006) 196–201.
<https://doi.org/10.1016/j.apcata.2005.12.019>.
- [82] R.Y. Brogaard, M. K murcu, M.M. Dyballa, A. Botan, V. Van Speybroeck, U. Olsbye, K. De Wispelaere, Ethene Dimerization on Zeolite-Hosted Ni Ions: Reversible Mobilization of the Active Site, *ACS Catal.* 9 (2019) 5645–5650.
<https://doi.org/10.1021/acscatal.9b00721>.
- [83] J.M. Haynes, Pore size analysis according to the Kelvin equation, *Mat. Constr.* 6 (1973) 209–213. <https://doi.org/10.1007/BF02479035>.
- [84] J.T. Scanlon, D.E. Willis, Calculation of Flame Ionization Detector Relative Response Factors Using the Effective Carbon Number Concept, *J Chromatogr Sci.* 23 (1985) 333–340.
<https://doi.org/10.1093/chromsci/23.8.333>.
- [85] J. Sluiter, A. Sluiter, *Summative Mass Closure: Laboratory Analytical Procedure (LAP) Review and Integration*, 2011.

PUBLICATIONS

1. **R. Caulkins**, R. Joshi, R. Gounder, F.H. Ribeiro, Effects of Ethene Pressure on the Deactivation of Ni-Zeolites During Ethene Oligomerization at Sub-ambient Temperatures, *ChemCatChem*. (2021)
2. Talpade, A., **Caulkins, R.**, Xu, L., Ridha, T., Kenttämä, H., Agrawal, R., Delgass, W.N., Ribeiro, F.H., “Origins of char formation during fast-hydropyrolysis of biomass to fuels and chemicals,” in preparation.
3. Ridha, T., **Caulkins, R.**, Talpade, A., Li, Y., Gencer, E., Ribeiro, F.H., Delgass, W.N., Tawarmalani, M., Agrawal, R., “Upgrading Fast-Hydropyrolysis Vapor of Cellulose to Higher Molecular Weight Products Using Systems-level Molecular Mapping,” in preparation.
4. Talpade, A., Xu, L., **Caulkins, R.**, Easton, M., Kenttämä, H., Agrawal, R., Delgass, W.N., Ribeiro, F.H., “Mechanistic effects of inorganic compounds on the fast pyrolysis of cellulosic materials,” in preparation.
5. LiBretto, N.J., Xu, Y., Quigley, A., Edwards, E., Nargund, R., Vega-Vila, J.C., **Caulkins, R.**, Saxena, A., Gounder, R., Greeley, J., Zhang, G., Miller, J.T., “Olefin oligomerization by main group Ga^{3+} and Zn^{2+} single site catalysts on SiO_2 ,” *Nature Communications* **12** (2021)